HAL
open science

Statistical modeling of bladder motion and deformation in prostate cancer radiotherapy

Richard Rios Patiño

To cite this version:

Richard Rios Patiño. Statistical modeling of bladder motion and deformation in prostate cancer radiotherapy. Signal and Image Processing. Université de Rennes; Universidad nacional de Colombia, 2017. English. NNT : 2017REN1S116 . tel-01779880

HAL Id: tel-01779880

https://theses.hal.science/tel-01779880v1

Submitted on 27 Apr 2018

HAL is a multi-disciplinary open access archive for the deposit and dissemination of scientific research documents, whether they are published or not. The documents may come from teaching and research institutions in France or abroad, or from public or private research centers.

L'archive ouverte pluridisciplinaire **HAL**, est destinée au dépôt et à la diffusion de documents scientifiques de niveau recherche, publiés ou non, émanant des établissements d'enseignement et de recherche français ou étrangers, des laboratoires publics ou privés.

ANNÉE 2017

THÈSE / UNIVERSITÉ DE RENNES 1
sous le sceau de l'Université Bretagne Loire

En Cotutelle Internationale avec
UNIVERSIDAD NACIONAL DE COLOMBIA, Colombia

pour le grade de

DOCTEUR DE L'UNIVERSITÉ DE RENNES 1

Mention : Traitement du Signal et Télécommunications

Ecole doctorale MATISSE

présentée par

Richard RIOS PATIÑO

préparée à l'unité de recherche LTSI-INSERM U1099
Laboratoire Traitement du Signal et de l'Image
ISTIC UFR Informatique et Électronique
Grupo de Automatica de la UNAL-Facultad de Minas

Statistical modeling of bladder motion and deformation in prostate cancer radiotherapy

Thèse soutenue à Medellín le 2 mai 2017

devant le jury composé de :

Jose Carlos PRINCIPE
Professeur, University of Florida / rapporteur

Jason DOWLING
Senior Research Scientist, CSIRO / rapporteur

Edgar Eduardo ROMERO CASTRO
Professeur, Universidad Nacional de Colombia / examinateur

Oscar ACOSTA TAMAYO
MCU, Université de Rennes 1/ examinateur

Diana MATEUS
Senior Research Scientist, Technical University of Munich / examinateur

Jairo J. ESPINOSA OVIEDO
Professeur, Universidad Nacional de Colombia/ directeur de thèse

Renaud DE CREVOISIER
PU/PH, Université de Rennes 1/ directeur de thèse

A mi madre, cuyo apoyo y compromiso, me han permitido alcanzar las metas propuestas

Acknowledgements

This thesis was made possible by a co-supervision agreement between the Universidad Nacional de Colombia Sede Medellín and the Université de Rennes 1. I would like to acknowledge that this research was supported by the Departamento Administrativo de Ciencia, Tecnología e Innovación (COLCIENCIAS) - Colombia with the "Becas de Doctorado en Colombia 2010 - Convocatoria 511" grant, and also by the Institut National du Cancer (INCa) - France with the "STIC IGRT-P" project. Without all these generous efforts it would not have been possible to develop this work.

I would like to thank to my supervisors, Prof. Jairo José Espinosa Oviedo, Prof. Renaud de Crevoisier and Prof. Oscar Acosta for guiding me throughout the thesis process and for providing the necessary theoretical support to complete this thesis. What I have learned from them goes beyond the limits of academia. Besides, I would like to thanks to Profs. Carlos E. Mejía and Norman Diego Giraldo from the Universidad Nacional de Colombia (UNAL), I express my utmost gratitude for thier comments and advices to achieve this thesis.

I feel honored for having conducted my research work at the Gaunal research group from the UNAL and the Laboratoire Traitement du Signal et de l'Image (LTSI) from the Université de Rennes 1 (UR1). I met very gentle people in both places. In particular Muriel Diop, Soizic Charpentier and Patricia Gerouard made my days at the LTSI very pleasant and happy ones; similarly, I would like to thank to Marina Grisales and Magda Pinto at the UNAL. I will always remember their kindness and welcome.

I am also in debt to my colleagues: Julian Patiño that always encouraged me to enjoy this work even in the not so good times; to Guillaume Cazoulat that was always ready wheter to discuss ideas from my thesis or take a beer after work; to Juan David Ospina that opened the door to arrive to the LTSI; and also to Frederic Commandeur, Mohamed Nassef, Gael Drean, Aureline Fargeas, Bastien Rigaud, Ricardo Gutierrez and Khemara Gnep that helped me day to day wheater with comments and observations of my work, or even free time to take coffee. From the LTSI and GAUNAL, I also have special gratitude to Geoffray Roman-Jimenez, Sophie Collin, Juan Mantilla, Hélène Feuillatre, Nasraw, Nadine, Matthieu Dyn, Xavier (el Catalan), Ibra, Roviro, Andres, Marquez, Harold, Mario Giraldo, Cesar Gomez, Edwin Lopera, Julian Betancur, Zulma, Tovard, Ahmad, and Mahmoud. Also, I have an special gratitude to some special friends and persons: Sebastian Castrillon, Isabel Arcila, Jenifer Posada, Omar, Luis F, DOC, Ju Lie, Efren, Lucho, Cecilia Isacchi, Alba Vargas, Anssony Balaguera, Sandra Balaguera, Zehir and Marian Lee (who also helped me to proofread this document). They have contributed to make this period of my life a very happy one.

Finally, I want to dedicate this work to my whole family RIOS PATIÑO and also to my second family FRANCO-ARANGO.

Summary

Prostate cancer is the most common cancer amongst the male population in most developed countries. It is the most common cancer amongst the male population in France (73.609 cases in 2014) and in Colombia (9564 cases in 2014). It is also the third most common cause of cancer deaths in males in both countries (9.3% and 7.1% in France and in Colombia in 2014, respectively). One of the standard treatment methods is external radiotherapy, which involves delivering ionizing radiation to a clinical target, namely the prostate and seminal vesicles. Due to the uncertain location of organs during treatment, which involves around forty (40) radiation fractions delivering a total dose ranging from 70 to 80Gy, safety margins are defined around the tumor target upon treatment planning. The radiation units are expressed in Grays, abbreviated as Gy, which represents 1 Jule/Kg. This leads to portions of healthy organs neighboring the prostate or organs at risk — the bladder and rectum — to be included in the target volume, potentially resulting in adverse events affecting patients' urinary (hematuria and cystitis, among others) or rectal (rectal bleeding, fecal incontinence, etc.) functions. Several studies have shown that increasing dose delivery to the prostate leads to improved local cancer control, up to approximately 80Gy. However, such dose increases are limited by their associated risks of treatment-related toxicity involving the organs at risk.

The bladder is notorious for presenting the largest inter-fraction shape variations during treatment, caused by continuous changes in volume. These variations in shape introduce geometric uncertainties that render assessment of the actual dose delivered to the bladder during treatment difficult, thereby leading to dose uncertainties that limit the possibility of modeling dose-volume response for late genitourinary (GU) toxicity. The Quantitative Analysis of Normal Tissue Effects in the Clinic (QUANTEC) project has stated that a similar dose-response to that of late gastrointestinal (GI) toxicity is far from being established. The dosimetric variables obtained from the planning CT prove to be very poor surrogates for the real delivered dose. As a result, it appears crucial to quantify uncertainties produced by inter-fraction bladder variations in order to determine dosimetric factors that affect late GU complications.

The aim of this thesis was thus to characterize and predict uncertainties produced by geometric variations of the bladder between fractions, using solely the planning CT as input information. In clinical practice, a single CT scan is only available for a typical patient during the treatment planning while on-treatment CTs/CBCTs are seldom available. In this thesis, we thereby used a population approach to obtain enough data to learn the most important directions of bladder motion and deformation using

principal components analysis (PCA). As in groundwork, these directions were then used to develop population-based models in order to predict and quantify geometrical uncertainties of the bladder. However, we use a longitudinal analysis in order to properly characterize both patient-specific variance and modes from the population. We proposed to use mixed-effects (ME) models and hierarchical PCA to separate intra and inter-patient variability to control confounding cohort effects. Other than using PCA, bladder shapes were represented by using spherical harmonics (SPHARM) which additionally enables data compression without losing information. Subsequently, we presented PCA models as a tool to quantify dose uncertainties produced by bladder motion and deformation between fractions. We then estimated mean and variance of the dose delivered to the bladder using PCA-based models via Monte Carlo simulation and dose integration; and subsequently, we compared the estimated accumulated doses with the accumulated dose derived from non-rigid registration and patient's available images. We also calculated average voxel doses, local dose variability and dose-volume histogram uncertainties.

Résumé

Le cancer de la prostate est le cancer le plus fréquent chez les hommes dans la plupart des pays développés. C'est le cancer le plus fréquent chez les hommes en France (73.609 cas en 2014) et en Colombie (9564 cas en 2014). En outre, c'est la troisième cause de décès par cancer chez les hommes dans les deux pays (9,3 % en France et 7,1 % en Colombie en 2014). Il existe de nombreuses techniques différentes pour soignier le cancer de la prostate, comme la chirurgie, la chimiothérapie, la radiothérapie externe et la curiethérapie, entre autres. La radiothérapie externe (EBRT) est une technique principalement utilisée pour le cancer localisé qui consiste à délivrer un rayonnement ionisant pour détruire les cellules tumorales. Cependant, les tissus sains qui entourent recevront également une dose de rayonnement, ce qui peut altérer le fonctionnement normal. L'EBRT est donc un compromis entre permettre une dose élevée à la tumeur et épargner des organes sains qui sont voisins. Ces tissus sains entourant la tumeur sont appelés les organes à risque (OARs). Le terme radiothérapie désignera dorénavant l'EBRT.

Dans la radiothérapie du cancer de la prostate, la prostate et les vésicules séminales définissent la cible principale à irradier tandis que les OARs sont la vessie et le rectum. Quand un patient, qui a la maladie du cancer de la prostate, est soigné avec radiothérapie, une tomodensitométrie (TDM) est prise de la zone pelvienne et les organes du patient sont délimités (à savoir la prostate, les vésicules séminales, la vessie et le rectum). Depuis le plan de délivrance de la dose est optimisé afin de respecter les contraintes de dose maximale sur les organes à risque et de dose prescrite sur la prostate. Ensuite, le traitement est délivré au patient sur plusieurs fractions sur plusieurs jours, où une petite quantité de la dose est donnée pour chaque fraction. Par exemple, si une dose de 80 Gy est prescrite à la prostate, des fractions de 2 Gy administrées pendant 5 jours en huit semaines sont le planning du traitement classique. Le fractionnement de dose est effectué pour augmenter le rapport thérapeutique, c'est-à-dire qu'il permet aux tissus sains de se réparer entre les fractions et d'augmenter les dommages aux cellules de la tumeur par réoxygénation et redistribution.

Cependant, les organes pelviens se déplacent et se déforment entre les fractions en introduisant des incertitudes géométriques aléatoires qui rendent difficile la correcte livraison de la dose à la tumeur et les OARs. Ces changements de taille et de forme dans les organes conduisent à des géométries qui ne sont pas exactement à celles délimités lors de la planification. Par exemple, ces variations peuvent inclure des contractions/dilatations du rectum, remplissage et vidange quotidiens de la vessie, des

contractions musculaires involontaires, etc. Ces variations d'organe peuvent donc exposer le patient à une sous-dose de rayonnement dans la zone de la tumeur ou à une surdose concernant OAR. Ainsi, des marges de sécurité sont introduites autour de la tumeur sur le plan de délivrance afin d'élargir la zone irradiée. Néanmoins, cela implique également que des portions des OARs seront fortement irradiées, ce qui peut entraîner des événements indésirables qui affectent les fonctions organiques du patient (hématurie, cystite, hémorragie rectale, incontinence fécale, entre autres). Bien que les nouvelles technologies - comme la radiothérapie guidée par image (IGRT), les marqueurs et la radiothérapie à intensité modulée (IMRT)- nous permettent de distribuer des doses complexes et de réduire les incertitudes sur la position et la forme réelles des organes, l'intégration en ligne de tous ces technologies lors de la thérapie n'est pas encore pratique ou trop coûteuse (par exemple, l'imagerie en ligne de la zone pelvienne et le calcul de la dose pendant une fraction quotidienne en temps réel). En conséquence, les incertitudes géométriques aléatoires ont encore un impact au cours du traitement, en réduisant sa qualité.

La vessie présente les plus grandes variations de forme entre fractions de traitement, provoquées par des changements continus de volume. Ces variations de forme introduisent des incertitudes géométriques qui rendent difficile l'évaluation de la dose qui est réellement délivrée à la vessie pendant le traitement. Ces incertitudes limitent la possibilité de modéliser une relation dose-volume pour la toxicité génito-urinaire tardive (GU). Le projet QUANTEC (Quantitative Analysis of Normal Tissue Effects in the Clinic) a déclaré qu'une dose-réponse similaire à celle de la toxicité gastro-intestinale tardive (GI) était loin d'être établie. Les variables dosimétriques obtenues à partir de la tomodensitométrie de planification peuvent être faiblement représentative de la dose effectivement délivré. En conséquence, il est crucial de quantifier les incertitudes produites par les variations inter-fraction de la vessie afin de déterminer les facteurs dosimétriques qui affectent les complications GU tardives.

Le but de cette thèse était donc de caractériser et de prédire les incertitudes produites par les variations géométriques de la vessie entre les fractions de traitement, en utilisant uniquement la tomodensitométrie de planification comme information d'entrée. En pratique clinique, une seule tomodensitométrie est disponible lors de la planification du traitement d'un patient typique, alors que des images supplémentaires peuvent être acquises en cours de traitement. Dans cette thèse, une approche basée population a été utilisée pour obtenir suffisamment de données pour apprendre les directions les plus importantes du mouvement et de la déformation de la vessie en utilisant l'analyse en composante principales (PCA). Comme dans les travaux de référence, ces directions ont ensuite été utilisées pour développer des modèles basés population pour prédire et quantifier les incertitudes géométriques de la vessie. Cependant, nous avons utilisé une analyse longitudinale afin de caractériser correctement la variance du patient et ses modes spécifiques à partir de la population. Nous avons proposé d'utiliser un modèle à effets mixtes (ME) et une PCA hiérarchique pour séparer la variabilité intra et inter-patients afin de contrôler les effets de cohorte confondus. Outre l'PCA, la forme de la vessie a été représentée par l'utilisation d'harmoniques sphériques (SPHARM), ce qui a permis la compression des données sans perte d'information. Finalement, nous avons

présenté des modèles sur l'PCA comme un outil pour quantifier des incertitudes de la dose produit par le mouvement et déformation de la vessie entre fractions. Également, en utilisant seulement l'information de planification, les objectifs spécifiques de la thèse sont: i) de caractériser et prédire le mouvement et la déformation de la vessie entre les fractions ; ii) de quantifier les incertitudes de dose et de DVH produites par les variations géométriques de la vessie entre les fractions ; iii) proposer une méthodologie pour modéliser le mouvement et la déformation OAR entre les fractions qui aide à déterminer la dose de planification optimale et les modifications du traitement en intégrant contraintes du traitement (taille de fraction et événements de toxicité), le mouvement OAR et les contraintes de déformation et de traitement.

La première étape de cette thèse consistait en apprendre les directions les plus importantes (modes dominants) du mouvement et de la déformation de la vessie à partir d'une base de données de population à l'aide de l'analyse des composantes principales (PCA). Nous avons utilisé ces modes dominants pour caractériser les formes de la vessie et les régions de déformation/mouvement. Cette thèse a aussi proposé une méthode de normalisation pour aligner anatomiquement les structures pelviennes (prostate et vessie) pour tous les patients dans le même référentiel spatial. Cette méthode était un enregistrement rigide qui permettait de quantifier le mouvement et les déformations de la vessie par rapport au barycentre de la prostate d'un patient modèle. La deuxième étape était une première étape de réduction de la dimensionnalité en utilisant des harmoniques sphériques (SPHARM). Cette étape nous a permis de réduire le nombre de paramètres requis pour représenter la surface de la vessie, de plus encodés avec les modes dominants dérivés par PCA. La troisième étape consistait à introduire une analyse longitudinale pour développer des modèles basés sur la population, au lieu d'utiliser l'analyse transversale comme dans les travaux précédents. Avec cela, .

Deuxièmement, nous avons caractérisé la variance du patient de la population sur chaque mode. En plus, nous avons proposé d'utiliser un modèle à effets mixtes (ME) et une PCA hiérarchique pour séparer la variabilité intra et inter-patients afin de contrôler les effets de cohorte confondu. La troisième étape était de quantifier les incertitudes de la dose et DVHs qui sont produites par le mouvement de la vessie et la déformation entre les fractions. Nous avons formé des modèles individuels de PCA à partir des échantillons de vessie disponibles sur les images CT/CBCT en cours de traitement de trois patients. Sur la base des modèles ci-dessus, des sommes pondérées de ces modes ont été utilisées pour estimer les vessies avec leur probabilité d'occurrence. Nous avons ensuite estimé la moyenne et la variance de la dose délivrée à la vessie en utilisant des modèles basés sur la PCA par la méthode de simulation de Monte-Carlo et l'intégrale de la dose; et par la suite, nous avons comparé les doses cumulées estimées avec la dose accumulée obtenue en utilisant un recalage d'image non-rigide et les images du patient. Également, nous avons calculé la moyenne de la dose par voxel, la variabilité de la dose locale et des incertitudes d'histogramme de volume de dose.

Finalement, les contributions de cette thèse ont été sur trois sujets de recherche principaux : i) la caractérisation des formes et des régions de mouvement/déformation de la vessie pour une base de données de patients utilisant PCA; ii) l'approche longitudinale utilisé pour prédire le mouvement et la déformation de la vessie spécifiques du patient en

apprenant à partir d'une base de données d'entraînement longitudinale; iii) l'utilisation des modèles PCA comme outil virtuel pour évaluer les incertitudes dosimétriques produites par le mouvement de la vessie et la déformation entre les fractions. Concernant au premier sujet, la méthode de normalisation utilisée pour aligner anatomiquement les structures pelviennes nous a permis de quantifier le mouvement et les déformations de la vessie par rapport à un point référentiel spatial. Egalement, la réduction de la dimensionnalité en utilisant SPHARM nous a permis de réduire le temps de calcul, les erreurs numériques produit par des opérations arithmétiques finies et le stockage de données. Concernant au deuxième sujet, l'approche longitudinale nous a permis de caractériser des formes et des régions de mouvement/déformation de la vessie; et par la suite, de visualiser et d'identifier la variabilité hétérogène observée dans base de données de la vessie. Concernant au troisième sujet, cette thèse a déterminé le nombre de modes nécessaires pour déterminer les régions de mouvement/déformation, ainsi que pour estimer la dose cumulée de la vessie. Nous avons montré que seul le premier mode avait un impact significatif sur l'estimation de dose cumulée car il décrit les changements les plus significatifs en volume en dehors des faisceaux.

Resumen

El cáncer de próstata es el cáncer más común entre la población masculina en muchos de los países desarrollados. Especificamente, es el cáncer más común de la población masculina tanto en Francia (73.609 casos en 2014) como en Colombia (9564 casos en 2014); y además, es también la tercera causa de muerte por cancer en los hombres para ambos países (9.3% y 7.1% en Francia y en Colombia en 2014, respectivamente). Uno de los métodos de tratamiento más común es la radioterapia externa, el cual consiste en enviar una radiación ionizante a un objetivo clínico, en este caso la próstata y las vesículas seminales. Debido a incertidumbres producidas por variaciones anatómicas de los órganos durante el tratamiento, el cual consiste en 40 fracciones para un total de dosis entre 70 y 80 Gy, márgenes de seguridad son definidos alrededor del tumor durante la planeación del tratamiento. Lo anterior, conlleva a que partes de los órganos sanos, también llamados órganos en riesgo, que son cercanos a la próstata y vesículas seminales -como la vejiga y el recto- también sean irradiados, potencialmente resultando en eventos adversos que afectan las funciones urinarias (hematuria e infección urinaria) o rectal (sangrado rectal, incontinencia fecal) del paciente. Algunos estudios han demostrado que el incrementando la dosis a la próstata permite un mejor control local del cáncer (por encima de los 80Gy aproximadamente). Sin embargo, tales incrementos de dosis son limitados por sus riesgos asociados de toxicidad para los órganos en riesgo.

La vejiga es particular por presentar las variaciones de forma más grandes entre las fracciones del tratamiento, las cuales son causadas por continuos cambios de volumen. Estas variaciones de forma de la vejiga introducen incertidumbres geométricas que hacen difícil la determinacion de la verdadera dosis entregada a la vejiga durante el tratamiento. Estas incertidumbres limitan la posibilidad de modelar una relación dosis-volumen para la toxicidad Genitourinario tardia (GU). El proyecto Quantitative Analysis of Normal Tissue Effects in the Clinic (QUANTEC) ha establecido que una respuesta dosis-volumen similar a la que se tiene para la toxicidad Gastrointestinal tardia (GI) está lejos de ser establecida. Las variables dosimétricas que se obtienen de la tomografía computarizada de planeación pueden ser débilmente represenativas de la verdadera dosis suministrada. Por lo tanto, es crucial identificar las incertidumbres producidas por el movimiento y deformación entre fracciones de la vejiga con el fin de determinar los factores dosimétricos que afectan las complicaciones GU tardías.

El propósito de esta tesis fue entonces caracterizar y predecir las incertidumbres geométricas producidas por las variaciones geométricas de la vejiga entre fracciones, usando solamente el CT de planeación como información de entrada. En la práctica

clínica, un sola tomografía computarizada esta disponible en la fase de planeación del tratamiento para un paciente típico, mientras que imágenes suplementarias durante el tratamiento estan raramente disponibles. Por lo tanto, en esta tesis fue usado un enfoque poblacional para obtener suficientes datos para aprender las direcciones más importantes de movimiento y deformación de la vejiga usando análisis de componentes principales (ACP). Tal como en trabajos anteriores, estas direcciones fueron también usadas para desarrollar modelos poblacionales para predecir y cuantificar incertidumbres geométricas de la vejiga. Sin embargo, en esta tesis se propuso un análisis longitudinal con el fin de adecuadamente caracterizar la varianza y los modos del paciente de la población. Básicamente, se propuso usar modelos de efectos-mixtos (ME) y ACP jerárquico para separar la variabilidad intra e inter-paciente para controlar efectos confusos de la población. Adicional a ACP, la superficie de la vejiga también fue representada usando esféricos harmónicos (SPHARM), lo cual nos permitio adicionalmente comprimir los datos sin perder información. Finalmente, se presentan los modelos basado en ACP como una herramienta para cuantificar las incertidumbres de la dosis producidas por el movimiento y deformación de la vejiga entre fracciones. El promedio y la varianza de la dosis entregada a la vejiga fueron estimadas utilizando modelos ACP via simulación de Monte Carlo e integración de la dosis; y posteriormente, se comparo las dosis acumuladas estimadas con la dosis acumulada obtenida a partir de registro no-rigido y las imagenes disponibles del paciente. Igualmente, se calcularon los valores promedio de la dosis por voxel, la variabilidad local de la dosis y las incertidumbres de los histogramas dosis-volumen.

Contents

Summary/ Résumé/ Resumen 1

Contents 11

List of figures 15

List of tables 18

Acronyms 19

I Problem definition, objectives and clinical context 21

1 Introduction: clinical context and treatment uncertainties in prostate cancer radiotherapy 23
1.1 Prostate cancer . . . 23
1.1.1 Diagnosis and staging of prostate cancer . . . 24
1.1.2 Curative treatments for localized prostate cancer . . . 27
1.2 External beam radiotherapy in prostate cancer . . . 27
1.2.1 Irradiation techniques . . . 29
1.2.2 Image guided radiotherapy . . . 30
1.3 Current practices and treatment plan evaluation in prostate cancer radiotherapy . . . 31
1.4 Random geometric uncertainties in prostate cancer radiotherapy . . . 33
1.5 Research problem . . . 39
1.6 Objectives . . . 40
1.7 Chapter by chapter overview . . . 42

II Population-based PCA models using a longitudinal approach to describe bladder geometrical uncertainties 45

2 Data, spatial normalization and organ parametrization 47
2.1 Data . . . 47
2.1.1 Training database . . . 47

2.1.2 Validation database 48
2.1.3 Descriptive information 49
2.2 Prostate-based rigid registration 50
2.3 Bladder shape parametrization 51
2.4 Discussion 52
2.5 Conclusion 55

3 Characterization and dimensionality reduction of bladder motion and deformation in prostate cancer radiotherapy 57
3.1 Data 57
3.2 Methods 58
3.2.1 Principal component analysis 59
3.2.2 Validation 59
3.3 Results 60
3.4 Discussion 63
3.5 Conclusion 64

4 Population PCA-based models using a longitudinal approach: characterization of patient-specific variance from the population variance 65
4.1 Data 66
4.2 Methods 66
4.2.1 Principal component analysis 66
4.2.2 Linear mixed-effects model 68
4.2.3 Out-of-sample problem 69
4.2.4 Evaluation of prediction performance 70
4.2.5 Metrics of similarity between PMs 72
4.2.5.1 Mutual information-based metric 72
4.2.5.2 Metric of misestimated voxel 74
4.3 Results 75
4.3.1 PCA representation 75
4.3.2 Evaluation of performance prediction with groundwork models . 78
4.4 Discussion 82
4.5 Conclusion 86

5 Population PCA-based models using a longitudinal approach: characterization of patient-specific modes from the population modes 87
5.1 Data 88
5.2 Methods 88
5.2.1 Hierarchical Principal Component Analysis 88
5.2.1.1 Top-level PCA model 88
5.2.1.2 Projection and clustering of bladder into latent space . 90
5.2.1.3 Second-level PCA 91
5.2.2 Linear mixed-effects models 94
5.2.3 Out-of-sample problem 94

5.2.4 Evaluation of prediction performance 96
5.3 Results 96
5.3.1 Hierarchical PCA representation 96
5.3.2 Evaluation of performance prediction with groundwork models . 101
5.4 Discussion 103
5.5 Conclusion 107

III Quantification of dose uncertainties for the bladder using PCA-based models 109

6 Quantification of dose uncertainties for the bladder in prostate cancer radiotherapy based on PCA-based models 111
6.1 Data 112
6.2 Methods 112
6.2.1 Principal component analysis 112
6.2.2 Estimation of the reference accumulated dose distribution 114
6.2.3 Mean and variance accumulated dose via integration 115
6.2.4 Mean and variance accumulated dose via Monte Carlo simulation 116
6.2.4.1 Dose confidence region for single fractions 118
6.3 Results 120
6.4 Discussion 126
6.5 Conclusion 129

Conclusion and perspectives 133

List of publications 141

Appendices 141

A Supplementary material for characterization of bladder motion and deformation 143

B Cluster center that minimizes the distance to data point in K-means clustering 145

C Elements of numerical analysis for solving mean and variance dose integrals 147

References 168

List of Figures

1.1 Male pelvic zone anatomy 24
1.2 T stages of prostate cancer 26
1.3 Multileaf collimator 28
1.4 Workflow of the treatment planning 30
1.5 Workflow of the treatment planning system 31
1.6 IMRT treatment plan 32
1.7 ICRU target volumes 32
1.8 Dose distribution to treat prostate cancer 33
1.9 Impact of random geometric uncertainties on the delivered dose 36
1.10 Workflow of the methodology used in this thesis. 41

2.1 Average values for the bladder and prostate volume in both databases. . 49
2.2 Overlay of a typical individual bladder registered to the template. . . . 50

3.1 Workflow of the method used to train the population-based model using voxel-wise representation 58
3.2 Accumulated mode variance P_q obtained by PCA 60
3.3 Sagittal view of the first three and 90-th mode 61
3.4 Scatterplot of the patients projected in the space spanned by the first two modes 61
3.5 Scatterplot of the observations available for one patient projected in the space spanned by the first two modes 62
3.6 Mean approximation error $\mathcal{M}$ as a function of the number of modes in the PCA model and left-out patients 63

4.1 Workflow of the method used to train the population-based model based on mixed-effects models 67
4.2 Workflow to estimate new structures based on the planning CT for a new patient 71
4.3 Relative mode variances obtained from the PCA in the training database 73
4.4 Mean approximation error $\mathcal{M}$ as a function of the number of modes in the Local PCA-ME model and left-out patients 74
4.5 3D sagittal views of the first three motion/deformation modes of the Local PCA-ME model 75

4.6 Scatterplot of the patients from the training database projected in the first two modes (black points) 76
4.7 3D sagittal views of PMs obtained for one patient in the training database as an out-of-sample patient 77
4.8 3D sagittal views of PMs obtained for one patient in the validation database as an out-of-sample patient 78
4.9 Average $dist_{intensity}$ values of observed and estimated PMs for patients in both databases. 79
4.10 Average Accuracy values of observed and estimated PMs for patients in both databases. 79
4.11 Average joint histograms of observed and estimated PMs for patients in the training and validation database 81

5.1 Workflow of the method used to train the hierarchical population-based model 89
5.2 Workflow to estimate new structures based on the planning CT for a new patient for the hierarchical-based PCA model 95
5.3 3D sagittal views of the first three motion/deformation modes in the top-latent space 97
5.4 Scatterplot of the patients projected in the top-latent space 98
5.5 3D sagittal views of the first three motion/deformation modes for the first cluster 99
5.6 3D sagittal views of the first three motion/deformation modes for the second cluster 100
5.7 Mean approximation error $\mathcal{M}$ of the Hierarchical PCA models in the training and left-out patients 100
5.8 Average $dist_{intensity}$ values of observed and estimated PMs for patients in the training database using Hierarchical PCA models. 101
5.9 Average $dist_{intensity}$ values of observed and estimated PMs for patients in the validation databases using Hierarchical PCA models. 102
5.10 Average $dist_{intensity}$ values of observed and estimated PMs for patients in the training database using Hierarchical PCA models. 103
5.11 Average Accuracy values of observed and estimated PMs for patients in the validation databases using Hierarchical PCA models. 104

6.1 Workflow of the method used to quantify dose uncertainties of the bladder 113
6.2 Pareto curve used to determine the number of modes to estimate dose uncertainties 117
6.3 Dose confidence region for single fractions 119
6.4 Relative mode variances obtained for the three patients 119
6.5 Intra-patient analysis for patients with on-treatment CBCTs 120
6.6 3D sagittal views of PMs obtained for each patient. Segmented prostate (blue), bladder (purple) and rectum (green) at the planning CT scan are overlaid. Patient's mean bladder (cyan) is also depicted. 122

6.7 Visualization of DVH uncertainties for Patient 1. (a) Mean (green) and accumulated DVHs (red) resulting from Monte Carlo (MC) simulation are depicted. Planned DVH (blue) and DVH (cyan) obtained from the patient's mean bladder shape are also illustrated. (b) DVH uncertainties resulting from observed and estimated bladder structures (rescaled to the total dose) in the MC simulation. (c) DVH uncertainties resulting from observed and estimated bladder structures (rescaled to the total dose) in the dose integration and confidence region (CR). 123
6.8 Visualization of DVH uncertainties for Patient 2. (a) Mean (green) and accumulated DVHs (red) resulting from Monte Carlo (MC) simulation are depicted. Planned DVH (blue) and DVH (cyan) obtained from the patient's mean bladder shape are also illustrated. (b) DVH uncertainties resulting from observed and estimated bladder structures (rescaled to the total dose) in the MC simulation. (c) DVH uncertainties resulting from observed and estimated bladder structures (rescaled to the total dose) in the dose integration and confidence region (CR). 124
6.9 Visualization of DVH uncertainties for Patient 3. (a) Mean (green) and accumulated DVHs (red) resulting from Monte Carlo (MC) simulation are depicted. Planned DVH (blue) and DVH (cyan) obtained from the patient's mean bladder shape are also illustrated. (b) DVH uncertainties resulting from observed and estimated bladder structures (rescaled to the total dose) in the MC simulation. (c) DVH uncertainties resulting from observed and estimated bladder structures (rescaled to the total dose) in the dose integration and confidence region (CR). 125
6.10 3D sagittal views of $\sigma_{cum,MC}$ for each patient. Segmented prostate (cyan), bladder (purple) and rectum (red) at the planning CT scan are overlaid. 126
6.11 DVH differences between the reference and estimated accumulated doses for all the three patients. (a) DVH differences between the reference accumulated $DVH_{cum,ref}$ and the mean accumulated $DVH_{cum,MC}$ via MC simulation. (b) DVH differences between the accumulated DVH $DVH_{cum,int.3}$ obtained with dose integration over the first three modes and the mean accumulated $DVH_{cum,MC}$ obtained via MC simulation. . 128

A.1 Boxplot of average prostate volume in the training database 144

C.1 Visualization of the Gaussian distribution of the first mode 148
C.2 Visualization of the multivariate Gaussian distribution of the first two mode 151

List of Tables

1.1 Treatment options for localized prostate cancer. 29
1.2 GETUG dose-volume constraint recommendations for target volumes and OARs in prostate cancer radiotherapy 34
1.3 Methods developed in order to quantify geometrical uncertainties. . . . 35
1.4 Methodologies developed for statistical models of organ motion and deformation based on PCA. 38
1.5 List of divergence and convergence points between the developed methodologies to describe organ motion and deformation based on PCA. 42

2.1 Population average of parameters describing bladder and prostate volumes in both databases. 50

4.1 Averaged values from the metric $dist_{intensity}$ for two patients between estimated and observed PMs. 79
4.2 Averaged values from the metric Accuracy for two patients between estimated and observed PMs. 80
4.3 Number of patients exhibiting significance difference using the Wilcoxon rank sum test in both databases. 80
4.4 p-values of the Wilcoxon rank sum tests for the variance distributions between PCA models in both databases. 81

5.1 Error metrics of the classifier for both hierarchical models 101
5.2 Number of patients exhibiting significance difference using the Wilcoxon rank sum test in both databases between the Local PCA and HR-ML PCA-ME models. 105
5.3 p-values of the Wilcoxon rank sum tests for the variance distributions between PCA models in both databases the Local PCA and HR-ML PCA-ME models. 105

6.1 Mean and standard deviation of the Dice Scores (DS) obtained following DIR for each bladder and estimated bladder structure. 121
6.2 Relative errors from the metric $dist_{dose}$ for the mean and variance accumulated dose via integration for Patient 1. 127

6.3 Relative errors from the metric $dist_{dose}$ for the mean and variance accumulated dose via integration for Patient 2. 127
6.4 Relative errors from the metric $dist_{dose}$ for the mean and variance accumulated dose via integration for Patient 3. 127

Acronyms

3D-CRT 3D conformal radiotherapy. 27

ASAP atypical small acinar proliferation. 23

CBCT cone beam computed tomography. 29, 30

CT computed tomography. 13, 23, 26, 30

CTV clinical Target Volume. 30

DRE digital rectal examination. 23

DVH dose-volume histogram. 14, 17, 31

EBRT external beam radiotherapy. 13, 21, 26

GI gastrointestinal. 14

GS gleason score. 23–26

GTV gross Tumor Volume. 30

GU genitourinary. 14, 15

IGRT image-guide radiotherapy. 14, 21, 29, 30, 34

IMRT intensity-modulated radiotherapy. 14, 21, 27, 28, 32, 34

ME mixed-effects. 15

MRI magnetic resonance image. 23, 30

NTCP normal tissue complication probability. 14

OARs organs at risk. 13, 14, 26, 29, 34

PCA principal component analysis. 15, 17, 41

PET positron emission tomography. 30

PIA prostatic intraepithelial neoplasia. 23

PSA prostate-specific antigen. 23

PTV planning target tolume. 30

TPS treatment planing system. 13, 27–29

TRUS transrectal ultrasound. 23

Part I

Problem definition, objectives and clinical context

Chapter 1

Introduction: clinical context and treatment uncertainties in prostate cancer radiotherapy

This chapter introduces the clinical context of prostate cancer treated with EBRT. It also introduces the research problem and objectives of this thesis, and the workflow methodology used in this thesis. We firstly introduce a description of the prostate anatomy and nearby organs in the pelvic zone. Subsequently, we briefly describe the diagnosis and curative methods, and the main concepts of EBRT. We finally introduce a review of approaches developed to model inter-fraction motion and deformation of pelvic organs.

1.1 Prostate cancer

The prostate is a gland that plays an important role in the male reproductive system. Some of its functions are to produce part of the alkaline fluid that makes up semen and enables ejaculation by contracting its muscles. The prostate is located in the pelvic cavity, below the bladder and in front of the rectum. The seminal vesicles, two glands that make most of semen, connect behind the prostate, see Fig. 1.1.

The prostate changes size over time, growing mostly during puberty, due to a rise of male hormones. In adults, it usually remains stable in the same size or grows slowly, so the average prostate weight is approximately $20g$. However, the prostate sometimes gets bigger as men get older, leading to an enlarged prostate. This is called benign prostatic hyperplasia (BPH) or benign enlargement of the prostate (BPE). Prostate enlargement is usually benign, but men can have an enlarged prostate and prostate cancer at the same time.

The prostate cancer is the most common cancer amongst the men population in most developed countries. According to the World Health Organization (WHO), it was the second most common cancer among men with 1.112 million of diagnosed cases in 2012 [1]. In males, prostate cancer is the most common cancer in France (73.609 cases

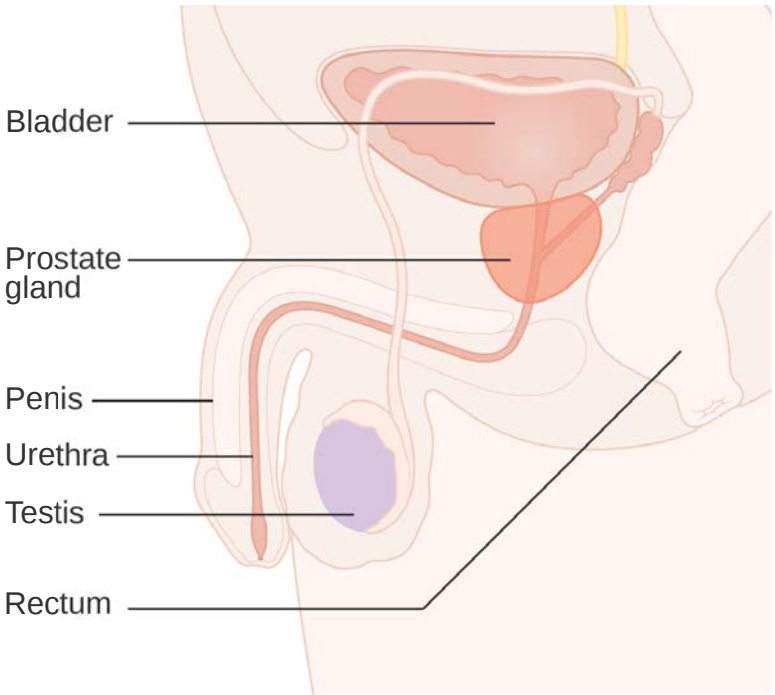

Figure 1.1: Visualization of the male pelvic zone anatomy. Source *wikimedia*

in 2014) and in Colombia (9564 cases in 2014). Meanwhile, it is the third most common cause of cancer deaths in males in both countries (9.3% and 7.1% in France and in Colombia in 2014, respectively) [2–4]. It develops mainly in men over the age of 50, and it usually grows slowly without causing any symptoms or problems over a men' lifetime. However, some men may have cancer that grows quickly, likely resulting in health problems. About 42% in fifty-year-old men have developed histological evidence of cancerous cells in the prostate; 9.5% of these will develop an aggressive form of cancer, and 2.9% will die from prostate cancer [5, 6]. Medical treatments are thus needed to prevent or delay the tumor from spreading outside the prostate. For a complete review on prostate cancer diagnosis, staging and treatments (with curative intent), see guidelines of the European Association of Urology [7, 8].

1.1.1 Diagnosis and staging of prostate cancer

The biopsy is the only procedure that can fully confirm the diagnosis of prostate cancer [9, 10]. It consists of introducing a needle — through the rectum wall into the prostate — in order to remove small prostate tissues. Biopsy samples are then sent to a lab to be examined under a microscope to determine whether they have cancer cells or not. A grade called grade score (GS) is subsequently assigned based on how much cancer looks like normal prostate tissue, according to the Gleason system [11, 12]. Grade 1 means that the cancerous tissue looks very much like normal prostate tissue, i.e the glands are

small, well-formed, and closely packed. Meanwhile, Grade 5 means that the cancerous tissue does not have any or only a few recognizable glands, and grades between 2 and 4 mean that tissue has features in between both extremes. Since prostate cancers may have areas with different grades, the pathologist assigns a primary grade to the dominant pattern of tumor (greater than 50% of the total pattern), and a secondary grade to the next-most frequent pattern (less than 50%, but at least 5% of the pattern). The GS is then obtained by summing the primary and secondary grade. For example, if the primary grade was 3 and the secondary tumor grade was 4, the Gleason score would be $3 + 4 = 7$.

In addition to the biopsy, there are two methods used to suspect the presence of cancer: the prostate-specific antigen (PSA) test and the digital rectal exam (DRE) [13, 14]. The PSA test measures the level of prostate-specific antigen which is a protein produced by prostate cells. Meanwhile, DRE test consists of inserting a gloved and lubricated finger into the rectum to feel any bumps or hard areas on the prostate, and it can help to determine whether tumor is only in one or both sides of the prostate. Most healthy men have PSA levels under 4 ng/ml of blood, and it usually goes above 4 when prostate cancer develops. However, PSA can also be raised in a man that has other medical conditions like BPH, prostate infection, exercise, or sex. The PSA and DRE test are not thus 100% accurate, and they can have abnormal results in a man that does not have cancer (i.e false-negative), or normal results in a man that does have cancer (i.e false-positive). For example, about 15% of men with a PSA below 4 will have prostate cancer on a biopsy. As a result, other tests can be undergone to avoid false-positives, such as those based on medical image (MRI, bone scan or CT), medical history or tests (TRUS, PIA or ASAP) [15, 16].

The stage or extent of a cancer is one of the most important factors in choosing treatment options and predict prognosis [8, 17, 18]. The objective is to determine how far cancer has spread. The most widely used staging system for prostate cancer is the TNM classification system, which is an international standard that can be adapted to each type of cancer. The TNM system assesses the tumor (T category), lymph nodes (N category) and secondary cancer (metastases- M category). The stage is determined based on the prostate biopsy results (including the Gleason score (GS)), PSA level, and any other exams that are done. The general outline for the T stages is given as follows:

- T: size or extent of the primary tumor
  - T1: tumor present, but not detectable with imaging or clinically:

    T1a: tumor is less than 5% of prostate tissue resected during a transurethral resection of the prostate (TURP) for BPH.

    T1b: tumor is more than 5% of prostate tissue resected in a TURP.

    T1c: tumor is found in a biopsy performed due to a high level PSA.
  - T2: tumor can be felt in a DRE or seen with imaging clinically, but it still appears to be confined to the prostate.

    T2a: tumor is in half or less of one (left or right) of the prostate lobes.

T2b: tumor is in more or half one (left or right) of the prostate lobes, but not both.

T2c: tumor is in both sides of the prostate lobes but still in the prostate capsule.

- T3: tumor has spread outside the prostate and may have spread to the seminal vesicles.

  T3a: tumor has spread outside the prostate but not to the seminal vesicles.

  T3b: tumor has spread to the seminal vesicles.

- T4: tumor has invaded other nearby structures (other than the seminal vesicles).

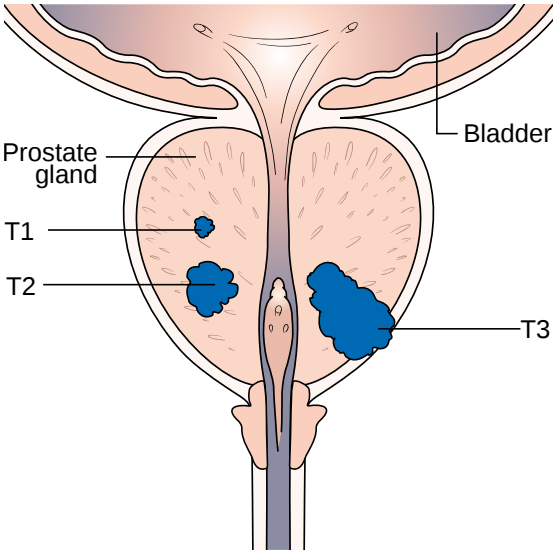

Figure 1.2: Diagram showing the T1-3 stages of prostate cancer. Source *Cancer Research UK/Wikimedia*

Fig. 2.1 illustrates a diagram showing the T stages of prostate cancer. Once the TNM categories are defined, this information is combined with the results of the prostate biopsy, the Gleason score, the PSA level, and any other exams done to determine an overall staging, which is divided into four stages, as follows:

- Stage I (low risk and confined): T1 to T2a, GS$\leq$ 6, PSA$\leq$ $10ng/mL$.
- Stage IIA (intermediate risk and confined): T2b or GS= 7 or $10ng/mL$ $\leq$PSA$\leq$ $20ng/mL$.
- Stage IIB (high risk and confined): T2c or GS$\geq$ 8 or PSA$\geq$ $20ng/mL$.

- Stage III (high risk and non-confined): T3, any GS, any PSA.
- Stage IV (metastasis): any GS, any PSA, T4.

Once the staging procedure is carried out, treatment options are considered and the prognosis is predicted.

1.1.2 Curative treatments for localized prostate cancer

There are several treatment options for localized prostate cancer with comparable outcomes but different side effects [8]. Table 1.1 illustrates a classification of treatment options according to the risk grade given during staging phase [18]. A short description of these treatment options is given as follows:

- Surgery. Men in good health whose tumor is still confined in the prostate may be treated with surgery to remove the tumor. Radical prostatectomy is the main type of surgery, which consists of removing the entire prostate gland plus surrounding tissue and the seminal vesicles. However, erectile dysfunction following radical prostatectomy is a common complication due to nerve damage after the procedure [19].
- Watchful waiting or active surveillance. Because prostate cancer is often slow-growing, these options are usually recommended for some older men without serious health problems. Both treatment options seek to monitor tumor growth and avoid having unnecessary treatment. However, key differences rely on the type of follow-up and medical tests used to monitor prostate cancer. For example, active surveillance implies more regular doctor visits, hospital tests such as PSA tests, DRE exams, biopsies, or MRI scans about every six (6) months.
- Hormone therapy. Prostate cancer grows when male hormones like testosterone and dihydrotestosterone (DHT) stimulated the tumor. Hormone therapy thus seeks to stop male hormones from reaching prostate cancer cells. However, its purpose is not to cure cancer but rather to keep it under control slowing down its growth.
- Radiotherapy. This option uses high-energy x-rays or other types of radiation to kill cancer cells. The main two types of radiotherapy are EBRT and brachytherapy. Brachytherapy consists of inserting a source of radiation inside or next to the tumor, while EBRT uses X-ray beams to irradiate prostate gland from outside the body.

1.2 External beam radiotherapy in prostate cancer

More than two thirds of patients diagnosed with prostate cancer will be treated with EBRT, which is mostly used if prostate cancer is between stage TI and T3. EBRT uses

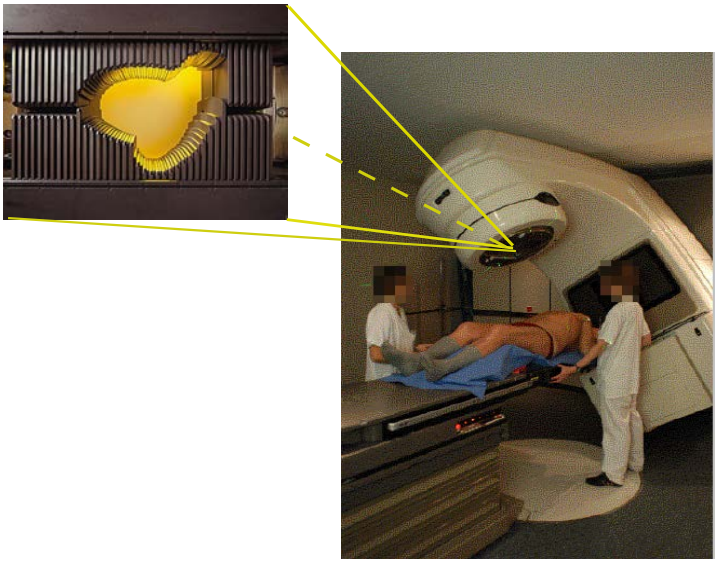

Figure 1.3: Patient lying on a table of a linear particle accelerator (right) and multileaf collimator (left, manufactured by Varian, 120 leafs).

X-ray beams to irradiate prostate gland and seminal vesicles in order to kill cancerous cells (tumor control) while sparing neighboring healthy organs classified as OARs. The radiation dose is delivered in several sessions in order to allow healthy tissue to recover and increase tumor damage by reoxygenation. A small dose called fraction is thus delivered in each session. For example, if a dose of 80 Gy is prescribed to the prostate, fractions of 2 Gy delivered over five (5) days in eight weeks are the conventional treatment schedule. The radiation units are expressed in Grays, abbreviated as Gy, which represents 1 Jule/Kg [18]. Dose fractionation is used to increase the therapeutic ratio, i.e. it enables both normal tissues to repair between fractions and increase tumor damage by reoxygenation and redistribution.

Before treatment starts, the radiotherapy team will carefully plan the proper radiation dose, fractionation scheme and correct angles of the beams. This session, known as treatment planning, starts by acquiring a computed tomography (CT) scan on the zone being irradiated. This scan shows the patient's organs which are delineated by an expert (e.g. prostate, seminal vesicles, bladder, femoral heads, and rectum). This information is then exported to a TPS, which is a software used to generate the prescribed dose, known as the planning dose. The prescribed dose is a three-dimensional map that relates every point within patient with a level of dose. The following step is then to set up the linear accelerator to deliver the planning dose using the selected fractionation scheme, whereby each treatment fraction lasts only a few minutes. The patient is fitted with a plastic mold on a table that is below the linear particle accelerator for each fraction during treatment. The aim is to keep the patient in the same position as that of the planning CT, see Fig. 1.3. Markers can be implanted on the patient's skin

Treatment	Low risk (T1-T2a, GS ≤ 6) PSA $\leq 10ng/mL$)	Intermediate risk (T2b, GS= 7 $10ng/mL \leq$PSA$\leq 20ng/mL$)	High risk (T2c-T4, GS≥ 8 PSA$\geq 20ng/mL$)
Active surveillance	✓		
Brachytherapy	✓	✓	
Prostatectomy	✓	✓	
EBRT	✓	✓	✓
Watchful waiting	✓	✓	✓
Hormone therapy			✓

Table 1.1: Treatment options for localized prostate cancer.

or prostate to align him at each irradiation session. It is worth mentioning that a few days or weeks may have passed between the planning and start of the treatment itself. During this time, physicists and clinician decide the areas to be irradiated or spared using a TPS. Fig. 1.4 depicts the treatment planning workflow in radiotherapy.

1.2.1 Irradiation techniques

There are two types of irradiation techniques: 3D conformal radiotherapy (3D-CRT) and intensity modulated radiotherapy (IMRT). In both techniques, the fluence (radiation energy per unit area) of the radiation beams are modulated to match the prostate shape as closely as possible and optimally avoid dose being delivered to the surrounding healthy tissues. In 3D-CRT, between five to nine convergent beams are used to conform the target volume via the modulation of a multileaf collimator located at the linear accelerator output (see Fig. 1.3). The multileaf collimator is made up of metal bars called leaves that block part of the radiation beam. These leaves are arranged in opposing pairs, and they are positioned under computer control in order to conform the target shape. IMRT also uses multileaf collimator to modulate the fluence, but it can provide non-uniform dose distribution and control independently the beam intensity in different regions [18]. IMRT appeared with the arrival of inverse-planning software that enables us to obtain concave iso-doses, a property desired mainly at the prostate-rectum junction. IMRT has become the standard irradiation technique in 30% of French treatment centers [2], including at the Centre Eugène Marquis (from 2003 onwards) that provided the medical support and background to this thesis. Fig. 1.5 shows the work-flow of the Direct Machine Parameter Optimization with RayMachine using the Pinnacle TPS manufactured by Phillips. As is illustrated, IMRT dose is derived by an inverse-planning software that starts from the end-product (i.e. desired dose) and ends with the input (i.e. fluence profile). The desired dose is represented as a mathematical cost function f to be optimized with some constraints. The input parameters of this function include leaf positions, some weights (w), and the fluence matrix (deposition matrix). Fig. 1.6 depicts a planning dose to treat prostate cancer with IMRT, and demonstrates the concave shape of the iso-doses.

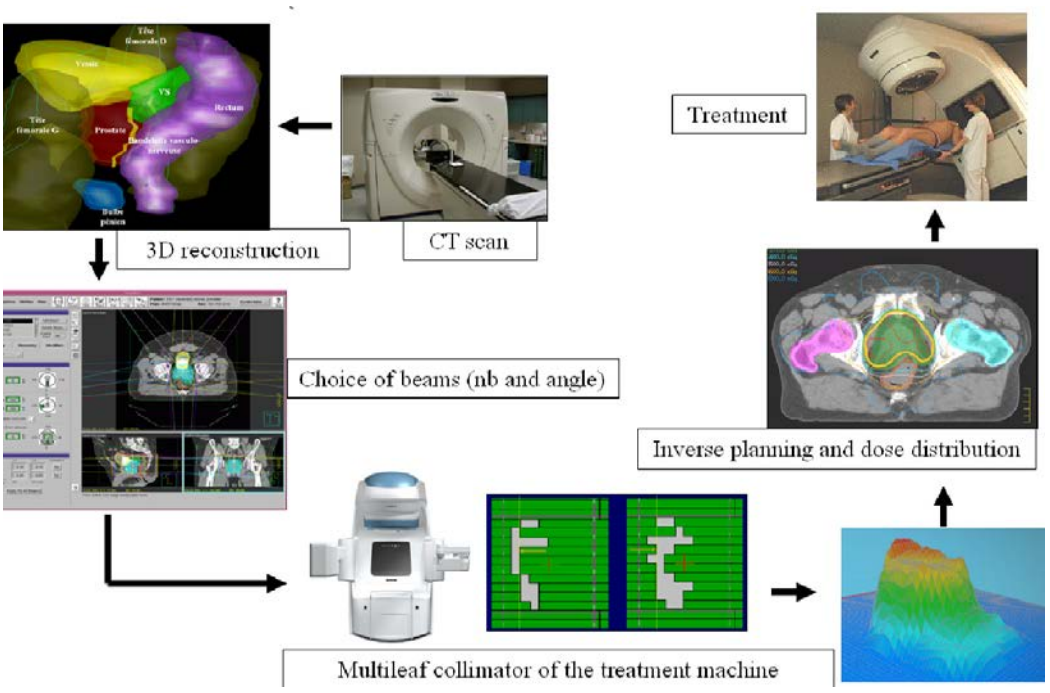

Figure 1.4: Treatment planning workflow for external beam radiotherapy of the prostate.

1.2.2 Image guided radiotherapy

Image-guided radiotherapy (IGRT) is defined as frequent imaging in the treatment room that allows treatment decisions to be solved [21]. IGRT then uses different imaging techniques, ranging from planar to fluoroscopy to X-ray images, to check that the actual treatment delivered matches with that which was planned [18, 22]. IGRT has played an important role in the evolution of radiotherapy by achieving important accomplishments such as reducing the uncertainty of the exact position of tumor and OARs, and improving the precision of the delivered dose. IGRT has also enabled the development of adaptive radiotherapy based on the assessment of information obtained from daily images.

The most important problem to be solved in IGRT is organ motion during treatment [22]. In prostate cancer radiotherapy, organ motion and deformation mostly arise from geometric variations in the prostate, bladder, and rectum. These anatomical variations can lead to an under-radiation of the target volume, or an over-radiation to OARs, decreasing the local control in the former and increasing the risk of toxicity in the latter. Localizing the tumor and OARs is thus a requirement that has resulted in the development of new image modalities (with new devices integrated to linear accelerators), such as kilovolts (kV), megavolts (MV), ultrasound or electromagnetic detection. The most common modalities in radiotherapy are: cone beam computed tomography (CBCT), computed tomography (CT), magnetic resonance imaging (MRI), MR-linac,

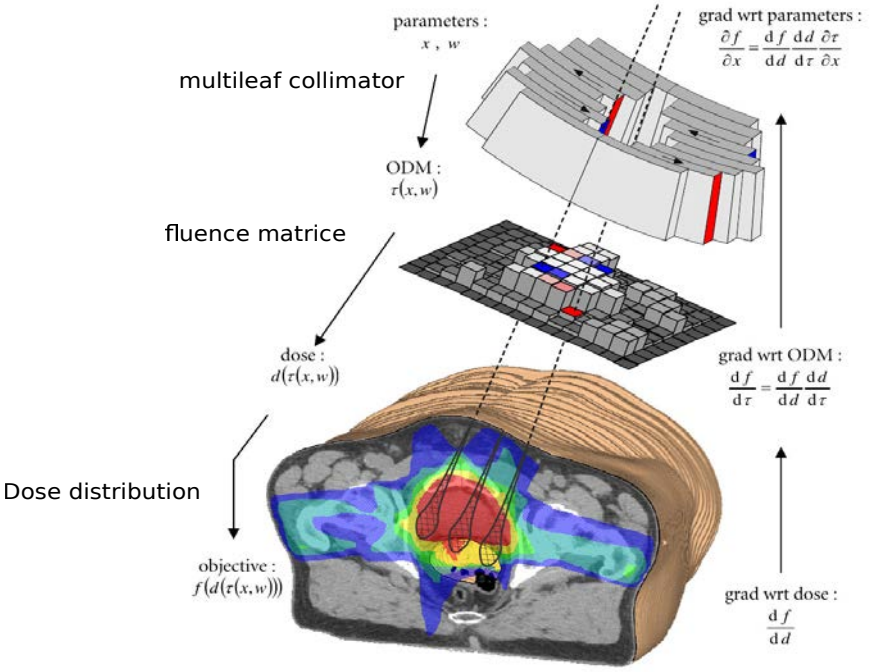

Figure 1.5: Workflow of the Direct Machine Parameter Optimization with RayMachine using Pinnacle® TPS manufactured by Phillips. (image modified from [20])

and positron emission tomography (PET). CT enables a 3D image of the internal structure of an object to be obtained without cutting from many X-ray images taken from different angles. CT provides detailed cross-sectional anatomy of organs and 3D tumor information (see Fig. 1.6) [18, 22]. CBCT is also an X-ray CT, but the X-rays taken with this modality are divergent, forming a cone. The voxel value of the CBCT thus depends on the position in the image volume, rather than its tissue density. Nevertheless, CBCT has become an important tool in IGRT to position patients, whose reconstructed 3D image is compared to the planning CT scan.

1.3 Current practices and treatment plan evaluation in prostate cancer radiotherapy

According to the International Commission on Radiation Units and Measurements (ICRU) [23], there are five target volumes defined in radiotherapy: gross tumor volume (GTV), clinical target volume (CTV), planning tumor volume (PTV), and treated and irradiated volume. The CTV represents the main target volume to be irradiated in radiotherapy, receiving all the prescribed dose. The CTV contains the primary tumor (called GTV) and/or sub-clinical malignant disease that has to be eradicated in order to control the tumor. Fig. 1.7 shows the target volumes set by ICRU in order to define

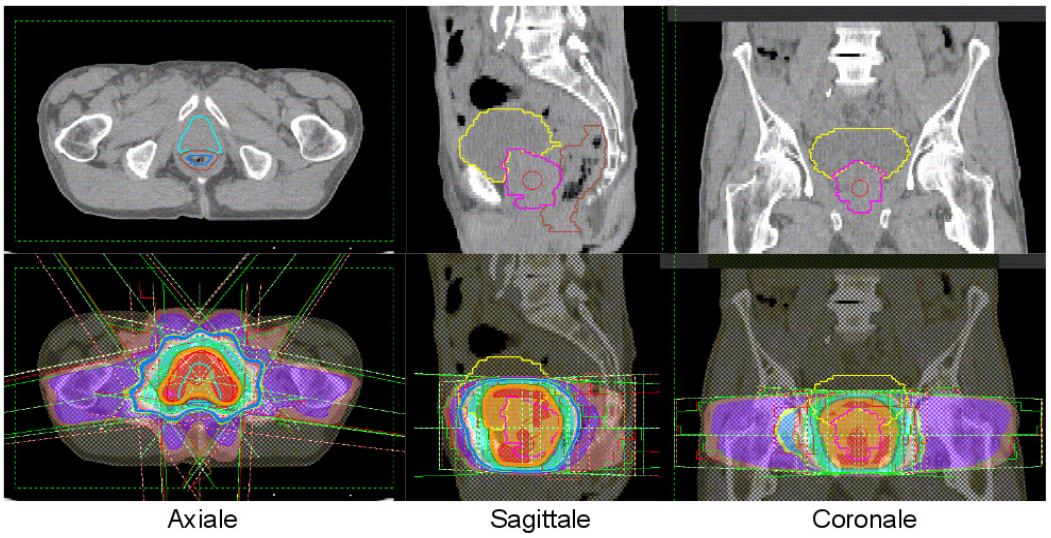

Figure 1.6: Above: Planning CT scan and the main structures delineated (prostate, bladder and rectum). Below: IMRT planning dose distribution.

a common international language to delineate tumors. 3D safety margins around the CTV define the planning target volume (PTV). This target volume is set in order to ensure that the prescribed dose is actually delivered to the CTV, even if it does experience geometric variations in organs during a fraction or between fractions. In prostate cancer radiotherapy, it is not possible to accurately define the GTV with current imaging techniques [18]. As a result, it is standard practice to define a CTV that includes the whole prostate and any possible extension of the seminal vesicles. The target volume then includes the prostate and base of seminal vesicles in the low risk group, while the prostate and entire seminal vesicles in the other risk groups [18]. The PTV is defined by an isotropic margin of $1cm$ around the CTV, but the posterior the PTV region is reduced to $5mm$ in order to limit the dose to the rectum.

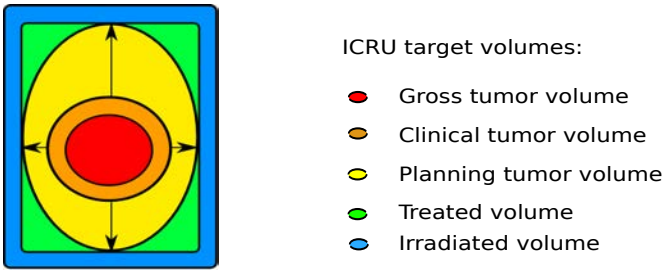

Figure 1.7: Diagram representation of ICRU target volumes. This diagram was made following the same idea of target volume definitions from ICRU (1993) Prescribing, Recording and Reporting Photon Beam Therapy. ICRU report 50.

Planned dose distributions are usually evaluated by means of a two-dimensional graph that relates the percentage of the organ volume that receives a dose equal to, or lower than, a certain value. This graph is called a dose volume histogram (DVH). The ideal scenario is then to have 100% of the CTV receiving the total prescribed dose, while OARs receiving 0% of the dose, see Fig. 1.8.

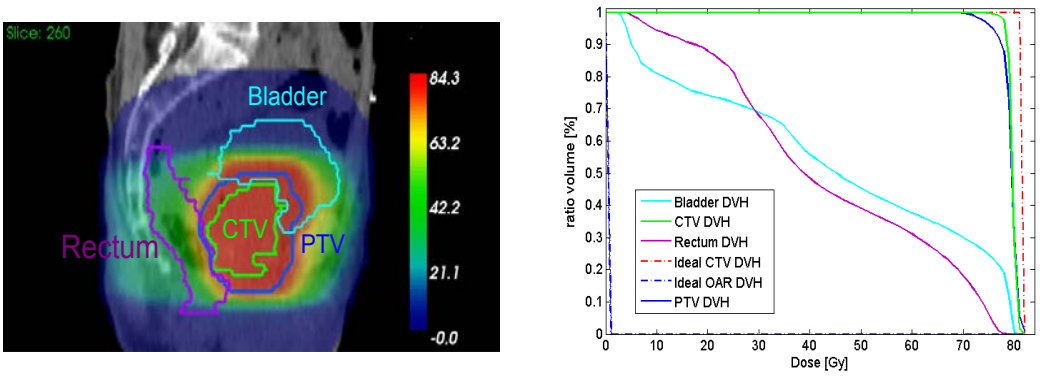

Figure 1.8: Example of dose distribution used to treat prostate cancer. The figure on the left shows a sagittal view of the planning CT with the main delineated organs, target volumes and dose in colorwash. Meanwhile, the figure on the right shows the DVH of the CTV, PTV, bladder and rectum compared with ideal CTV and OAR DVH.

Table 1.2 shows dose-volume constraints recommended by Groupe d'ètude des tumeurs uro-gènitales (GETUG) for target volumes and OARs in prostate cancer radiotherapy.

1.4 Random geometric uncertainties in prostate cancer radiotherapy

In radiotherapy geometric uncertainties may be systematic or random. Systematic uncertainties may result from organ delineation errors in the planning CT (either due to the limited CT resolution or different human interpretations), misalignments in the patient repositioning with respect to the planning phase [24], or inaccurate placing of devices, among others [18]. Meanwhile, random uncertainties mostly arise from unpredictable and involuntary anatomical changes in patient's organs during the delivering of a dose fraction or between fractions [18, 25]. For example, in prostate cancer radiotherapy, the prostate can be displaced or compressed by filling and emptying the bladder and/or rectum; SV volume can also vary during treatment, between 30% and 50% [26]. These anatomical changes in organs thus introduce random geometric uncertainties that make their positions and shapes unknown within and between fractions, reducing the treatment quality.

IMRT has enabled us to deliver complex dose distributions with higher doses and sharp concave iso-doses that conform target volumes well. However, IMRT dose distri-

Table 1.2: GETUG dose-volume constraint recommendations for target volumes and OARs in prostate cancer radiotherapy

Volume	Notation	Definition
PTV	$D_{min} > 90\%$	Minimum dose to PTV must be higher than 90% of the prescribed dose.
	$V_{95\%} > 90\%$	The volume receiving at least 95% of the prescribed dose must be higher than 90% of the total volume.
Bladder wall (7mm)	$D_{max} < 80\,Gy$	The average dose to 1.8 cm^3 must be always lower than 80Gy.
	$V_{70} < 50\%$	The volume receiving at least 70 Gy must be lower than 50%.
Rectal wall (7mm)	$D_{max} < 76\,Gy$	The average dose to 1.8 cm^3 must always be lower than 76 Gy.
	$V_{72} < 25\%$	The volume receiving at least 72 Gy must be lower than 25%.
Femoral heads	$V_{55} < 5\%$	For each femoral head, the volume receiving at least 55 Gy must be lower than 5%.

butions are only made using the planning CT scan, where organ structures observed on this image does not hold during treatment, either caused by systematic and/or random geometric uncertainties [26, 28–32]. For example, Fig. 1.9 depicts the planned and accumulated DVHs for a patient treated for prostate cancer, showing an overdose on the bladder caused by its changes in volume during treatment. These geometric uncertainties can thereby make the beams miss the target volume and hit the healthy organs increasing the probability of developing side-effects.

There are some efforts made to overcome these geometrical uncertainties. For example, systematic uncertainties can significantly be reduced by means of body cast, skin tattoos, or fiducial markers, whose position can be determined in three dimensions using IGRT. Translational errors can thus be reduced to $1\,mm$ and rotational errors to $1°$ [18]. Safety margins are also introduced around the CTV upon treatment planning, in order to enlarge irradiated area [23]. Nevertheless, this also means including portions of OARs that may be highly irradiated, potentially resulting in adverse events affecting patient's organ functions (hematuria, cystitis rectal bleeding, fecal incontinence, among others). Although new technologies — such as image guided radiotherapy (IGRT), fiducial markers and intensity-modulated radiation therapy (IMRT) — have enabled us to determine organ location and deliver higher doses with sharp iso-doses, random geometric uncertainties still have an impact during treatment. In the case of IGRT, on-line adaptive imaging has arisen as a promising solution, but integration in real time of on-line imaging and dose adaptation while fraction are performed is task that is not

Method	Advantages	Disadvantages
Serial imaging measurements, fiducial markers, OAR margins, rigid-body motion	∗ Quick implementation. ∗ Easy to interpret. ∗ Systematic and random uncertainties assumed to be normally distributed. ∗ Population-based approach.	∗ Organ deformation is not considered. ∗ High number of CT scans per patient. ∗ Scalar variables like volume, translation or rotation are used to describe organ shape variation.
Organ shape parametrization	∗ Organ changes in size and shape are considered. ∗ Population-based approach. ∗ Probability distributions of geometric parameters are estimated ([27]).	∗ Slice-by-slice parametrization. ∗ The database should represent the patient population. ∗ Observed deformations can only be reproduced.
Biomechanical models	∗ Organ motion and deformation are considered. ∗ Biomechanical properties are introduced.	∗ Individual-based approach. ∗ Limited by the required number of CT scans per patient. ∗ Organ motion and deformation are assumed to be uniformly distributed between two measured geometries.
Non-parametric statistical models	∗ Organ motion and deformation are considered. ∗ Population approach. ∗ Non-statistical distribution is assumed.	∗ Slow convergence of the estimated non-parametric distribution. ∗ Limited by the requited number of CT scans per patient.

Table 1.3: Methods developed in order to quantify geometrical uncertainties.

feasible or too expensive. As a result, the dosimetric variables obtained from the planning CT are very poor surrogates for the actual-delivered dose [33–35], and random geometrical uncertainties still have an impact during treatment, reducing its quality.

Several approaches have been developed in order to quantify geometrical uncertainties produced by organ variations between fractions, including: serial imaging measurement of the organ during treatment course [26,36], fiducial markers [28,37], margins of organs at risk (OAR) [38,39], rigid-body motion [25,29,40–43], parametrization of the

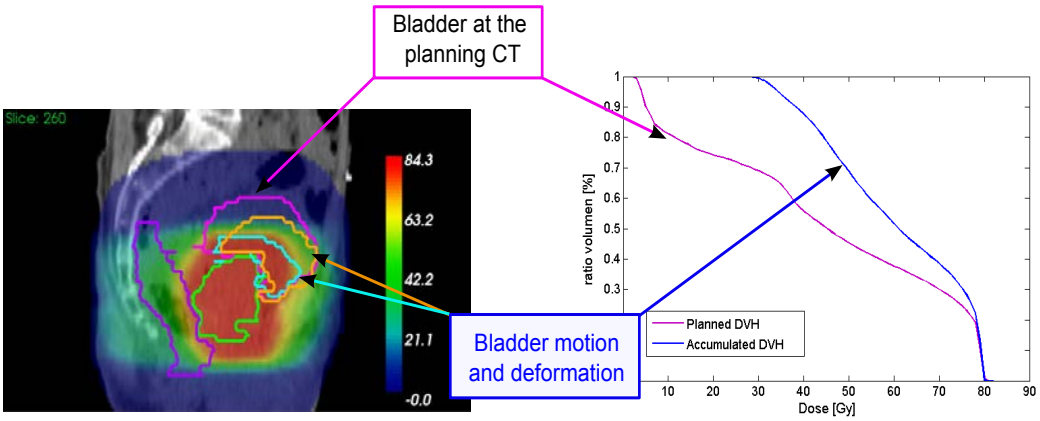

Figure 1.9: Impact of random geometric uncertainties on the delivered dose on a bladder. The figure on the left shows the CTV, bladder and rectum delineated at the planning CT with the planning dose. It also shows the bladder delineated at two CT scans obtained during treatment. The figure on the right shows the bladder DVH obtained with the planning dose (planned DVH), and the bladder DVH obtained by dose accumulation during treatment (accumulated DVH).

organ shape [27, 44, 45], as well as biomechanical [46, 47] and statistical models [48–56]. Table 1.3 provides a short description of advantages and disadvantages of the developed approaches to quantify random geometric uncertainties.

From statistical models, a method based on weighted scenarios of the fundamental directions of geometric variability has been introduced [54, 57]. These directions of variability, called motion/deformation modes, were obtained by applying principal component analysis (PCA) to a data set of (pre-)treatment organ geometries, usually parameterized by a set of corresponding surface points. This approach known as a point-distribution model (PDM) has also been applied in statistical shape models and organ segmentation [58–60]. The idea of PCA-based models is to represent any organ structure x as a linear combination of q dominant directions called modes:

$$x \approx \hat{x} = \bar{x} + \sum_{k=1}^{q} z_k \, \varphi_k, \tag{1.1}$$

where $\bar{x}$ is the mean shape vector, φ_k is the k-th mode, $z_k = (x - \bar{x})^T \varphi_k$ is the projection of x along mode φ_k. The scalar z_k may be interpreted as a "measure" of geometric variability around the mean shape. These modes were derived by diagonalization of a data matrix, called the covariance matrix, whose columns were made of patient's motion/deformation vectors (i.e. vectors that describe the observed geometric variation of the organ at the on-treatment CTs/cone-beam CTs (CBCTs) relative to the mean shape). Denoting the observed organ structure at the i-th CT as x_k, the empirical covariance matrix $\mathbf{C}_{empirical}$ is defined as follows:

$$\mathbf{C}_{empirical} = \frac{1}{n-1}\sum_{i=1}^{n}(x_i - \bar{x})(x_i - \bar{x})^T = \mathbf{UDU}^T \tag{1.2}$$

where $\mathbf{U}$ is a matrix composed of eigenvectors φ_k of $\mathbf{C}_{empirical}$, and $\mathbf{D}$ is the diagonal matrix constructed from its corresponding eigenvalues λ_k, i.e. $\mathbf{C}_{empirical}\varphi_k = \lambda_k\varphi_k$. New organ geometries can then be generated by adding a weighted sum of a few dominating modes to the mean organ shape, where each weight obeyed a Gaussian distribution with mean of zero and the corresponding eigenvalue as variance. PCA-based models thus have the following advantages: i) organ motion and deformation are parameterized by few dominating directions; ii) the number of model parameters is defined according to a pre-fixed error; iii) geometric uncertainties can be quantified; iv) PCA enables the reduction of dimensionality of high-dimensional data (repeated CTs/CBCTs) while preserving the most important information. Table 1.4 provides a short description of developed methodologies for statistical models of organ motion and deformation based on PCA.

PCA-based motion/deformation models were initially used by Söhn et al. [57] for modeling individual geometric variations between fractions of the rectum, bladder, and prostate. The main goal was to estimate the patient's variance along each mode of geometric variability. These modes were derived by diagonalization of a data matrix, called the covariance matrix, whose columns were made of patient's motion/deformation vectors (i.e., vectors that describe the observed geometric variation of the organ at the on-treatment CTs/cone-beam CTs (CBCTs) relative to the mean shape). New organ geometries were then generated by adding a weighted sum of a few dominating modes to the mean organ shape, where each weight obeyed a Gaussian distribution with mean of zero and the corresponding eigenvalue as variance. PCA has also been applied to generate individual 4D statistical models for organs undergoing respiratory motion like the lung, liver, and heart [52,53,63]. The same method was in turn applied to describe the geometric variations of organs like prostate, seminal vesicles, and pelvic lymph nodes [51].

However, this individual-based methodology was limited by the required number of CT scans per patient for training the model. In clinical practice, only one CT scan is available at the planning treatment for a typical patient, and on-treatment CTs/CBCTs are seldom available during treatment. Budiarto et al. [54] thus proposed a population-based method that learned the geometric variations from a population database seeking to infer the possible organ variations for a typical patient despite his small number of CTs/CBCTs. Budiarto et al. [54] applied his method to describe clinical target volume (CTV) motion and deformation between fractions in prostate cancer using a longitudinal database. It is worth mentioning that longitudinal data set consists of repeated observations of a set of homologous objects or variables at several time points [64,65]. In our context, it corresponds to repeated observations of the organ at different fractions for a patient population. This methodology was also applied to model motion

Method	Advantages	Disadvantages
Individual-based model [50–53]	Characterization and prediction of organ motion and deformation.	∗ Limited by the required number of CT scans per patient. ∗ Organ parametrization via a set of surface points. ∗ A mesh relaxation process is needed to achieve a set of surface corresponding points.
Population-based model [54–56]	∗ Few number of CT scans per patient. ∗ Voxel-wise implementation without using a mesh relaxation process [56]. ∗ Not suitable to longitudinal data: modes are biased to the most observed directions in the population.	It is based on a cross-sectional analysis, where the inherent correlation of intra-individual observations is not considered.
Population-based model + Longitudinal analysis [61, 62]	∗ Organ shapes represented with less variables. ∗ A mesh relaxation process is not needed. ∗ Intra-patient variance is characterized from the total variance. ∗ Patient-specific eigenmodes are characterized from the population modes	∗ Problems to properly representing non-convex organs. ∗ The bladder at the planned CT may not be a proper estimation of the mean bladder shape. ∗ Orthogonal eigenmodes may not properly describe the latent structure of the data.

Table 1.4: Methodologies developed for statistical models of organ motion and deformation based on PCA.

and deformation of the CTVs and bladder in rectal and prostate cancer radiotherapy, respectively [55, 56]. In addition, Hu et al. [66] proposed a population-PCA model to describe prostate deformation in magnetic resonance (MR)-tumor-targeted biopsies using a longitudinal database of prostates obtained from MR images and biomechanical models. Similarly, several researchers have introduced so-called 4D population-based or cross-population models for organs undergoing respiratory motion [63, 67, 68]. In

population-based models, modes were derived from the population covariance matrix made by the patients' motion/deformation vectors, i.e., all the rigid and non-rigid organ displacements observed for each patient around his mean bladder were stacked as columns. For a given patient, new organ samples were also generated by a weighted sum of the dominating modes to the mean shape, whereby each weight also obeyed a Gaussian distribution with mean of zero and the corresponding eigenvalue as variance (i.e., the total population variance). However, this may lead to a suboptimal estimation of individual-specific variability as it is considered that the mode variance is shared by all the individuals. In addition, the dominating modes used to generate new organ samples were the most observed directions of geometric variability in the population. As a result, patients with dominating modes different from the population modes may not properly be described. Therefore, as the patients may exhibit heterogeneous organ variability, it is not necessarily verified that all the patients share the same dominant modes as well as the same mode variance.

1.5 Research problem

In prostate cancer radiotherapy the bladder is notorious for presenting the largest inter-fraction shape variations during treatment, caused by continuous changes in volume [26, 31]. These variations in shape introduce geometric uncertainties that render assessment of the actual dose delivered to the bladder during treatment difficult, thereby leading to dose uncertainties that limit the possibility of modeling the dose-volume response for late genitourinary (GU) toxicity [35, 69]. The Quantitative Analysis of Normal Tissue Effects in the Clinic (QUANTEC) project has stated that a similar dose-response to that of late gastrointestinal (GI) toxicity is far from being established. The dosimetric variables obtained from the planning CT are very poor surrogates for the real-delivered dose [33, 34]. As a result, it is crucial to quantify uncertainties produced by inter-fraction bladder variations in order to determine dosimetric factors that affect late GU complications.

The aim of this thesis was thus to characterize and predict uncertainties produced by geometric variations of the bladder between fractions, using solely the planning CT as input information. In clinical practice, a single CT scan is only available for a typical patient at the treatment planning while on-treatment CTs/CBCTs are seldom available during treatment. In this thesis we thereby used a population approach to obtain enough data to obtain the most important directions of bladder motion and deformation using principal components analysis (PCA). As in groundwork, these directions were then used to develop population-based models to predict and quantify bladder geometrical uncertainties. However, we used a longitudinal analysis in order to properly characterize both patient-variance and patient-specific modes from the population. We proposed to use a mixed-effects (ME) model and hierarchical PCA to separate intra- and inter-patient variability to control confounding cohort effects. Other than using PCA, bladder shapes were also represented by using spherical harmonics (SPHARM) which additionally enable data compression without resulting in a loss of information.

We lastly presented PCA models as a simulation tool to quantify dose uncertainties produced by bladder motion and deformation between fractions.

Fig. 1.10 provides a workflow of the methodology used in this thesis. The first step was to learn the most important directions (dominant modes) of bladder motion and deformation from a population database using principal components analysis (PCA). We used these dominant modes to characterize bladder shapes and deformation/motion regions. The second step was an early step of dimensionality reduction using spherical harmonics (SPHARM). This step enabled us to reduce the number of parameters required to represent the bladder surface, further encoded with the dominant modes derived by PCA. The third step was to introduce longitudinal analysis to develop population-based models, instead of using cross-sectional analysis as in previous works. With this, we firstly sought to properly characterize patient-specific variance from the population variance along each mode. We proposed the use of mixed-effects (ME) models to separate intra- and inter-patient variability in order to control confounding; secondly, we sought to properly characterize the patient-specific modes from the population modes by using hierarchical PCA-based models. Table 1.5 provides a list of divergence and convergence points between the developed methodologies to describe organ motion and deformation based on PCA. Finally, we quantified dose and DVH uncertainties produced by bladder motion and deformation between fractions. From on-treatment CT/CBCTs of three patients, we trained individual PCA models using the bladder samples available from the images. Based on the above models, weighted sums of these eigenmodes were used to estimate bladders with their probability of occurrence. We then estimated mean and variance of the dose delivered to the bladder using PCA-based models; subsequently, we compared the estimated accumulated dose with the accumulated dose derived using non-rigid image registration and the on-treatment CT/CBCTs available for the patient.

1.6 Objectives

The main objective of this thesis is to develop a methodology to predict and quantify geometrical uncertainties produced by bladder motion and deformation between dose fractions using planning and on-treatment CT/CBCTs scans of population databases

Also, using only planning information, the specific objectives of the thesis are:

- To characterize and predict bladder motion and deformation between fractions.
- To quantify dose and DVH uncertainties produced by geometric variations of the bladder between fractions.
- To propose a methodology to model OAR motion and deformation between fractions that helps to determine optimal planning dose and treatment modifications by integrating treatment constraint (fraction size and toxicity events), OAR motion and deformation and treatment constraints (PTV: $D_{\min} > 90\%$, $V_{76} > 90\%$; Bladder wall $D_{\max} < 80Gy$, $V_{70} < 50\%$).

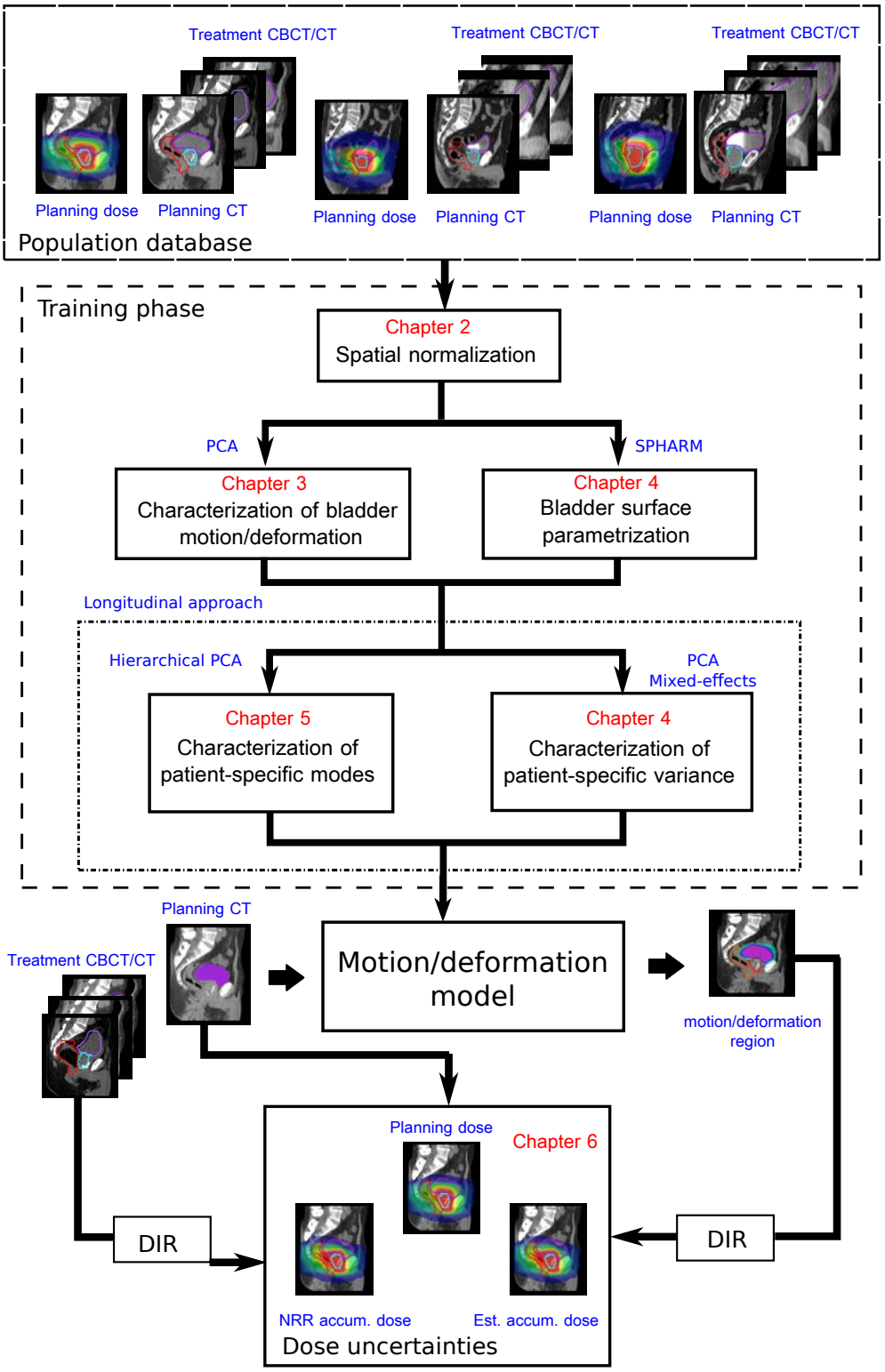

Figure 1.10: Workflow of the methodology used in this thesis.

Shön's methodology [57]	Budiarto's methodology [54]	Rios's methodology [56,62]
Patient-specific data: planning CT + on-treatment CTs/CBCTs	Population data: planning CT + on-treatment CTs/CBCTs	Population data: planning CT + on-treatment CTs/CBCTs
Organ: Rectum/ bladder/ prostate	Organ: CTVs in prostate cancer radiotherapy	Organ: Bladder
Spatial normalization: bony anatomy	Spatial normalization: Prostate barycenter	Spatial normalization: Prostate barycenter
Organ parametrization: 3D triangular mesh model	Organ parametrization: 3D triangular mesh model	Organ parametrization: SPHARM model
	Cross-sectional approach: each observation considered as a single subject	Longitudinal approach: Characterization of patient-specific variance and modes

Table 1.5: List of divergence and convergence points between the developed methodologies to describe organ motion and deformation based on PCA.

1.7 Chapter by chapter overview

This thesis comprises of six chapters. A brief description of each chapter is presented, as follows:

- Chapter 2 presents the clinical context of prostate cancer treated with radiotherapy. It thereby introduces a brief description of the prostate anatomy, statistics related to prostate cancer, and the different options available to treat this cancer. It also presents the main aspects of radiotherapy, and a survey of methods to model organ motion and deformation between fractions.

- Chapter 3 describes the training database used in this study. It also presents the characterization of bladder shapes and motion/deformation regions by means of the limited number of directions of geometric variability called modes, and goes on to describe the validation method performed to assess whether the modes can be used to describe bladder motion and deformation for a typical patient.

- Chapter 4 and 5 describe the longitudinal approach proposed to develop population PCA-based models. Chapter 4 firstly describes the additional database used in this study and the early step of dimensionality reduction used to represent bladder surface with a lesser number of variables. It subsequently addresses the characterization of the patient-specific variance from the population using mixed-effects models. This chapter also describes the validation process used to assess the performance prediction in population-based models. Meanwhile, chapter 5 presents the characterization of the patient-specific variance from the population using hierarchical PCA.

- Chapter 6 presents PCA models as a versatile tool to quantify dose uncertainties produced by bladder motion and deformation. Individual PCA models were trained using the bladder samples available from the on-treatment CT/CBCTs of three patients; and subsequently based on the above models, cumulated doses, local dose variability and dose-volume histogram uncertainties were estimated.

The main contributions of this thesis were:

- A methodology to characterize shapes, and motion/deformation patterns (modes) and regions of the bladder.

- The reduction of the number of variables required to represent bladder surface in a factor of 10 using spherical harmonics (SPHARM).

- A methodology based on longitudinal analysis to develop population-based models that predict motion/deformation regions using solely the planned CT.

- The quantification of dose uncertainties on the bladder produced by motion and deformation between fractions.

Part II

Population-based PCA models using a longitudinal approach to describe bladder geometrical uncertainties

Chapter 2

Data, spatial normalization and organ parametrization

This chapter describes the two population databases used in this study. It also describes the rigid-spatial normalization that was proposed in order to anatomically align the pelvic structures (prostate and bladder). Subsequently, this chapter describes the early step of dimensionality reduction followed to represent all the bladder contours by means of spherical harmonic coefficients (SPHARM). The figures in this chapter, as well those of subsequent chapters, were made by using Matlab R2014, Inkscape, Paraview, and VV image viewer.

2.1 Data

In this study we included two population databases of patients treated for prostate cancer with external beam radiotherapy (RT). These databases were longitudinal data sets, which consisted of repeated observations of the prostate and bladder at different fractions for a patient population. Both databases are named and described below.

2.1.1 Training database

This study included a cohort of 20 patients treated for prostate cancer with external beam radiotherapy with an average age of 70 years. Patients approximately had one additional CT scans per week under identical conditions on a Scanner Philips Big Bore 16. Each patient had a planning CT and several on-treatment CTs (5-8), bringing a total number of 156 images. The resolution of the CT scans were $512 \times 512 \times 80$, with a voxel size of $1mm \times 1\ mm \times 3\ mm$.

Patients were positioned in supine position, arms folded over the chest, pillow under the head and a hold under the knees. Three points had been tattooed on the skin of the patients to allow their positioning under the treatment device. Three fiducial markers were placed on these three points to make them appear in the image before acquiring each CT scans. The contours of the bladder, rectum, prostate and seminal vesicles

(SV) were manually delineated following the same observer (an expert radiotherapy physician). A full bladder protocol was followed, where the patients were asked to hold the volume of his bladder 1 hour before each CT scan and radiotherapy session. None daily-temporal schedule was followed in order to acquire the planning and on-treatment CT scans of the patients. Besides, there were not specific procedures that would have affected the bladder shapes (TURBT/TURP) of the patients.

The prescribed dose was computed in the Philips Pinnacle Treatment Planning System (TPS) Version 9.4. Organ delineation was set to meet GETUG group recommendations [70]. The bladder walls were derived from a $7mm$ negative expansion from the manually delineated contours. Two CTVs were delineated, CTV1 including the prostate and seminal vesicles while CTV2 including only the prostate. PTVs were generated from the CTVs by adding a $1cm$ margin in all the directions, except for the posterior direction, where $5mm$ were added. The total dose was $46Gy$ in PTV1, followed by a boost of $34Gy$ to deliver $80Gy$ in PTV2, at $2Gy$ per fraction. Five 18 MV photon beams were used. GETUG dose-volume constraints were respected throughout: $V70Gy \leq 50\%$ and $Dmax \leq 80\%$ for the bladder wall, and $V50Gy \leq 50\%$, $V72Gy \leq 25\%$, and $Dmax \leq 76Gy$ for the rectum wall.

2.1.2 Validation database

This study included a cohort of 28 patients treated for prostate cancer with external beam radiotherapy with an mean age of 70 years. 25 patients had a planning CT and several on-treatment CTs (6-9) (approximately one CT scans per week were obtained under identical conditions using a Scanner Philips Big Bore 16). Three patients had a planning CT and daily on-treatment CBCTs (35-39). CBCT images were acquired during the 8 weeks of treatment. The total number of bladder contours were 195. The resolution of the CT scans were $512 \times 512 \times 80$, with a voxel size of $1mm \times 1\ mm \times 3\ mm$.

Patients were positioned in supine position, arms folded over the chest, pillow under the head and a hold under the knees. Three points had been tattooed on the skin of the patients to allow their positioning under the treatment device. Three fiducial markers were placed on these three points to make them appear in the image before acquiring each CT scans. The contours of the bladder, rectum, prostate and seminal vesicles (SV) were manually delineated following the same observer (an expert radiotherapy physician). A full bladder protocol was followed, where the patients were asked to hold the volume of his bladder 1 hour before each CT scan and radiotherapy session. None daily-temporal schedule was followed in order to acquire the planning and on-treatment CT scans of the patients. Besides, there were not specific procedures that would have affected the bladder shapes (TURBT/TURP) of the patients.

The prescribed dose was computed in the Philips Pinnacle Treatment Planning System (TPS) Version 9.4. Organ delineation was set to meet GETUG group recommendations [70]. The bladder walls were derived from a $7mm$ negative expansion from the manually delineated contours. Two CTVs were delineated, CTV1 including the prostate and seminal vesicles while CTV2 including only the prostate. PTVs were generated from the CTVs by adding a $1cm$ margin in all the directions, except for the

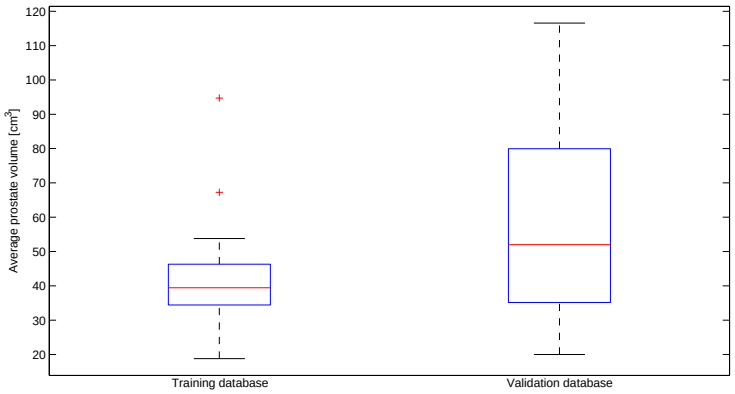

(a) prostate

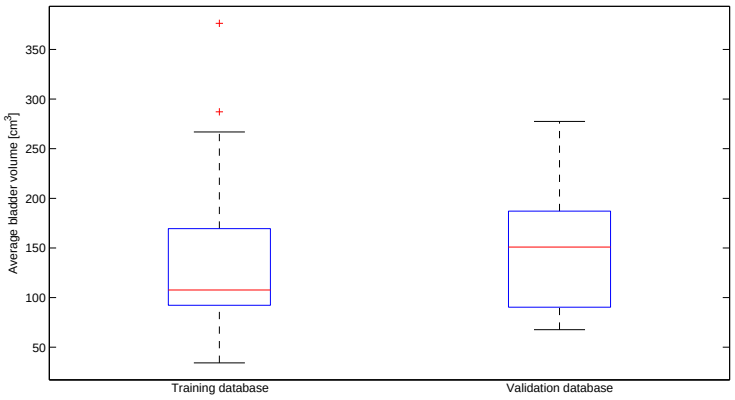

(b) bladder

Figure 2.1: Average values for the bladder and prostate volume in both databases.

posterior direction, where $5mm$ were added. The total dose was $46Gy$ in PTV1, followed by a boost of $34Gy$ to deliver $80Gy$ in PTV2, at $2Gy$ per fraction. Five 18 MV photon beams were used. GETUG dose-volume constraints were respected throughout: $V70Gy \leq 50\%$ and $Dmax \leq 80\%$ for the bladder wall, and $V50Gy \leq 50\%$, $V72Gy \leq 25\%$, and $Dmax \leq 76Gy$ for the rectum wall.

2.1.3 Descriptive information

Table 2.1 provides the population avarage of some parameters that describe the bladder and prostate contours in both databases. Besides, Fig. 2.1 shows the distribution of the average volume of the bladder and prostate during treatment in both databases.

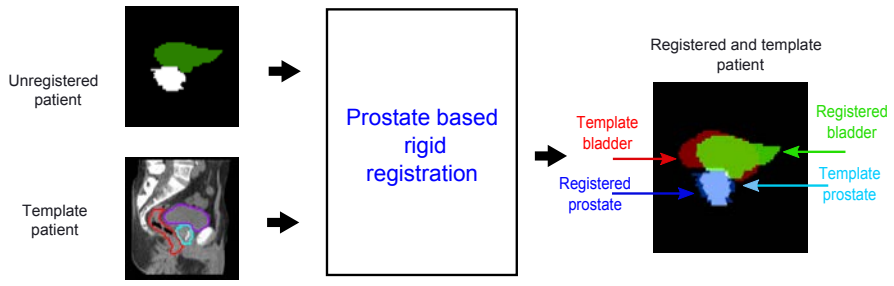

Figure 2.2: Overlay of a typical individual bladder registered to the template.

Table 2.1: Population average of parameters describing bladder and prostate volumes in both databases.

	Training database		Validation database	
	Prostate	Bladder	Prostate	Bladder
Mean volume $[cm^3]$	42.65	145.48	57.40	136.10
std volume $[cm^3]$	17.43	102.18	25.17	80.1
Max. volume $[cm^3]$	113.47	645.24	121.30	531.70
Min. volume $[cm^3]$	12.46	25.20	17.85	30.17

2.2 Prostate-based rigid registration

This was served to spatially align all the bladders in the same spatial referential. After defining the prostate barycenter of a patient as common coordinate system, henceforth called the template, all the patient structures were thus registered by semi-automatically aligning the prostate barycenters, which provided a transformation T. The template was a patient from the training database whose prostate exhibited the lowest volume variation and the most similar mean volume to the population mean. The individual bladders were then propagated to the common template using the obtained T. This transformation was derived from the difference in physical positions between the two barycentres of the prostates. Non rotation or affine transformation were made as the bladder does not present rotations as the prostate does, neither volume changes in the prostate are correlated with volume changes in the bladder. This spatial normalization thus enabled bladder motion and deformations to be quantified with respect to the template prostate barycenter. Fig. 2.2 depicts an example of the performed rigid registration/propagation step.

In addition, all the binary images representing the bladder contours were cropped to the resolution of $135 \times 215 \times 55$ voxels as each delineated bladder in the database only occupied a region in the whole image. This dimension was chosen seeking the minimum image size that covered all the bladder contours in the database. The binary images were thus cropped as follows: firstly, the binary image representing the bladder contour at the planning CT of the template patient was defined as the reference image; secondly, we manually cropped the reference image to the resolution of $135 \times 215 \times 55$ by using

the VV image viewer; thirdly, the binary images representing the bladder contours were semi-automatically cropped based on cropped reference image.

2.3 Bladder shape parametrization

An essential objective in shape modeling has been the reduction of parameters needed to describe a shape instance. As a first step towards this goal, PDM method was proposed to parameterize 3D shapes by means of a set of boundary points [58, 71]. However, this approach required thousands of points to properly describe shape surfaces and a one-to-one correspondence between these boundary points [46,54,55,57,71]. SPHARM, the extension of 2D Fourier techniques to three dimensions, was proposed to obtain smooth, accurate and fine parametrization of 3D shapes with spherical topology with a fewer number of parameters [72–75]. This method consisted in expressing a surface as a linear combinations of a reduced number of spherical harmonics basis functions, where different levels of approximation errors can be obtained by truncating the spherical harmonic series.

As opposed to other methods like PDM, it offers the advantage of delivering a shape parametrization with an implicit correspondence between shapes on the boundary. Besides, the spherical harmonics define an orthogonal basis functions whose spanned space has a reduced dimension that enables us to describe and quantify shape variations. This implies that the number of parameters (i.e. SPHARM coefficients) needed to describe a shape instance is lower than other shape modeling methods like PDM.

In medical imaging, SPHARM has played a crucial role in 3D-shape representation and modeling of anatomic structures in several applications, including computer assisted diagnosis [76–80], rigid registration [79,81] and organ segmentation [73–75,82,83], among others. In most of these applications, statistical shape models were developed by applying PCA to a training population of organ surfaces parameterized with SPHARM coefficients, where eigenmodes of maximum variation around the mean shape were calculated. In these applications, the surfaces of these binary organs were initially parameterized by surface boundary points, and these boundary points-based parametrization were subsequently expanded into series of spherical harmonics.

In our study, SPHARM was used to parameterize the surface of each delineated bladder into a vector of SPHARM coordinates. As a result, we initially defined a reference point for each bladder contour, which was its distance map point. An uniform 3D sphere contour with 64442 evenly distributed vertices was then created and centered on the defined reference point, using a sampling of 1 degree for each spherical angle. The sampling was an arbitrary number aiming to obtain a re-sampling lines in radial directions that were dense enough to fully capture the feature points of bladder surface. Following mesh parameterization, each bladder was represented by a sphere surface function $f = (x(\theta, \phi), y(\theta, \phi), z(\theta, \phi)) \in \mathcal{R}^3$, and we subsequently encoded this function f in a reduced number of spherical harmonic functions, as follows:

$$f(\theta,\phi) = \sum_{l=0}^{\infty}\sum_{m=-l}^{l} c_l^m Y_l^m(\theta,\phi) \approx \sum_{l=0}^{L}\sum_{m=-l}^{l} c_l^m Y_l^m(\theta,\phi), \qquad 0 < L < \infty \tag{2.1}$$

where θ and ϕ denoted the spherical coordinates, and with

$$Y_l^m(\theta,\phi) = (-1)^m \sqrt{\frac{2l+1}{4\pi}} \sqrt{\frac{(l-m)!}{(l+m)!}}\, P_l^m\left(\cos(\theta)\right) e^{im\phi} \tag{2.2}$$

defining a spherical harmonic function of degree l and order m, where P_l^m was an associated Legendre polynomial; L was the number of spherical harmonic functions used to approximate f; and coefficients c_l^m corresponded to the coordinates in the space spanned by the spherical harmonic basis. The c_l^m coefficients were obtained as the projection of the mesh function f onto the spherical harmonic basis, i.e, $c_l^m =< f(\theta,\phi), Y_l^m(\theta,\phi) >$. By fixing a harmonic degree to L, the bladder surface at the j-th CT scan of the i-th patient, denoted by $x_{i,j} \in \mathbb{R}^{d_1 \times d_2 \times d_3}$, was uniquely represented in spherical harmonic coordinates as follows:

$$c_{ij} = \begin{bmatrix} c_{ij,0}^0 & c_{ij,1}^0 & c_{ij,1}^1 & c_{ij,2}^0 & \cdots & c_{ij,L}^L & c_{ij,1}^{-1} & c_{ij,2}^{-1} & \cdots & c_{ij,L}^{-L} \end{bmatrix}^T \tag{2.3}$$

where

$$c_{ij} \in \mathbb{R}^p \quad \wedge \quad p = 2\left[(L+1)^2 - \frac{(L+1)^2 - (L+1)}{2}\right] << d = d_1 \times d_2 \times d_3 \tag{2.4}$$

Observe that we have taken only the SPHARM coefficients that were different to 0. The value of L was optimally chosen by analyzing its impact on the approximation error in the training cohort. The approximation error was assessed as a function of L in terms of dice score (DS) and the Hausdorff distance (HD).

In the study, an L of 15 spherical harmonics was selected to approximate bladder surfaces in the population database. With $L = 15$ in Eq. 2.1, the average DS and HD values in the training database were 0.954 ± 0.0522 and $6.112 \pm 4.997\,mm$, respectively. Conversely, validation database equivalents were 0.97 ± 0.0099 and $4.32 \pm 2.27\,mm$, respectively. Any bladder in the databases can thus be represented by $p = 272$ coefficients instead of $d = 1596375$ voxel variables. The SPHARM surface parameterization was implemented in C+/C using ITK libraries.

2.4 Discussion

We have hereby described the population databases used in this study. We have also proposed a prostate-based rigid registration process to map all the bladders in the same

spatial referential. After defining the prostate barycenter of the template patient as common coordinate system, all the patient structures were thus registered by semi-automatically aligning the prostate barycenters. This rigid-registration was derived from the difference in physical positions between the two barycentres of the prostates. We have also proposed to parameterize the bladder surface using spherical harmonic expansion. A number of 15 spherical harmonic basis functions were used, since acceptable reconstruction errors were obtained in the population databases in terms of DS and HD.

In this study we have used two databases that consisted of repeated observations of the bladder at different fractions for a patient population. Each patient in the data set had more than one observation at different time-points. As a result, the analysis of such data sets should lead to the characterization of the most common geometric variations of the bladder that patients shared between them (i.e. inter-patient variability), and also those geometric variations that make them different (i.e. intra-patient variability). We therefore followed a longitudinal analysis instead a cross-sectional in order to take into account the inherent correlation of repeated measurements of the same patient. As opposed to previous works, our aim was then to separate intra- and inter-patient variability in order to tailor organ motion and deformation models to a typical patient using population databases. It is important to highlight that we consider that our databases were representative of the population due to the prostate and bladder volume distributions were similar to the volume distributions of previous studies [26, 32]. For example, in the study of [26], the population volume of the prostate and bladder were $55.46 \pm 21.16cm^3$ and $187.21 \pm 71.05cm^3$, respectively. Meanwhile, in the study of [32], the population bladder volume was approximately $151.63 \pm 95.07cm^3$, and the maximum and minimum volume were $686cm^3$ and $46cm^3$, respectively. In our study, the bladder volume was $145.48 \pm 102.18cm^3$ and $136.10 \pm 80.10cm^3$ in the training and validation databases, respectively. Meanwhile, the maximum and minimum volume were $645.24cm^3$ and $25.2cm^3$ in the training database, and $531.70cm^3$ and $30.17cm^3$ in the validation database.

Previous studies have matched CT scans for modeling geometric variations of the pelvic organs based on body anatomy, soft-tissue registration, or fiducial markers. For example, Söhn et al. [57] used bone anatomy to match for each patient the repeat CT scans to the planning CT in order to obtain an intra-patient model for the prostate/bladder/rectum. Thörnqvist et al. [51] used fiducial markers to model individual geometric variations of the prostate. In contrast, Hu et al. [66] proposed anatomical apex and base points of the prostate. Meanwhile, Budiarto et al. [54] defined the prostate barycenter as the origin for each CT scan in order to derive a population-based model of the CTV for prostate cancer. However, we believe that using the barycenter as a reference point is not feasible for all pelvic organs to obtain population-based models. For this reason, Bondar et al. [55] used a setup based on bone anatomy for each patient, to calculate intra-patient motion-deformation vectors and develop a population model of CTVs for rectum cancer, as did [54]. Nevertheless, this method may not be the most suitable setup for analyzing in the same framework all the different sizes and shapes that an organ can manifest in patients [56]. In our study, we did not use bone anatomy

as it can significantly differ from one patient to another, affecting the rigid registration and distribution of the pelvic organs. On the other hand, the bladder is attached to the prostate across the urethra, and the surface in contact with the prostate is generally stable, or is at least considered the least mobile part, while the top and anterior part can expand. We thereby sought to align this fixed bladder section in order to model both bladder motion and deformation. We believe that the ideal setup could be to match CTs using the boundary between the bladder and prostate, yet that type of rigid-registration is not possible. For intra-patient analysis, we think that the prostate barycenter offers a better means to perform this alignment due to the prostate volume being near constant during treatment, despite its rigid displacements [26, 30] (see Fig. 1 in appendix A).

For inter-patient analysis, we consider that differences in prostate size and shape in the population can be reduced by defining the template as a patient presenting a prostate with the lowest volume variation and the most similar mean volume to the population mean (see Fig. 6.5 in appendix A). In our training database, this patient prostate volume was $42.14 \pm 3.33cm^3$, whereas the population volume was $42.65 \pm 17.43cm^3$. For example, Fig. A.1b shows 3D sagittal views of some segmented patient prostates that were plotted as outside the first and third quartiles of the boxplot of the average prostate volumes. In Fig. A.1a, it can be observed that the size and shape differences were not significant for patients 17, 7, and 20, particularly in the upper anterior part of the prostate (the surface in contact with the bladder). The highest dissimilarity was obtained for Patient 8, an outlier like Patient 17. We thus consider that size and shape differences among prostates in the population are not sufficiently greater than those observed in bladders to introduce disturbances, at least in the first eigenmodes. For example, it can be observed in Fig. 3.3 that the first three modes did not reveal geometric variations in the lower posterior bladder section, i.e., the region that presented the geometric variations in the bladder produced by the barycenter alignment (see Figs. 4.5, 6.5 and A.1). Also, Fig. 6.5 demostrates that for intra-patient analysis, the first mode was also dominated by the bladder volume, meaning that volume changes in the prostate do not affect at least the most important mode in the bladder. It is worth mentioning that we did not introduce any rotation, nor conduct affine transformation, as the bladder does not present rotations as the prostate does, nor do volume changes in the prostate correlate with volume changes in the bladder. Besides, if all the bladders in the population are transformed using affine or non-rigid registration, inter-patient geometric variability can disappear, which is the main advantage of using ME models, where individual effects are separated from the mean. We therefore considered that the prostate barycenter also provided a suitable reference point in the pelvic zone to model bladder motion and deformation for inter-patient analysis, despite the potential variations of prostate in size and shape across the population.

Similar to other SPHARM-based shape models, our study was significantly aided by encoding the information of the bladder shape into vectors of SPHARM coefficients with orders of 10^2, instead of vectors of boundary points with orders of 10^3 obtained from a meshing process, as used in [54, 57]. The SPHARM parameterization thus enabled us to reduce not only computation time but also numerical errors, by affording finite

arithmetic operations, and data storage while preserving shape information. However, it is important to highlight that not all the bladder shapes were properly parameterized using the radial sampling in spherical coordinates. In our training database, some bladders with non-convex dilations in the inferior-ventral region resulted in higher reconstruction errors. Future work should thus be dedicated to improve bladder-shape modeling. One way would be to extend the SPHARM methodology to model a much larger class of simply-connected closed shapes using an area-preserving, distortion minimizing spherical mapping, as expressed in [73, 80]. Alternatively, a second possibility is to use a different computational technique called isogeometric analysis, which generalizes and improves on the standard finite element method [84, 85]. In population data, this technique offers the advantage of obtaining a surface parameterization with corresponding points in all organ instances without requiring a mesh relaxation procedure. This methodology defines a transformation to a canonical domain, where parametrization is carried out and extrapolated to any organ instance.

2.5 Conclusion

We have described the population databases used in this study in order to propose a methodology to predict and quantify geometrical uncertainties produced by bladder motion and deformation between fractions. We have also proposed a prostate-based rigid registration that enable us to align all the bladders in the same spatial referential. Besides, we have proposed an early step of dimensionality reduction using SPHARM in order to reduce the number of variables required to represent the bladder contours in a factor of 10.

Chapter 3

Characterization and dimensionality reduction of bladder motion and deformation in prostate cancer radiotherapy

This chapter is dedicated to characterize shapes and motion/deformation regions of the bladder using PCA for patients treated for prostate cancer with radiotherapy. This study included the cohort of 20 patients, where for each patient a planning CT scan and several (ranging from 5 to 8) on-treatment CT scans were available. As in Budiarto et al (2011), we obtained a limited number of directions of geometric variability that enabled us to characterize bladder shapes and motion/deformation regions, but using a voxel representation rather than a set of corresponding surface points. These directions of geometric variability called modes were then used to characterize bladder shapes and motion/deformation regions in the latent space. These modes were validated using a reconstruction error and leave-one-cross validation on the training database. A dimensionality reduction was obtained by representing any bladder in term of 104 scores instead of 1596375 voxel variables. 28 modes were considered as population directions to model bladder geometric variations.

The methodology proposed in this chapter was accepted for publication in the International Journal of Innovation and Research in BioMedical engineering (IRBM) [56]. The chapter is organized as follows. Section 3.1 describes the database used in this study, and it provides a description of the proposed model together with the validation framework. Section 3.2 presents the results while section 3.3 provides a discussion of the experimental findings. Lastly, section 3.4 summarizes the main conclusions.

3.1 Data

We used the training database previously described in Chapter 2.

3.2 Methods

Our proposed model is based on the assumptions stated in the methodology developed by Budiarto et al. [54]: firstly, that the bladder moves and deforms in a limited number of directions, constrained by the body's anatomy; secondly, that the inter-fraction geometric organ variations are randomly distributed along the set of variability directions; thirdly, that despite the potential variations in organ size and shape across the population, principal directions of geometric variation prove to be similar in all patients; fourthly, that geometric variations between fractions are independent random variables, where the time sequence of the observations does not matter. Hence, each bladder within the population can be characterized by its variation along each direction.

The paper is organized as follows. Section 1 describes the two databases (training and testing) included in this study. Section 2 provides a detailed description of the proposed method together with the validation framework. Section 3 presents the results and comparison to groundwork methods. Lastly, Section 4 discusses the experimental findings, with a conclusion given in Section 5 in addition to final considerations and future perspectives.

Fig. 3.1 shows the steps followed to train the population-based PCA model. Firstly, rigid-spatial normalization was performed in order to align all the bladders in the same spatial referential; secondly, a step of dimensionality reduction was conducted using PCA, thereby yielding a limited set of directions of maximum geometric variability. These directions, or modes, were validated by leave-one-out cross validation, seeking to assess whether patients exhibited common directions of bladder motion and deformation.

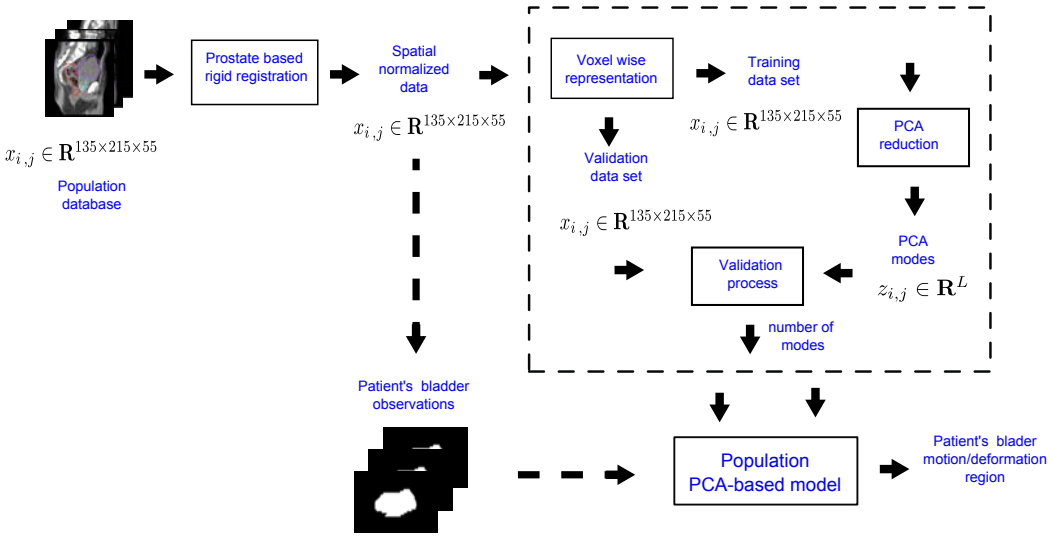

Figure 3.1: Workflow of the method used to train the population-based model. 0) Prostate-based registration, 1) principal component analysis (PCA) reduction, 2) leave-one-out cross-validation.

3.2.1 Principal component analysis

PCA is a powerful tool used for dimensionality reduction of high-dimensional data while preserving the most important information. In this study the modes of bladder motion and deformation were obtained using PCA, where each bladder instance was considered as an observation and each voxel as a variable.

Let $x \in \mathbb{R}^d$ be an anatomical structure after stacking the image into a vector, where d denoted the number of voxels. The aim was then to approximate x as a weighted combination of a limited number of the modes ψ_i, as follows:

$$x \approx \hat{x} = \sum_{i=1}^{q} z_i \, \psi_i, \tag{3.1}$$

where $z_i = x^T \psi_i$ was the projection of x along the mode ψ_i, which may be interpreted like a "measure" of geometric variability. Modes ψ_i were obtained by applying SVD to a data matrix denoted as $\mathcal{X}$ whose columns were the bladders stacked as vectors (see Eq. 3.2). The objective was to have a sample that described all the possible bladder shapes and sizes, i.e a snapshot matrix of the "bladder space". Denoting the observed bladder of the i-th patient at the j-th CT scan as x_{ij}, the data matrix and its SVD were defined as follows:

$$\mathcal{X} = \begin{bmatrix} x_{11} & \cdots & x_{1j_1} & x_{21} & \cdots & x_{2j_n} & \cdots & x_{nj_n} \end{bmatrix} = \mathbf{U}\mathbf{\Sigma}\mathbf{V}^T \tag{3.2}$$

where j_i was the number of images available for the i-th patient and n was the number of patients. $\mathbf{\Sigma}$ was the singular value matrix, and $\mathbf{U}$ and $\mathbf{V}$ were the left and right singular vectors, respectively. Each right singular vector defined a mode. Meanwhile, the singular values defined an significance ranking for the data variability described by each mode, attesting $var(\psi_1) = \sigma_1^2 \geq var(\psi_2) = \sigma_2^2 \geq \cdots \geq var(\psi_r) = \sigma_r^2$, where r was the rank of the data matrix $\mathcal{X}$ (given by the number of available images). The variance of the original variables was thus dominated by the first q modes. The accumulated variability contained in the first q modes was determined as follows:

$$P_q = \frac{\sum_{i=1}^{q} \sigma_i}{\sum_{i=1}^{r} \sigma_i}, \qquad q = 1, \ldots, r \tag{3.3}$$

The dimensionality reduction was thereby obtained by projecting each anatomical structure x on the subspace spanned by the first q modes, called "latent space"; then each structure x was represented by the scores $z_1, \ldots, z_q$ with $q < r << d$.

3.2.2 Validation

In order to test whether the modes described common directions of bladder motion and deformation among all patients, we performed a leave-one out cross validation on the training database. The modes were evaluated by using a reconstruction error metric in both data sets. Given a bladder x and its approximation $\hat{x}$ in Eq. 3.1, the reconstruction error e was defined as follows:

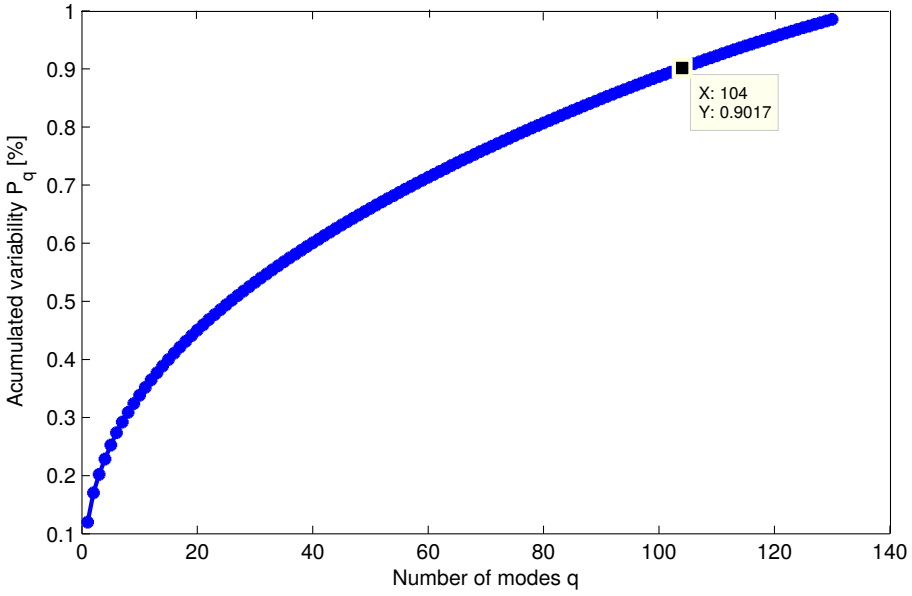

Figure 3.2: Accumulated mode variance P_q obtained by PCA. 90% of accumulated variability was obtained with the first 103 modes.

$$e = \frac{2\sum v_j \hat{v}_j}{\sum v_j + \hat{v}_j}, \tag{3.4}$$

where v_j and $\hat{v}_j$ were the intensity at the j-th voxel of the image x and its approximation $\hat{x}$, respectively. If the reconstruction of x was exact, then e was equal to 1; otherwise, the value of e was between 0 and 1. The mean of the reconstruction error e in all the bladders was also calculated, i.e., $\mathcal{M} = (1/N) \cdot \sum_{i=1}^{N} e_i$, where e_i denoted the approximation error of the i-th image x_i and N the number of available images, either in the training or validation data set.

3.3 Results

The analysis was carried out in MATLAB (R2014a). The eigenvectors and were obtained using the function eigs. Fig. 3.2 shows the spectrum of the singular values of all 20 combinations of cutting the training database from the leave-one-out cross validation. The size of the data matrix $\mathcal{X}$ was $1596375 \times n$, where $d = 135 \times 215 \times 55 = 1596375$ voxels and n varied between 151 and 154 (i.e. the available images after removing the left-out patient's images). The first mode contributed the largest variance (11.4% of the variability); similarly, the second and third modes contributed, on average, 5.05% and 3.18%, respectively. Fig. 3.2 shows also that 90% of the accumulated variability

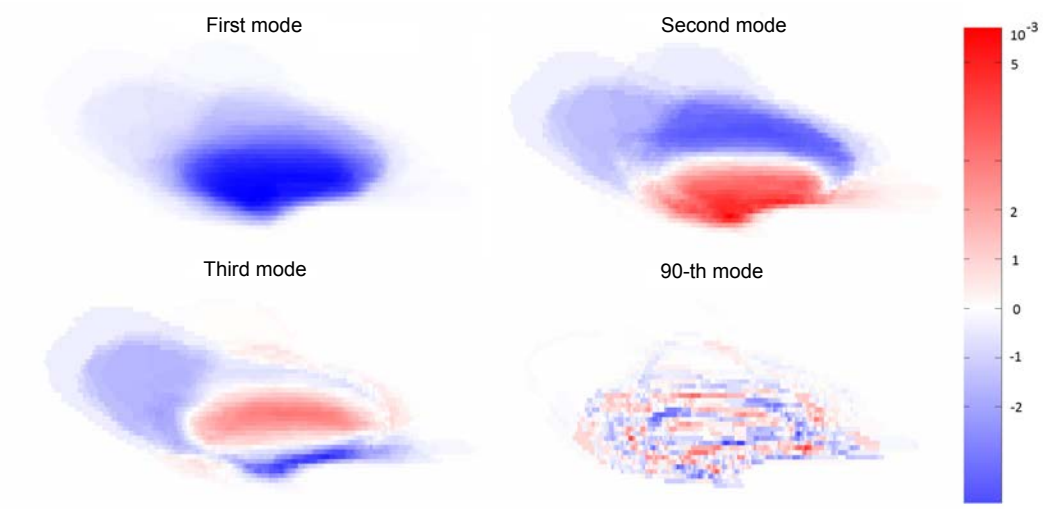

Figure 3.3: Sagittal view of the first three and 90-th mode. Each voxel of a given mode has a normalized value that represents its contribution in that direction of geometric variability.

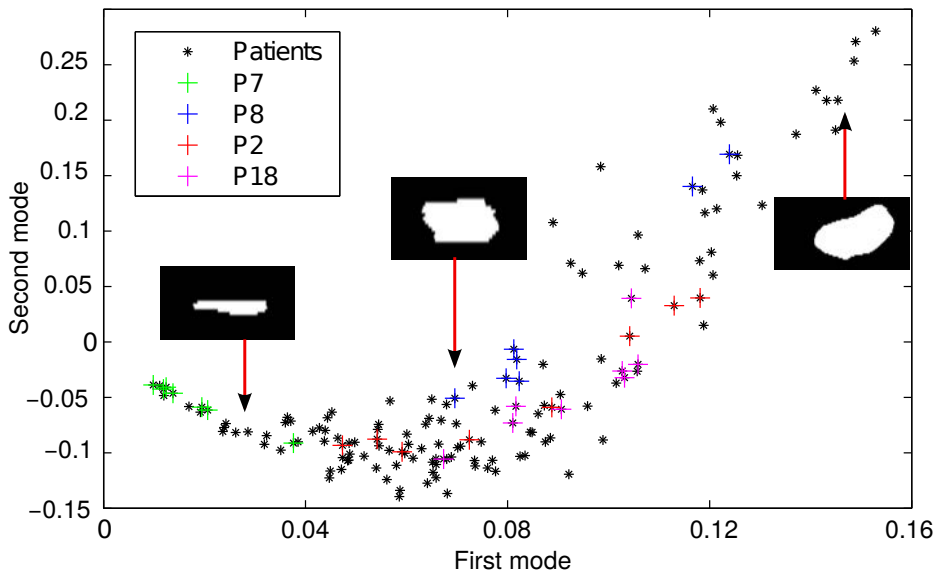

Figure 3.4: Scatterplot of the patients projected in the space spanned by the first two modes (Black points). Non-black points correspond to the observations for some patients in the database.

was contributed approximately by the first 103 modes. Any bladder was therefore represented as a vector of $q = 103$ scores ($q = 103 << r << d = 1596375$). The

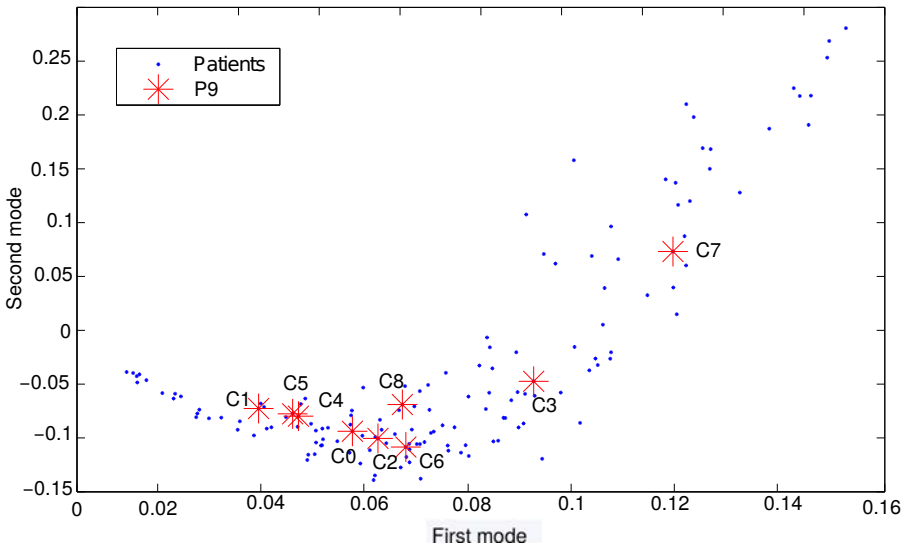

Figure 3.5: Scatterplot of the observations available for one patient projected in the space spanned by the first two modes. The symbol C_i denotes the observed bladder in the *i-th* CT scan.

analysis was carried out in MATLAB (R2014a). The eigenvectors and were obtained using the function eigs.

Fig. 3.3 presents sagittal views of the first three and 90-th modes. Each voxel of a given mode has a normalized value that represents its contribution in that direction of geometric variability. The first mode, the static component of the database, then represents the non-zero voxels that are the most significant to reconstruct any bladder, i.e. it is associated with the bladder volume. Similarly, modes with higher indices, like the second and third, represent those voxels that dilate and shrink regions in the bladder according to its negative and positive values. For example, if the weight z happens to be increased in Eq. (3.1), the second mode will shrink the superior-region of the bladder. However, higher modes, like the 20-th, do not describe directions of geometric variability observed in patients rather than patient-specific directions (see Fig. 3.6).

Fig. 3.4 depicts the projection of all the bladders on the space generated by the first two modes. Each point can be interpreted like measure of geometric variation along each direction. As observed in Fig. 3.4, this reduced space provides some well-defined regions or clusters of bladder shapes. Flat bladders, for example, are mainly found in the square region $(0, 0.5) \times (-1.5, 0.5)$. It is also observed that each patient has a motion/deformation region. Fig. 3.5 shows the observations of a patient during treatment, demonstrating that bladder geometric variations between fractions follow a random trajectory.

Fig. 3.6 shows that both mean and standard deviation of the approximation error $\mathcal{M}$ decreased as the number of modes was increased in both the PCA model and left-

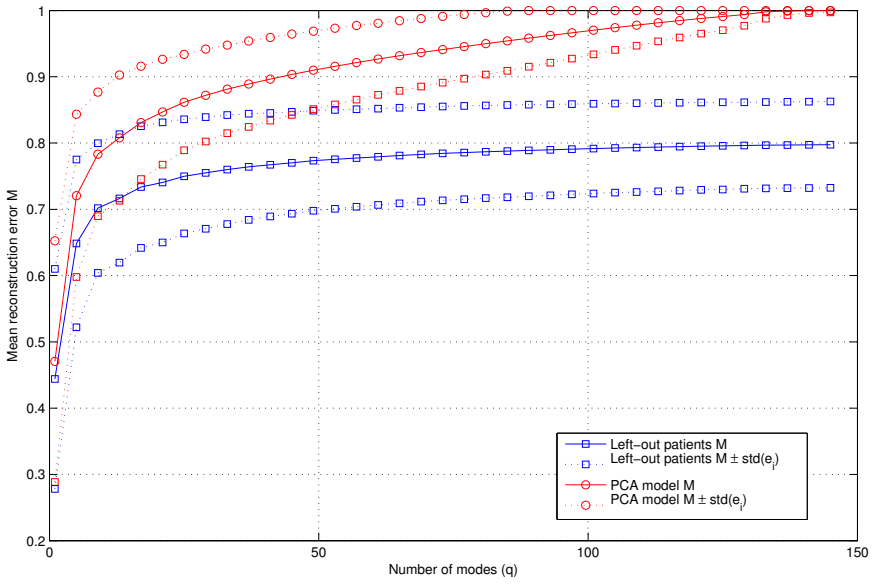

Figure 3.6: Mean approximation error $\mathcal{M}$ as a function of the number of modes in the PCA model and left-out patients. There are bands (dotted-lines) that represent the mean approximation error $\mathcal{M}$ (solid-lines) plus and minus one standard deviation of e_i.

out patients. However, mean and standard deviation of the reconstruction error $\mathcal{M}$ did not reach the value of zero in the left-out patients, mean reconstruction error settles between 0.75 and 0.80 after the 25-th mode.

3.4 Discussion

We have hereby implemented a methodology to describe and quantify uncertainties produced by inter-fraction geometric variations of the bladder in prostate cancer radiotherapy via population analysis. We performed leave-one-out cross validation in order to assess whether the modes described common directions of bladder motion and deformation for a typical patient. A reconstruction errors metric was proposed to assess the modes in both data sets in order to test whether they described common directions of bladder motion and deformation for a typical patient. Bladder shapes and motion/deformation regions were then characterized in the latent space spanned by the first two modes.

As opposed to previous studies, we proposed a population PCA-based model using a voxel representation rather than surface points [54,57]. We consider that the meshing approach has the disadvantage of requiring a relaxation process to ensure an one-to-one correspondence among surface points before applying PCA. Meanwhile, our voxel representation has the disadvantage of requiring a higher number of modes to sufficiently

describe the data variability. For example, 15 modes were required to describe 90% of CTV motion and deformation for prostate cancer in [54] whereas 104 modes were sufficient in our study to describe the same percentage of data variability. We consider that this result can be a consequence of the higher number of parameters being used to describe the bladder surface, which increases the information to be analyzed. Nevertheless, future studies should be done to confirm or disapprove the number of modes required to properly describe bladder motion and deformation due to the studied organs were not the same.

As established in the model assumptions, the modes represent directions of geometric variability. Unlike the first mode, they do not clearly define affine transformations that can be initially corrected using rotations along a certain axis or using a uniform dilation. Each mode dilates and shrinks regions in the bladder, showing that bladder motion and deformation are not uniform. In addition, we show that it is possible to characterize bladder shapes and patient's motion/deformation region in the latent space, which is an infeasible task in the original space due to its high dimensionality and the intra- and inter-patient variability. It is also proved that bladder motion and deformation between fractions follow a random behavior.

As in Budiarto et al. [54], the mean error decreased as the number of modes increased in both data sets. However, we found that the mean error settled in 0.8 in the left-out patients, implying that some individual directions were not detected by the modes. Besides, it can be observed We consider that the first 28 modes can thus be considered as truly population directions with a mean reconstruction error of 88% and 80% in the training and validation data, respectively. Nevertheless, comparing Figs. 3.2 and 3.6, a trade-off between truly population modes and accumulated data variability can be done to define the suitable order of a population-based PCA model, where we considered that 60 modes were needed in our study.

3.5 Conclusion

We implemented a model to characterize shape and motion/deformation regions of the bladder in prostate cancer radiotherapy via population analysis. This model was implemented following a voxel representation. This model can be used to quantify uncertainties produced by inter-fraction geometric variations of the bladder in dose delivering. Future studies should now be conducted to develop a model that predicts deformation/motion regions for a typical patient using solely the planned CT scan as input information. Future studies should also be focused to study the relationship among bladder motion and deformation, delivered dose and urinary symptoms in prostate cancer radiotherapy.

Chapter 4

Population PCA-based models using a longitudinal approach: characterization of patient-specific variance from the population variance

This chapter presents the longitudinal approach proposed to properly characterize patient's variance from the total population variance. This study included two population databases of patients treated for prostate cancer with external beam radiotherapy (RT). We trained the model using data from the database of 20 patients, including a planning CT and several on-treatment CTs (5-8) for each patient. We also used the validation database of 28 patients described as follows: 25 patients had a planning CT as well as 6-9 on-treatment CTs, and 3 patients with a planning CT as well as 35-39 on-treatment CBCTs for each. In this chapter, we used mixed-effects (ME) models to separate intra- and inter-patient variability along each mode in order to control confounding effects. This step enabled us to reduce the number of parameters required to represent the bladder surface, further encoded with the dominant modes derived by PCA. This step also allowed us to reduce data storage and the processing time, among others aspects. We evaluated the model by means of leave-one-out cross validation on the training data and also the validation data. Probability maps (PMs) were thus generated as predicted regions of probable bladder motion and deformation. These PMs were compared with the observed region using a metric based on mutual information distances. The prediction was compared with two previous population PCA-based models.

Our main contribution regarding groundwork was to introduce ME models in order to estimate individual-specific variations between fractions from a reduced-order model (SPHARM/PCA based model). Using the ME model the following aspects were addressed for each mode: i) the estimation and separation of individual-specific variance from that of the population, i.e, the inherent correlation of intra-individual observations;

ii) the reduction of the observed population variance by grouping repeated observations per patient by means of a "patient factor"; iii) the characterization of the individual-specific directions of motion and deformation from the population; iv) the study of longitudinal observations ordered in time, which may reflect temporal trajectories in the latent space. This study is also the first one in explicitly addressing the issue of predicting a region of probable inter-fraction bladder motion/deformation using solely the planning CT. A quantitative comparison of predicted vs observed probability maps was proposed using our model and other previous motion/deformation models.

The methodology proposed in this chapter was published in the International Journal of Medical Image Analysis (MedIA) [62]. The chapter is organized as follows. Section 4.1 describes the two databases (training and testing) included in this study. Section 4.2 provides a detailed description of the proposed method together with the validation framework. Section 4.3 presents the results and comparison to groundwork methods. Lastly, section 4.4 discusses the experimental findings, with a conclusion in section 4.5 in addition to final considerations and future work.

4.1 Data

We included the training and validation databases previously described in Chapters 2. Population-based models were thus trained using the training database. Meanwhile, the prediction performance of the model was evaluated by following leave-one-out cross validation in the training database and also using the validation database.

4.2 Methods

The training steps are depicted in Fig. 4.1. Firstly, all the bladders were aligned in the same spatial referential by performing the same prostate-based rigid registration used in Chapter 3; secondly, bladder surface parameterization was conducted using SPHARM, followed by dimensionality reduction using PCA, thereby yielding a limited set of directions of maximum geometric variability. These directions, or modes, were validated by leave-one-out cross validation, aiming to determine whether patients exhibited common directions of bladder motion and deformation; finally, a mixed-effects model was fit to each direction to model the inter and intra-individual geometric variations obtained.

4.2.1 Principal component analysis

This step was aimed to represent, in a reduced space, all possible rigid and non-rigid bladder displacements. After obtaining SPHARM coefficients, an empirical covariance matrix $\mathbf{C}$ of local patient motion-deformation vectors was thus defined in order to calculate the directions of maximum variability by using matrix diagonalization. Here, a local patient motion-deformation vector defined the difference between the observed bladder and patient mean bladder. Thus, denoting the observed bladder of the i-th patient at the j-th CT as c_{ij}, the empirical covariance matrix $\mathbf{C}$ was defined as follows:

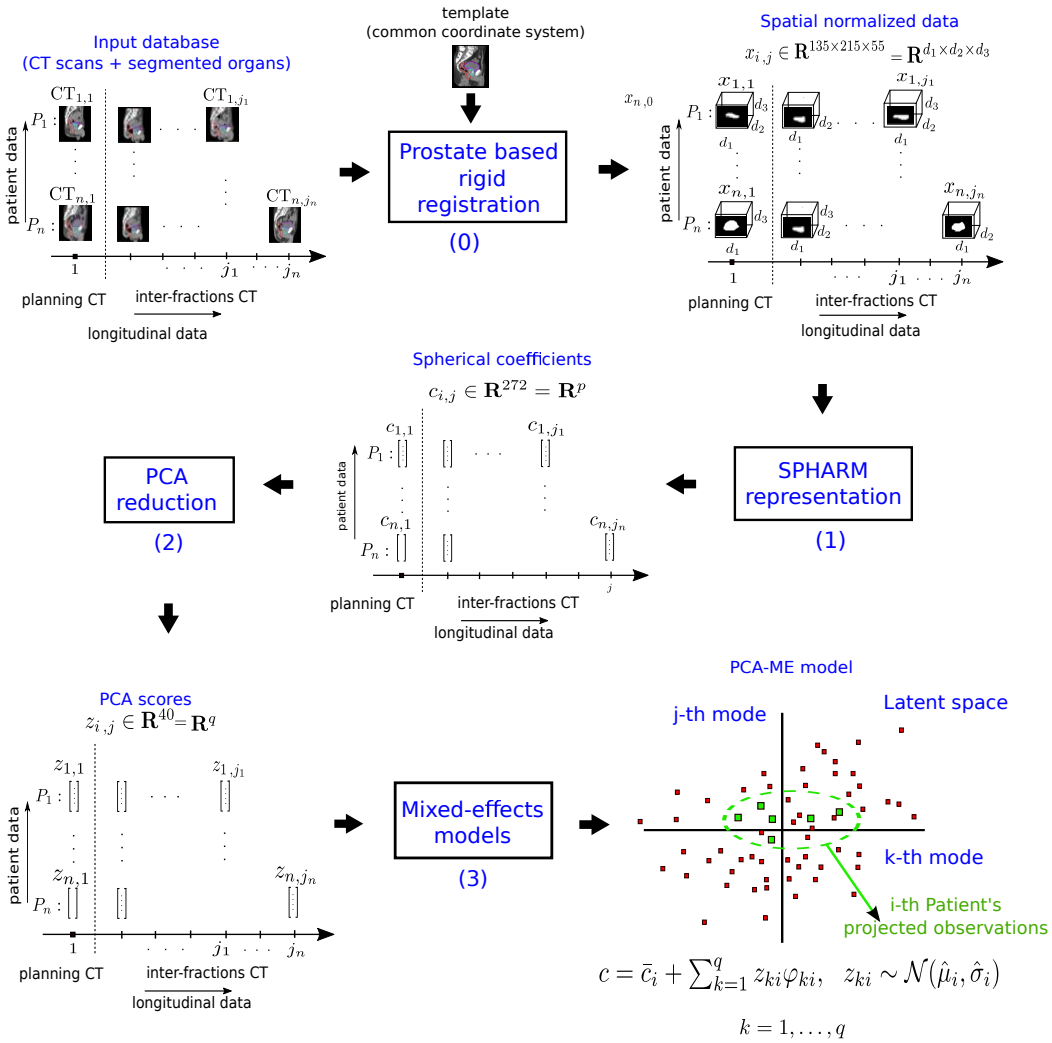

Figure 4.1: Workflow of the method used to train the population-based model. 0) Prostate-based registration, 1) spherical harmonics (SPHARM) representation, 2) principal component analysis (PCA) reduction, 3) mixed-effects model.

$$\mathbf{C}_{empirical} = \frac{1}{n}\sum_{i=1}^{n}\frac{1}{j_i-1}\sum_{j=1}^{j_i}(c_{ij}-\bar{c}_i)(c_{ij}-\bar{c}_i)^T \tag{4.1}$$

$$= \frac{1}{n}\sum_{i=1}^{n}\frac{1}{j_i-1}\sum_{j=1}^{j_i} d_{ij}d_{ij}^T = \mathbf{UDU}^T$$

where $d_{ij} = c_{ij} - \bar{c}_i$, n was the number of patients, j_i was the number of observations

available for the i-th patient, and $\bar{c}_i$ the average shape of the i-th patient. Similarly, $\mathbf{U}$ was a matrix composed of eigenvectors φ_k of $\mathbf{C}_{empirical}$, and $\mathbf{D}$ was the diagonal matrix constructed from its corresponding eigenvalues λ_k, i.e, $\mathbf{C}_{empirical}\varphi_k = \lambda_k\varphi_k$. Eigenvectors φ_k defined the directions of geometric variability of the bladder, called modes. As a result, each bladder in the spherical harmonic space was expressed as a linear combination of the modes, as follows:

$$c_{ij} = \bar{c}_i + z_{ij\,1}\,\varphi_1 + \cdots + z_{ij\,r}\,\varphi_r \tag{4.2}$$

where $z_{ijk} = d_{ij}^T\,\varphi_k$, and r was the rank of covariance matrix $\mathbf{C}_{empirical}$, and equal to the number of available images in the population database. Modes $\{\varphi_k\}_k$ defined a new coordinate system, where each vector d_{ij} was represented by new r coordinates $z_{ij\,1}, \ldots, z_{ij\,r}$. The eigenvalues of matrix D defined a significance ranking for the data variability represented by each mode, attesting $var(\varphi_1) = \lambda_1 \geq var(\varphi_2) = \lambda_2 \geq \cdots \geq var(\varphi_r) = \lambda_r$, and showing that data variability was dominated by the first q modes with $q << r$.

In order to test whether the modes described common directions of bladder motion and deformation among all patients, we performed a leave-one out cross validation on the training database. Thus, the error assessing the difference between the original and reconstructed motion-deformation vector was defined as follows:

$$e_i = \frac{\parallel d_i - \hat{d}_i \parallel}{\parallel d_i \parallel} \tag{4.3}$$

where d_i and $\hat{d}_i$ were the i-th bladder motion-deformation vector and its approximation, respectively. If the reconstruction of d_i was exact, then e_i was equal to 0; otherwise, the value of e_i was between 0 and 1. The mean of the reconstruction error e_i in all the motion-deformation vectors was also calculated, i.e., $\mathcal{M} = (1/N) \cdot \sum_{i=1}^{N} e_i$, where e_i denoted the approximation error of an i-th motion-deformation vector d and N the number of the available images, either in the PCA model or left-out patients.

4.2.2 Linear mixed-effects model

Several longitudinal studies have been designed to investigate anatomical or functional changes over time in objects or variables that are observed repeatedly at several time points [64, 86–89]. For instance, these repeated observations may be brain volume, response to clinical treatments, disease progression, blood pressure, heart motion or tumor evolution, among others [90–94]. In these longitudinal studies, observations may be obtained under changing experimental conditions that are not possible to fully control, leading to considerable variations among subjects in the number and time points of the observations. The resulting data sets, which are known as unbalanced data, have often analyzed using ME models that offer to simultaneously model both the random effects that differentiate one subject from a population and the inherent correlation of repeated measurements in the same subject [65, 86–89, 95, 96]. A linear ME model is then a statistical model that incorporates both "fixed effects", which are parameters

related to the entire population or a certain level of classification factor, as well as "random effects", which are parameters associated with differences among individual subjects drawn at random from a population.

The use of basis functions and ME have already proposed in the literature to account for random effects in longitudinal data. These basis function methods include: smoothing splines, wavelet basis, polynomial basis, and functional principal components [97–100]. In our study, the longitudinal data was encoded in the PCA modes, where the observed motion-deformation vectors in the training database were projected over each mode while a linear ME model was fit to each. The score resulting from each projection could be interpreted as a measure of how much a direction of geometric variability was presented in a motion-deformation vector. The implemented ME model thus aimed the characterization of population and individual bladder variations along each mode by introducing a "patient" factor modeled as a random effect.

Let z be the measure of motion/deformation of an organ along a mode. Considering the patient as the unit of observation state (subject), we used an index i, ranging from 1 to n, to differentiate among patients, and an index j to differentiate between observation times in a patient. The encoded longitudinal data was thus defined as follows:

$$\{z_{11k}, \ldots, z_{1j_1k}\}, \{z_{21k}, \ldots, z_{2j_2k}\}, \cdots, \{z_{n1k}, \ldots, z_{nj_nk}\}, \qquad k = 1, \ldots, q \tag{4.4}$$

with the linear mixed-effects model proposed for each mode described as follows:

$$\begin{gathered} z_{ijk} = \mu_k + b_{ik} + \varepsilon_{ij\,k}, \qquad i = 1, \ldots, n,\ j = 1, \ldots, j_i, \\ b_{ik} \sim \mathcal{N}(0, \sigma_{bk}^2),\ \epsilon_{ijk} \sim \mathcal{N}(0, \sigma_k^2), \end{gathered} \tag{4.5}$$

where μ_k was the mean projection along the k-th mode for the whole population, $b_{i\,k}$ was a random variable representing the deviation of the i-th patient mean from the population mean, and $\varepsilon_{ij,\,k}$ was a random variable representing the deviation for j-th projection of the i-th patient from the i-th patient mean. In addition, variances σ_{bk}^2 and σ_k^2 denote inter and intra-patient variability, respectively. The population based model is thus described as follows:

$$\begin{gathered} c = \bar{c}_i + Wz \\ c = \begin{bmatrix} c_0^0 & c_1^0 & \cdots & c_L^{-L} \end{bmatrix},\ W = \begin{bmatrix} \varphi_1 & \varphi_2 & \cdots & \varphi_q \end{bmatrix},\ z = \begin{bmatrix} z_1 & z_2 & \cdots & z_q \end{bmatrix} \end{gathered} \tag{4.6}$$

where $\bar{c}_i$ was the patient mean shape, $z_k \sim \mathcal{N}(\mu_k, \sigma_{bk}^2 + \sigma_k^2)$, for $k = 1, \ldots, q$.

4.2.3 Out-of-sample problem

We sought to predict a likely motion-deformation region of the bladder for a new patient using only his planning CT information. We described regions of motion/deformation

in terms of 3D probability maps (PM) that express the probability of a voxel being occupied by the bladder during treatment. As shown in Fig. 4.2, the first step was to spatially normalize the out-of-sample patient P_l to match the template patient; secondly, the SPHARM and PCA representations of his delineated bladder $c_{l,0}$ and $z_{l,0}$ were obtained; and thirdly, each ME model was adapted to the new patient by estimating his patient-specific mean and variance $\hat{\mu}_{lk}$ and $\hat{\sigma}_{ljk}$.

In ME models, random subject-specific effects are summarized to predict the response of a new subject. The predictor is a linear combination of both fixed and random effects, and it can be interpreted as a shrinkage estimator. Let us suppose that the l-th patient was included in the data set and we want to estimate the following linear model:

$$z_{ljk} = \mu_k + b_{l\,k} + \epsilon_{lj\,k} \sim \mathcal{N}(\hat{\mu}_{l\,k}, \hat{\sigma}^2_{l\,k}), \qquad j = 1, \ldots, j_l,\ k = 1, \ldots, q \tag{4.7}$$

A shrinkage estimator of $\hat{\mu}_{l\,k} = \mu_k + b_{l\,k}$ is then given by:

$$\hat{\mu}_{l\,k} = \mu_k + \zeta_k\,(\mu_{l\,k} - \mu_k), \quad \zeta_k = \frac{j_l}{j_l + \sigma_k^2/\sigma_{bk}^2}, \quad k = 1, \ldots, q \tag{4.8}$$

where $\mu_{l\,k}$ is the mean of the l-th patient at the k-th mode, and j_l is the number of patient's observations. Term ζ is known as the credibility factor. Similarly, the variance of the prediction error $\hat{\sigma}^2_{l\,k} = var(\epsilon_{lj\,k})$ was given by:

$$\hat{\sigma}^2_{lj\,k} = \left(1 - \frac{\sigma_{bk}^2}{\sigma_k^2 + \sigma_{bk}^2}\right) \frac{n}{\sigma_k^2 + \sigma_{bk}^2} \left(1 - \frac{\sigma_{bk}^2}{\sigma_k^2 + \sigma_{bk}^2}\right) - \frac{(\sigma_{bk}^2)^2}{\sigma_k^2 + \sigma_{bk}^2} + \sigma_k^2 + \sigma_{bk}^2 \tag{4.9}$$

In our study, $\bar{c}_l = c_{l,0}$, $\mu_l = W^T(\bar{c}_l - c_{l,0}) = z_l = 0$ and $j_l = 1$ due to we only had the information obtained from the planning CT. In this way, probable structures of the bladder during treatment were thus inferred after sampling S times the Normal distributed vector z. We used the function mvnrnd of Matlab to drawn random vector of z. Subsequently, each sample of z was mapped to a vector c in the spherical harmonic space using matrix W. Then, binary images representing probable bladder configurations were obtained from the parameterized surfaces that were coded in vectors c. Following this, an estimation of the motion/deformation region was calculated by the ratio between the number of times that a voxel was occupied by the bladder and the S generated samples.

4.2.4 Evaluation of prediction performance

Two additional population PCA-based models were used to compare the model's prediction performance. Considering motion-deformation vectors computed between the observed bladders and population mean bladder, the PCA model implemented by Söhn et al. (2005) was extended to the population data as follows:

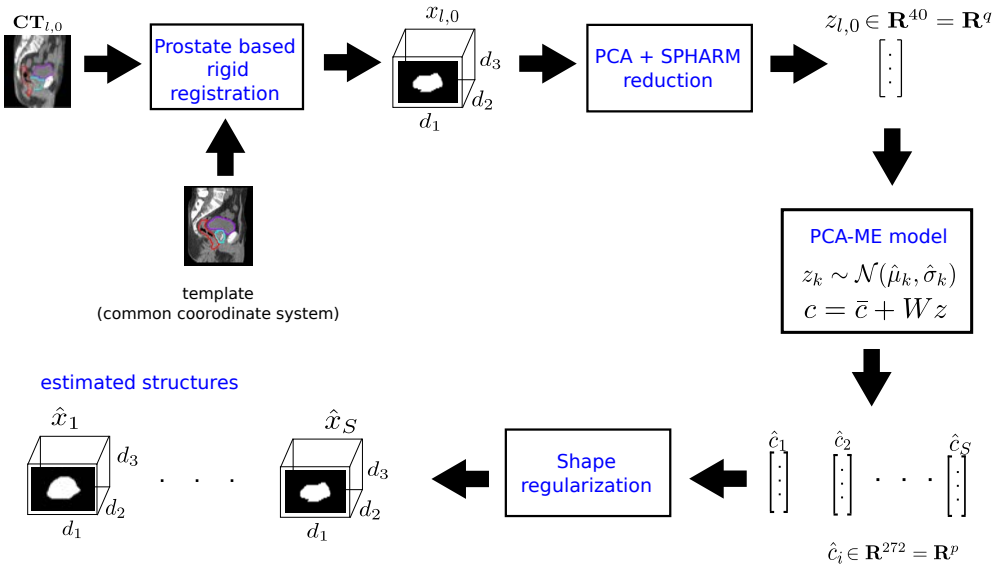

Figure 4.2: Workflow to estimate new structures based on the planning CT for a new patient.

$$c = \bar{c}_{pop} + \sum_{k=1}^{q} z_k \, \psi_k, \tag{4.10a}$$

$$\text{Global PCA model} := \quad z_k \sim \mathcal{N}(0, \alpha_k) \quad \wedge \quad \bar{c}_{pop} = \frac{1}{N} \sum_{i=1}^{n} \sum_{j=1}^{j_i} c_{ij} \tag{4.10b}$$

$$\frac{1}{N-1} \sum_{i=1}^{n} \sum_{j=1}^{j_i} (c_{ij} - \bar{c}_{pop})(c_{ij} - \bar{c}_{pop})^T \, \psi_k = \alpha_k \, \psi_k, \tag{4.10c}$$

where $N = \sum_{i=1}^{n} j_i$ was the total number of observations in the training database, $\bar{c}_{pop}$ was the population mean bladder, and vectors ψ_k were the eigenvectors of the empirical covariance matrix centered in terms of the population mean bladder. Observe that in this model it was thus considered that all the observed bladders in the training set came from a single individual. The second model proposed was taken from Budiarto et al. (2011), defined as follows:

$$c = \bar{c}_i + \sum_{k=1}^{q} z_k \, \varphi_k \tag{4.11a}$$

$$\text{Local PCA model} := \quad z_k \sim \mathcal{N}(0, \lambda_k) \quad \wedge \quad \bar{c}_i = \frac{1}{j_i} \sum_{j=1}^{j_i} c_{ij} \tag{4.11b}$$

$$\mathbf{C}_{empirical} \, \varphi_k = \lambda_k \, \varphi_k, \tag{4.11c}$$

where $\bar{c}_i$ was the mean bladder of the i-th patient, and vectors φ_i were the eigenvectors of empirical covariance $\mathbf{C}_{empirical}$. Then, given a new patient with planned delineated bladder z_l, both PCA models were adapted as follows:

$$\text{Global PCA model} : c = c_{l,0} + \sum_{k=1}^{q} z_k \, \psi_k, \quad \wedge \quad z_k \sim \mathcal{N}(z_l, \alpha_k) \tag{4.12}$$

$$\text{Local PCA model} : c = c_{l,0} + \sum_{k=1}^{q} z_k \, \varphi_k, \quad \wedge \quad z_k \sim \mathcal{N}(z_l, \lambda_k) \tag{4.13}$$

Both PCA based models used the modes to transform the delineated bladder on the planning CT and predict new bladder structures. It is worth mentioning that both sets of modes $\{\psi_k\}$ and $\{\varphi_k\}$ expressed different directions of organ motion and deformation. For example, modes $\{\psi_k\}$ described motion/deformation deltas regarding the population mean bladder whereas modes $\{\varphi_k\}$ described local patient motion/deformation deltas.

The models' prediction performance was evaluated by following leave-one-out cross validation in the training database and also using the independent database. We thus estimated probability maps with each model and compared with the observed PM in both databases. Estimated PMs were derived for each model and patient, as follows: firstly, 40 bladder structures were generated using the bladder observed at the planning CT (i.e. $S = 40$, see Fig. 4.4); and secondly, a distribution of 15 PMs were derived from the 40 estimated structures, where each PM was obtained from a sub-set of estimated bladders (without replacement) whose cardinality was equal to the number of available CT/CBCTs. The value $S = 40$ and $PMs = 15$ were an arbitrary number aiming to obtain a enough sampling of probable bladder contours and PMs of the patient during treatment.

Four PMs were thus calculated for each out-sample patient: one PM estimated by means of the proposed model, labeled $PM_{Local\,PCA-ME}$; one PM obtained from the patient's observed available images, labeled PM_{obs}; one PM estimated by means of the global PCA model, labeled $PM_{Global\,PCA}$; and one PM estimated by using the local PCA model, labeled $PM_{Local\,PCA}$.

4.2.5 Metrics of similarity between PMs

Two metrics were proposed for assessing the similarity between two PMs X and Y.

4.2.5.1 Mutual information-based metric

$$dist_{intensity}(X,Y) = 1 - \frac{I(X,Y)}{H(X,Y)} \tag{4.14}$$

$$H(X,Y) = -\sum_{x,y} p_{XY}(x,y) \log P_{XY}(x,y)$$

$$I(X,Y) = H(X) + H(Y) - H(X,Y)$$

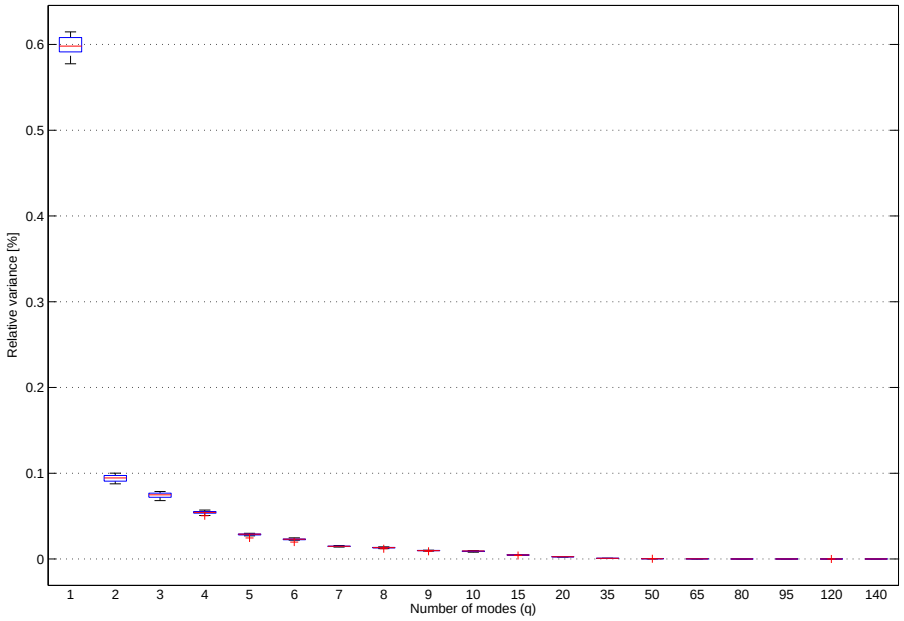

Figure 4.3: Relative mode variances obtained from the PCA in the training database (relative values: sum of all eigenvalues normalized to 100%).

where $I(X,Y)$ and $H(X,Y)$) denoted mutual information (MI) and joint entropy between X and Y, respectively. Similarly, x and y corresponded to intensity values in the voxels of X and Y, respectively. $H(X)$ and $H(y)$ denoted marginal entropies of each image. MI measures the amount of information that both images share (redundant information) based on the intensities of corresponding voxels, which is assumed to be maximal if both images are geometrically aligned. Similarly, joint entropy measures the uncertainty or dispersion between images. $dist_{intensity}$ also provided a distance based on the ratio of dependence and dispersion between two PMs, attesting $dist_{intensity}(X,Y)$ $= 0$ iff $X = Y$, and $dist_{intensity}(X,Y) \leq 1$ for all pairs (X,Y) [101–103]. It offers the advantage of not making any prior assumptions regarding the functional relationship between images. Since we were dealing with probability images, each voxel was considered as a discrete random variable. Joint and marginal entropies were calculated by normalizing the joint, and marginal histograms, i.e a (joint) probability distribution of intensity values were estimated by counting the number of times each value occurred in the images and dividing this value by the total number of voxels.

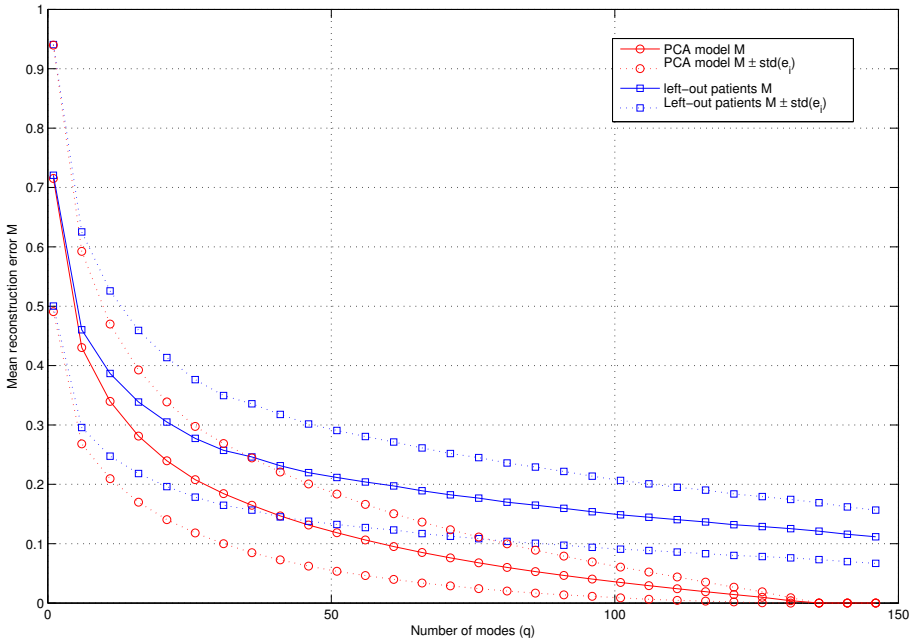

Figure 4.4: Mean approximation error $\mathcal{M}$ as a function of the number of modes in the PCA model and left-out patients. There are bands (dotted-lines) that represent the mean approximation error $\mathcal{M}$ (solid-lines) plus and minus one standard deviation of e_i (see Eq. 4.3).

4.2.5.2 Metric of misestimated voxel

We also proposed an error metric to assess whether a voxel was overestimated or underestimated. Denoting v as a voxel, let $X_b = \{v/X(v) > 0\}$ be the binary image obtained by those voxels with a probability greater than 0. The proposed metric is defined as follows:

$$\text{Accuracy}(X, Y) = \frac{|X_p \cap Y_p| + |\overline{X}_p \cap \overline{Y}_p|}{d} \tag{4.15}$$

where d denoted the total number of voxels (see Eq. **??**), $|\cdot|$ denoted the cardinality, and $\overline{X}_p$ and $\overline{Y}_p$ denoted the complement of X_p and Y_p, respectively. As a result, this metric provided the proportion of the properly estimated voxels (i.e. both true positives and negatives voxels in the motion/deformation region) among the total number of voxels.

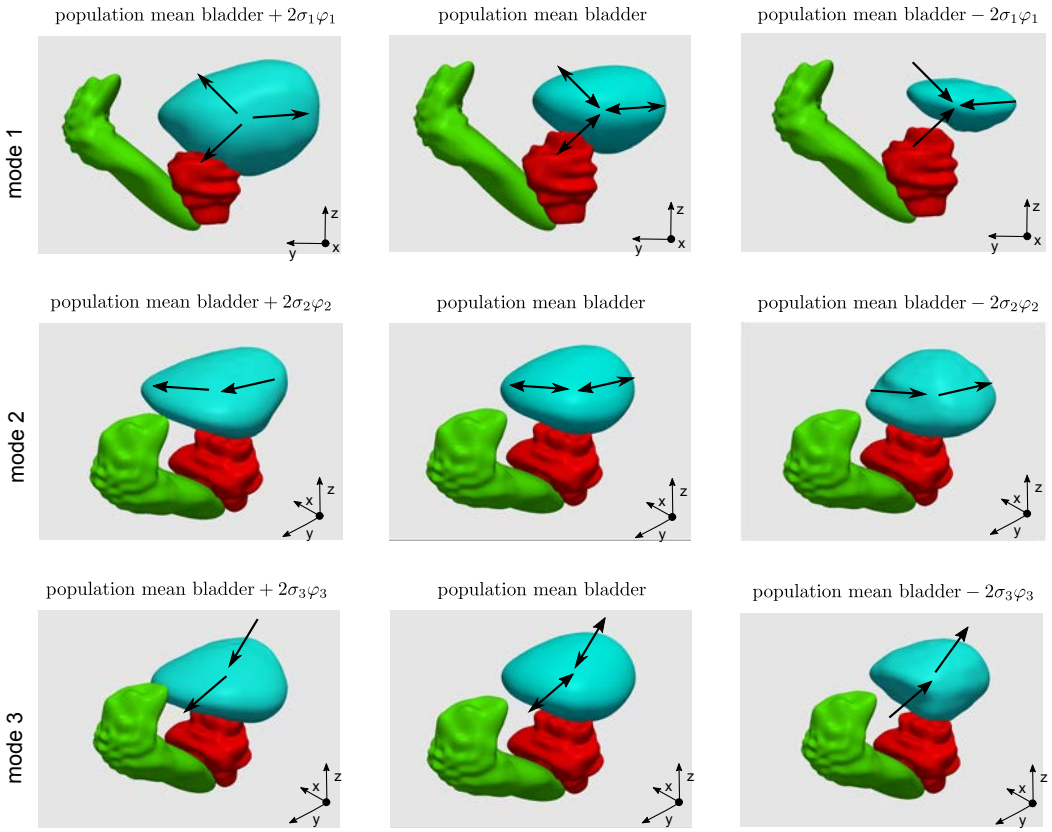

Figure 4.5: 3D sagittal views of the first three motion/deformation modes applied on the population mean bladder (center column). The left and right columns correspond to geometric variations along the respective mode φ_i, defined as *population mean bladder* $\pm$ $2\sigma_i\varphi_i$, where σ_i^2 is the mode variance. The prostate (red color) and rectum (green color) of the template patient were also included as spatial reference.

4.3 Results

The analysis was carried out in MATLAB (R2014a). The eigenvectors φ_k and ψ_k were obtained using the function eigs while the ME model of each score z_{ijk} was fit using the function fitlme with restricted maximum likelihood estimation (REML) as estimation method [65, 104].

4.3.1 PCA representation

Fig. 4.3 shows the eigenvalue spectrum of all 20 combinations of cutting the training database from the leave-one-out cross validation. The number of columns of the covariance matrix $\mathbf{C}_{empirical}$ varied between 151 and 154 (i.e. the available images after removing the left-out patient). The first mode contributed the largest variance (approximately 60% of the variability); similarly, the second, third, and fourth modes

contributed, on average, 9%, 7.8% and 5% of the variability, respectively. The first eight modes contributed 90% of the cumulative variance, on average. Meanwhile, Fig. 4.4 shows that both mean and standard deviation of the approximation error $\mathcal{M}$ decreased as the number of modes was increased in both the PCA model and left-out patients. However, mean and standard deviation of the reconstruction error $\mathcal{M}$ did not reach the value of zero in the left-out patients, and they exhibited a lower decreasing rate after the first eight modes. Considering only the first 60 modes, the mean reconstruction error $\mathcal{M}$ was 10% and 20% in the PCA model and left-out patient, respectively. When truncating the first 40, it still obtained an average accumulated variability of 98% and an average reconstruction error of 15% and 23% for the PCA model and left-out patients, respectively. Therefore, after performing two phases of dimensionality reduction, any bladder was represented as a vector of $q = 40$ scores ($q = 40 << p = 272 << d = 1596375$). Fig. 4.4 also shows bands (dotted lines) around the mean approximation error $\mathcal{M}$, which represent the mean plus and minus one standard deviation of e_i (see Eq. 4.3). It can be observed that the variance also decreased as the number of modes was increased in both the PCA model and left-out patients.

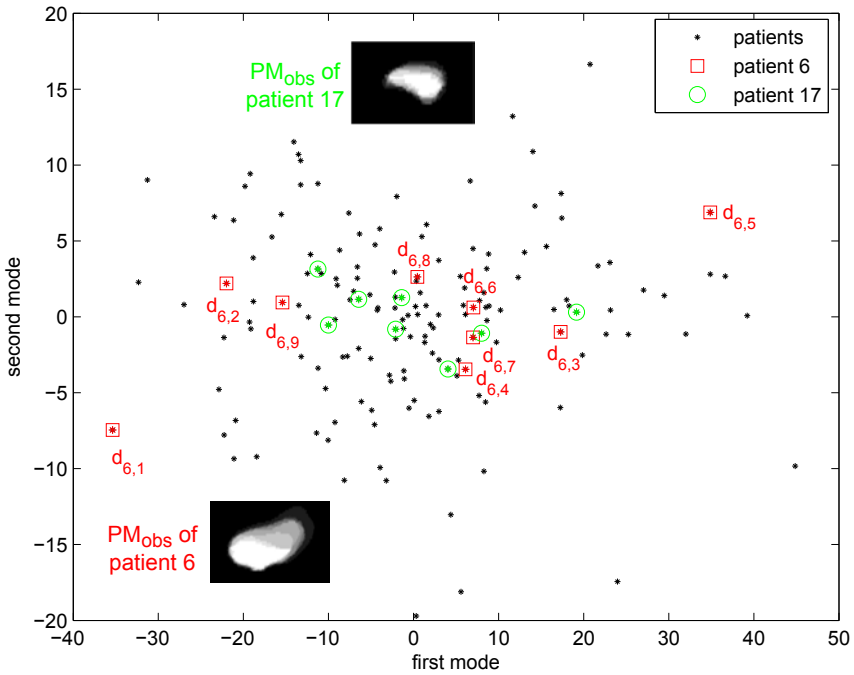

Figure 4.6: Scatterplot of the patients from the training database projected in the first two modes (black points). Color circles and squares correspond to the vectors of two individuals. $d_{6,j}$ denotes the observed motion/deformation vectors of Patient 6's bladder.

Fig. 4.5 presents sagittal views of the first three modes over the mean bladder

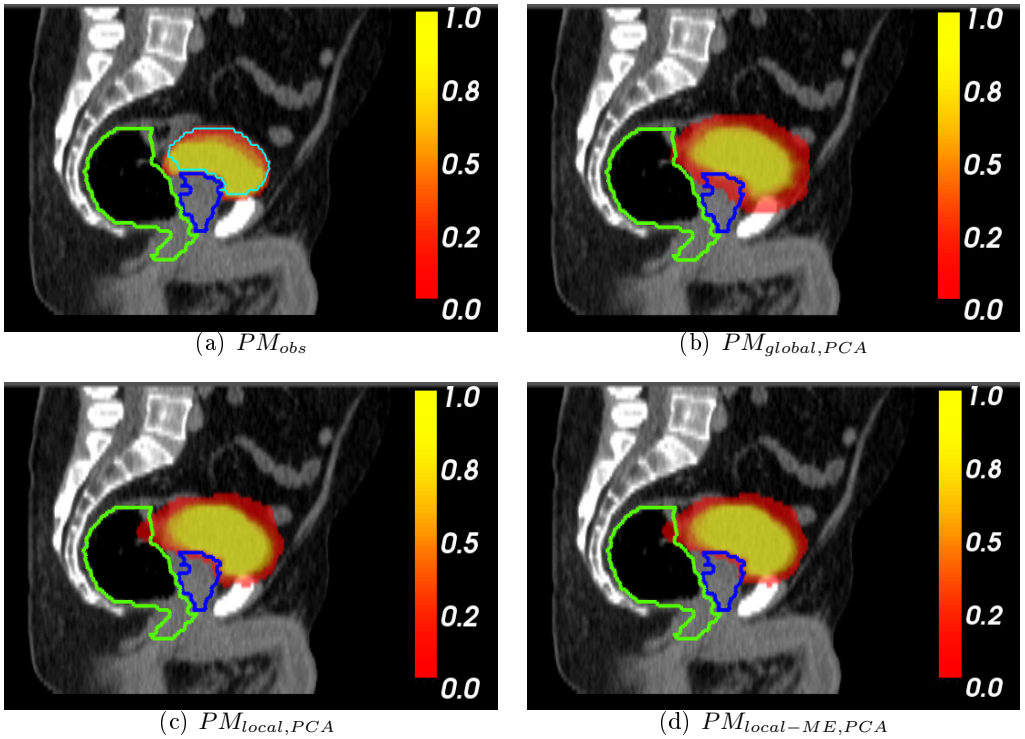

(a) PM_{obs} (b) $PM_{global,PCA}$

(c) $PM_{local,PCA}$ (d) $PM_{local-ME,PCA}$

Figure 4.7: 3D sagittal views of PMs obtained for one patient in the training database as an out-of-sample patient. Segmented prostate (blue) and rectum (green) at the planning CT scan are overlaid. Top left figure also depicts the segmented bladder (cyan) at the planning CT.

of the training database. The first mode was associated with bladder volume. Similarly, modes with greater indices, like the second and third, represented directions of dilation and contraction in some regions. For example, the second mode indicated dilation/contraction in the left-dorsal and right-ventral regions of the bladder whereas the third mode indicated dilation/contraction in the inferior-ventral and dorsal regions.

Fig. 4.6 depicts the projection of the motion/deformation vectors of the training patients on the space generated by the first two modes, where each point represents the observed geometric variations along these two modes. This figure also presents the observed motion/deformation vectors of Patient 6, indicating that the geometric variation followed a random trajectory. In addition, we can observe that Patient 6 and 17 had variance that differed both between them and from the mode's population variance. For example, Patient 6's bladder exhibited greater changes in volume during treatment than that of Patient 17, as shown in the PMs of both patients, proving that Patient 6's specific-variance along the first mode was greater than that of Patient 17. In addition, we also observed that Patient 17's variance of along the second mode was very slight due to the geometric variations of his bladder being greater in the inferior-medial and dorsal regions.

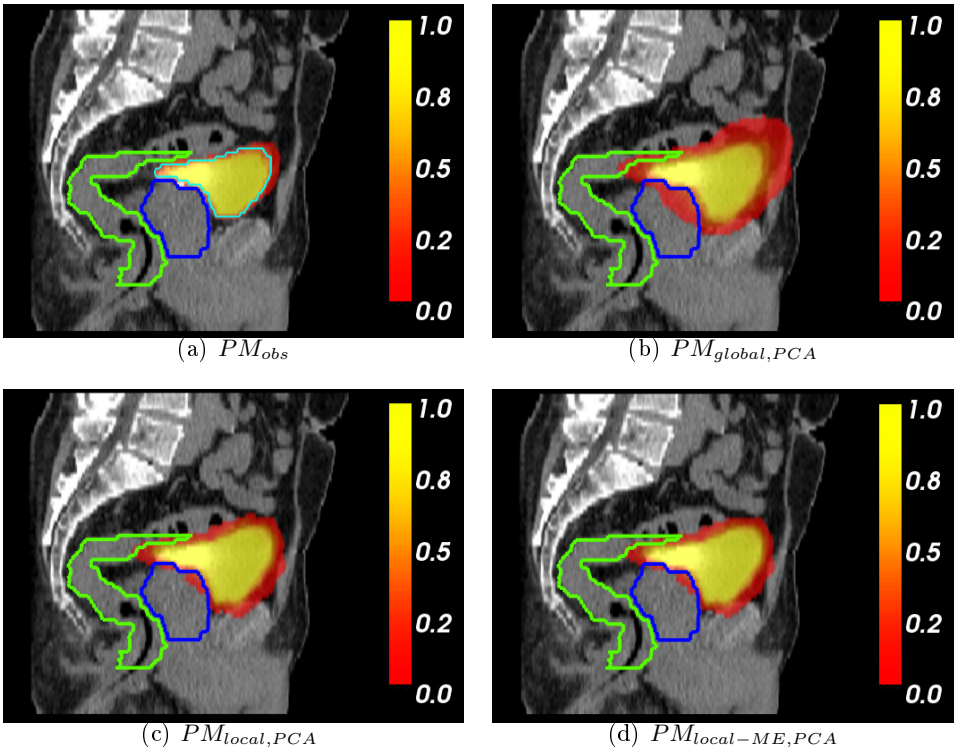

(a) PM_{obs} (b) $PM_{global,PCA}$

(c) $PM_{local,PCA}$ (d) $PM_{local-ME,PCA}$

Figure 4.8: 3D sagittal views of PMs obtained for one patient in the validation database as an out-of-sample patient. Segmented prostate (blue) and rectum (green) at the planning CT scan are overlaid. Top left figure also depicts the segmented bladder (cyan) at the planning CT.

4.3.2 Evaluation of performance prediction with groundwork models

Fig. 4.7 and 4.8 demonstrates the PMs obtained by all three models and the available observations of two patients as out-sample patients (one for each database). In both patients, the Global and Local PCA model overestimated more voxels than our proposed model. Tables 4.1 and 4.2 present the averages obtained by these metrics for these patients.

Fig. 4.9 depicts the averages of the metric $dist_{intensity}$ for patients in both databases. On average, the global PCA model obtained the highest measures of dissimilarity in both databases while our proposed model obtained the lowest measures. Similarly, Fig. 4.10 also shows the averages of the metric Accuracy for patients in both databases. On average, the global PCA model also obtained the lowest accuracy in both databases while our proposed model obtained the highest. For each patient and metric, a significant test was made between the PCA models using the Wilcoxon rank sum test for all 15 $dist_{intensity}$ and Accuracy values. The Table 4.3 shows the number of patients that had significant difference in both databases. Besides, we also obtained four variance distributions by deriving the variance of the 15 values for each metric and patient in

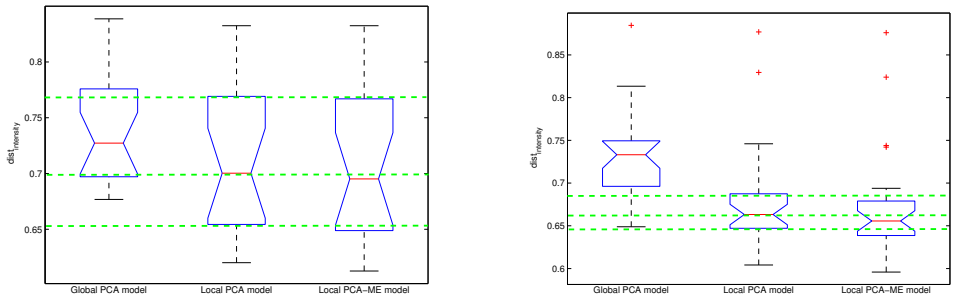

(a) training database (b) validation database

Figure 4.9: Average $dist_{intensity}$ values of observed and estimated PMs for patients in both databases.

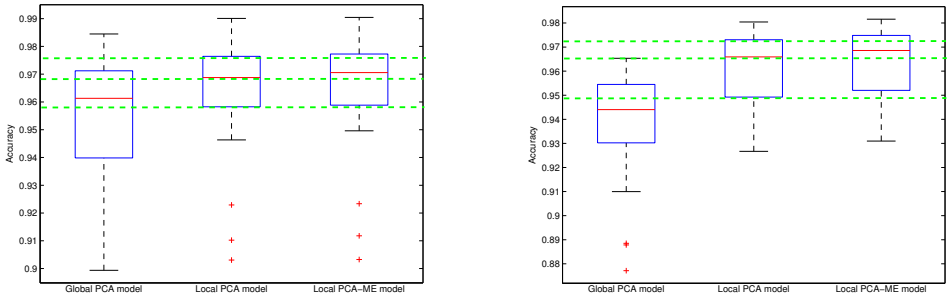

(a) training database (b) validation database

Figure 4.10: Average *Accuracy* values of observed and estimated PMs for patients in both databases.

Table 4.1: Averaged values from the metric $dist_{intensity}$ for two patients between estimated and observed PMs.

Patient	PM_{obs} vs $PM_{Global\,PCA}$	PM_{obs} vs $PM_{Local\,PCA}$	PM_{obs} vs $PM_{Local\,PCA-ME}$
Training database	0.691	0.676	0.66
Validation database	0.74	0.66	0.65

Table 4.2: Averaged values from the metric *Accuracy* for two patients between estimated and observed PMs.

Patient	PM_{obs} vs $PM_{Global\,PCA}$	PM_{obs} vs $PM_{Local\,PCA}$	PM_{obs} vs $PM_{Local\,PCA-ME}$
Training database	0.968	0.972	0.98
Validation database	0.946	0.97	0.975

both databases. Table 4.4 presents the p-values of the significant tests that were made between these variance distributions of the PCA models using the Wilcoxon rank sum test.

Fig. 4.11 also presents the average joint histograms of the voxel intensities of PM_{obs} vs $PM_{Local\,PCA-ME} - PM_{Global\,PCA}$ and PM_{obs} vs $PM_{Local\,PCA-ME} - PM_{Local\,PCA}$ in both database. This presents the number of times that a joint intensity value was repeated between the observed and estimated PMs. For example, Figs. 4.11a and 4.11c reveal that the global PCA overestimated more voxels than our proposed model in both databases in probabilities p ranging between 0 and 0.6 instead of the observed value of $p = 0$. Meanwhile, Figs. 4.11b and 4.11d demonstrate that our proposed model was also more capable of estimating voxels observed with probability $p = 0$.

Table 4.3: Number of patients exhibiting significance difference using the Wilcoxon rank sum test in both databases.

Database	Local PCA-ME model vs Global PCA model $dist_{intensity}$/Accuracy	Local PCA model vs Global PCA model $dist_{intensity}$/Accuracy	Local PCA-ME model vs Local PCA model $dist_{intensity}$/Accuracy
Training	17/18	17/14	0/0
Validation	20/27	20/26	5/3

Table 4.4: p-values of the Wilcoxon rank sum tests for the variance distributions between PCA models in both databases.

Database	Local PCA-ME model vs Global PCA model $dist_{intensity}$/Accuracy	Local PCA model vs Global PCA model $dist_{intensity}$/Accuracy	Local PCA-ME model vs Local PCA model $dist_{intensity}$/Accuracy
Training	0.0411/0.0001	0.0720/0.003	0.6/0.32
Validation	$0.037/3 * 10^{-5}$	0.10/0.0001	0.51/0.44

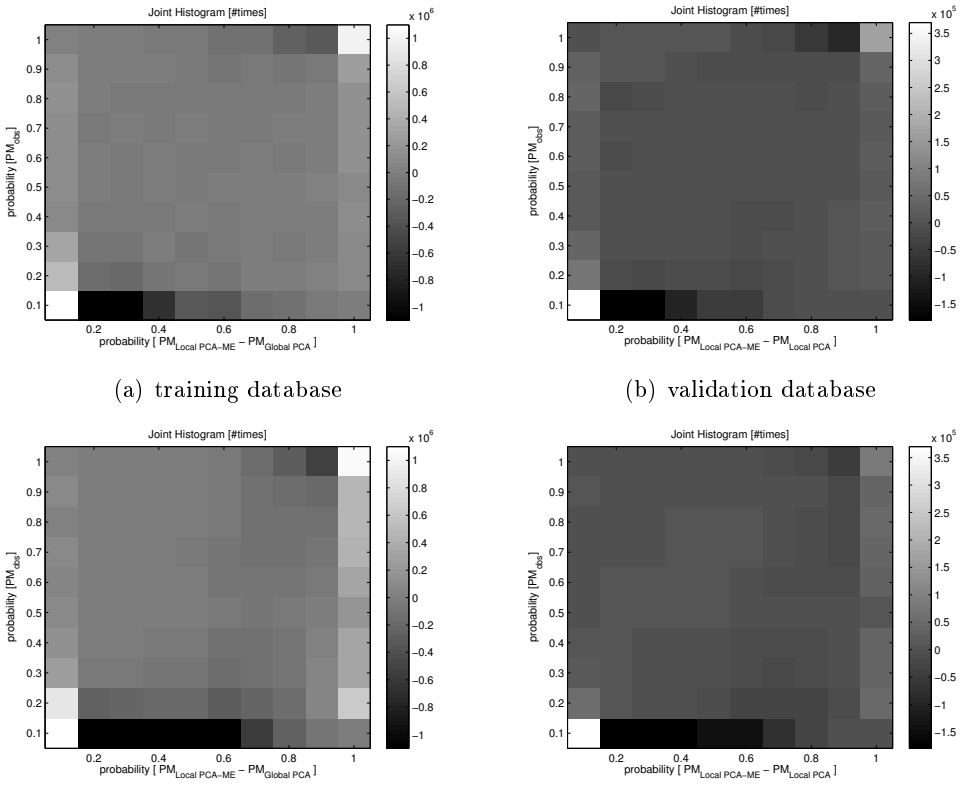

(a) training database

(b) validation database

(c) training database

(d) validation database

Figure 4.11: Average joint histograms of observed and estimated PMs for patients in the training and validation database. Left column shows the average joint histograms between PM_{obs} vs $PM_{Local\,PCA-ME} - PM_{Global\,PCA}$ while right column shows the average joint histograms between PM_{obs} vs $PM_{Local\,PCA-ME} - PM_{Local\,PCA}$.

4.4 Discussion

We have hereby proposed a new methodology for predicting bladder motion and deformation between fractions in prostate cancer radiotherapy via population analysis. We calculated bladder motion and deformation regions based solely on the planning CT scan. In order to predict which regions were likely to exhibit motion/deformation, we first performed a prostate-based rigid-registration alignment, two dimensionality reduction steps, and fitting regression. The first dimensionality reduction step consisted of surface parameterization of the bladder in the spherical harmonic space. The second step of dimensionality reduction was to determine the directions of bladder geometric variability by means of PCA. These directions, called modes, were validated by leave-one-out cross validation. Following this, an ME model was fitted along each mode to the longitudinal data defined by the projections of motion/deformation vectors observed in the training database. We used leave-one-out cross validation on the training database and an external database to validate the model. The proposed model was then compared to two additional population PCA based models. Motion/deformation regions were characterized by means of probability maps (PMs) and metrics were provided in order to measure similarities between observed and estimated PMs.

When considering population-based models developed for pelvic organs, we found that 15 modes were required to describe 90% of CTV motion and deformation for prostate cancer [54]. For rectum cancer, 28 modes were found to be required to describe 90% of the accumulated variability in CTVs [55]. In contrast, eight modes were sufficient in our study to describe the same percentage of accumulated variability. On analysis of the three methods' results, we noted that there were less fundamental directions of geometric variability in the bladder compared to other pelvic organs, despite its great volume and shape variations. Nevertheless, we were interested to note that more directions were observed in the prostate/SV composition, potentially due to the prostate and seminal vesicle centroids move independently [105], or due to patient-specific variations and delineation errors. Regarding the rectum, its greater number of directions may result from its flexible and vertical structure, enabling it to deform in any direction along its major axis [44], in addition to patient-specific variations and delineation errors. Future studies using other population databases would be required to confirm or contradict the number of principal directions of motion and deformation reported in these organs.

On the other hand, as in [54], the reconstruction error in the PCA model and left-out patients in our study tended to decrease towards 0 as the number of modes was increased. However, the error did not completely disappear in the left-out patients, meaning that not all individual directions were accounted for by the PCA modes. In addition, as observed in Fig. 4.4, the rate in the left-out patient curve decreased after the first eight modes, implying that the order of the modes was not preserved in all patients. As a result, both of these issues may significantly affect the performance of any population PCA model. For example, the lowest measures of similarity were observed in Patients 6, 12, and 20 in the training database, whose bladders exhibited geometric variations in the superior-ventral region (see Patient 6's PM in Fig. 4.6). These variations were

not represented by at least the first four modes (81% of the accumulated variability). It would therefore be interesting for future studies to first make a classification of bladders with similar shapes [56], then design the proposed model locally for each subgroup. For example, [106] introduced a methodology for developing hierarchical PCA models where each observation is plotted in the latent space to determine the number of sub-PCA models in the inferior levels.

It is also crucial to emphasize that we applied a quadratic relative error in the SPHARM space to assess the modes in our study, unlike [54], who used a quadratic error normalized by the number of points. Nevertheless, we considered it possible to compare the behavior of both errors. For example, [54] required 37 modes to reduce the initial error by 62% in the left-out patients, whereas 60 modes were needed in our study to reduce it by 80%. Both results may indicate there was significant intra-patient variability that was not sufficiently detected by the first modes obtained from the population. This also means that intra-patient variability may be higher in the bladder, potentially due to anatomical differences among patients and delineation errors. In this way, a trade-off was made between accumulated variability and the reconstruction error for determining the number of modes (40) in our PCA model, where an additional 20 modes only reduced the reconstruction error by 3%.

As established in the model assumptions, each mode corresponded to a direction of geometric variability that dilated or contracted certain regions of the bladder. Unlike the first mode, not all the rest were found to define an affine transformation that may be initially applied in the setup, such as rotation along an axis or a uniform dilation/contraction. In addition, we showed that the bladder motion and deformation between fractions follows random trajectory, as the data projections showed in the latent space (see Fig. 4.6). It was also possible, in this space, to characterize the geometric variations of each patient, where some directions were clearly found to be more dominant than others.

Although several studies have previously addressed the estimation of motion/ deformation regions of the pelvic organs by means of the coverage matrix concept [25,38, 41,107], this is the first, to our knowledge, to introduce a quantitative and qualitative comparison between estimated and observed regions using metrics of similarity and joint histograms. As observed in Figs. 4.9, 4.10, and 4.11, our proposed model obtained the lowest measures of dissimilarity and misestimated voxels. Previous population PCA models have thus overestimated or underestimated more voxels, primarily those not occupied by the bladder. As a result, our proposed model reduced uncertainties in estimations of the probable region of motion and deformation. This was achievable as the ME models enable us to reduce the observed population variance along each mode by grouping repeated observations per patient. For example, we obtained more patients presenting significant differences between the Global PCA model and our proposed model in both databases than the Local PCA model; moreover, we significantly reduced uncertainties in estimations of motion/deformation region regarding the Global PCA model (see Table 4). We therefore concluded that the Global, Local, and Local PCA-ME models provided a progressive decrease in uncertainties for estimating likely motion/deformation regions, while our proposed model led to the lowest reduction in all

the patients (see Fig. 4.9 and 4.10). When more CTs/CBCTs scans become available for a patient during treatment, this information could be used to improve estimation of the motion/deformation region by personalizing modes, variance, and mean bladder shape. It is worth mentioning that one limitation to use PCA models for modeling organ motion and deformation is their strong dependence on the organ's mean shape, as planning CT scans may not provide a good estimation. Future studies should be focused on analyzing the methodology's robustness for handling outlier patients whose variance along a mode is almost similar to the population variance. This kind of patient may lead to a misestimation of the intra-patient variability σ^2 affecting the performance of the ME model (see Patient 6 in the training database in Fig. 4.6). A robust formulation of PCA, the so-called robust PCA, could help overcome the problems associated with outlier patients.

PCA-based shape models are typically efficient for organs whose shape variations can be captured by a reasonable number of modes [108]. For instance, two studies have shown that 15 and 16 modes were required to describe most of the inter- and intra-patient motion and deformation of CTVs in prostate and rectum cancer, respectively [54, 55]. However, in population databases concerning highly-varying soft-tissue volumes, a large number of modes may be required to properly capture the complex shape variations observed in the training database. In our study, for instance, we required 40 modes to generate an inter-patient PCA model for the bladder. We believe that the large number of modes may render interpretation of higher modes difficult, as they may not describe directions of geometric variability observed in the population rather than patient-specific directions. In addition, the large number of modes may also hinder inference and analysis of the results for each ME model. However, as in [100], the modes define an orthogonal basis that enables us to consider each score z_{ijk} as an independent random variable across k that can be easily modeled as a response variable [109, 110].

We have previously mentioned that the scores can be interpreted as measures of geometric variability along the modes. Future studies should therefore focus on determining covariates that may help to describe patient-specific bladder deformation. The results displayed in Fig. 4.6 and published by [56] appear to indicate that there are some covariates that may underlie the motion/deformation region in the latent space or mode's variance for any arbitrary patient. For example, bladder size or volume could be considered as fixed parameters that may determine changes in volume and directions of geometric variations. [56] and [111] reported, in line with Fig. 4.6, that bladders with large volumes exhibited geometric variations in the superior-ventral region and higher variance along the first mode. In an adaptive radiotherapy scheme, a time covariate can also be added, as a random or fixed variable, to describe the daily volume changes of the bladder.

As previously stated, Hu et al. [66] proposed a population-PCA model to describe prostate deformation in MR-tumor-targeted biopsies. Concerning this methodology, we found two shared characteristics: firstly, that the scores were also considered as parameters that describe intra-subject organ motion; secondly, the added objective of characterizing subject-specific probability density functions (SSPDFs) of motion and deformation (parameterized by means of multivariate Gaussian distributions). How-

ever, [66] proposed a fixed-effects model to describe SSPDF of the scores across the population, while such a model consists of a multivariate non-linear regression involving the scores of the reference shapes defined as covariates. [66] also decided to model the SSPDF parameters instead of the subject-specific scores, as proposed in our study. Nevertheless, we believe that it could be interesting for future studies to add the scores of the bladder segmented at the planning CT as fixed variables, as this may help to correlate the subject-specific variance and directions of geometric variability. For future works, we wish to underline that both studies have suggested the possibility of including other parameters in the learning framework, such as organ size or any temporal information.

For future developments, it is worth noting that our main goal has been to predict late GU toxicity based only on planning treatment information, and we thus only used the planning CT scan to predict bladder motion/deformation regions. Nonetheless, we have also performed some simulations using two and three observations of the out-of-sample patient, with the aim of simulating an adaptive radiotherapy treatment, and the results achieved better estimation of the region. We think that the number of observations for the out-of-sample patient helps to decrease the variance of the estimate for the shrinkage predictor. Thus, the more observations we have for the out-of-sample patient, the more certain we can be about how the patient differs from the population mean. In these simulations, it is also worth mentioning that we only used these observations to improve the estimation of the patient's average bladder and shrinkage estimator of each mode, i.e. to improve the model adaptation yet not retrain the model's parameters (modes φ_k, and inter- intra-patient variances). We considered that more observations should be available to fit the model's parameters again, as five CTs/CBCTs has been established as the minimum number of observations required for intra-patient models [57].

In this study, we described regions of motion/deformation in terms of 3D probability maps (PM) that were obtained by sampling the model's distribution or using patient images. We have thus considered motion/deformation regions as histograms that can be compared using the proposed metrics. We believe that the next step should be focused on estimating the uncertainty of the motion/deformation region using the model's joint distribution. However, we considered that the large number of modes may hinder inference of the associated joint distribution, as the number of combinations of scores at the boundaries of the confidence intervals will significantly grow when we add modes to the joint distribution. Nonetheless, we consider that the uncertainty region can also be estimated using only those modes that have a strong influence on variables, like the accumulated delivered dose, i.e., that the uncertainty region can be restricted to those modes that have a strong influence on the mean accumulated dose. Finally, it may also be interesting to add linear modes that describe geometric variations between the mean bladders of the patients as the modes obtained from the covariance matrix $\mathbf{C}_{empirical}$ only described directions observed on the intra-patient level. These models are known as multi-level PCA models [112, 113].

4.5 Conclusion

We proposed a population based model to predict bladder motion and deformation between fractions using solely the planning CT. In comparison with previous studies, our proposed model was able to decrease uncertainty in the estimation of the region where the bladder will likely move and deform. We also demonstrated that, by following a longitudinal study with ME models, it was possible to separate the patient-specific variance from population variance and thus reduce the total variance. The potential applications of this model include margin evaluation, delivered dose estimation, toxicity prediction, and the design of robust treatment plans, among others. Future studies should now be conducted to validate the proposed model by means of a large cohort of patients who have undergone prostate cancer radiotherapy. It could also be valuable to focus on the relationship between inter-fraction bladder motion/deformation, delivered dose, and late GU toxicity in the prostate cancer radiotherapy context.

Chapter 5

Population PCA-based models using a longitudinal approach: characterization of patient-specific modes from the population modes

This chapter proposes hierarchical PCA to properly characterize patient-specific modes from the population modes. This study included two population databases of patients previously described in Chapter 4. As in previous population-PCA models, we use the data to obtain the dominant eigenmodes that describe bladder geometric variations. However, PCA-based models have the limitation of not being suitable to properly capture the latent structure of longitudinal data of organs with highly varying soft-tissue. We propose hierarchical modes to separate intra- and inter-patient bladder variability. This model was derived by following a hierarchical visualization algorithm that was initially proposed in Ref. 106. This algorithm seeks to design a single flexible model by hierarchically nesting latent variable models, which reveals the internal structure of a complex data set. The population database of 20 patients was initially used to derive a top-level PCA model that describe the entire structure of the bladder space. This space was subsequently divided into subspaces by lower-level PCA models describing the internal structure of clusters. The model was evaluated using a reconstruction error and compared with a conventional PCA model following leave-one-out cross validation. Probability maps (PMs) were also generated, which were compared with the observed region using a metric based on mutual information.

A similar methodology was also proposed by Foruzan et al. [60] to model shape variations in a population database of livers. However, two differences were observed: firstly, that the tree-like structure of the hierarchy was not defined by using a visualization algorithm; and secondly, that the population database of livers used in the study was not longitudinal. The methodology proposed in this chapter was submitted in the 12th International Symposium on Medical Information Processing and Analysis (SIPAIM) in Tandil, Argentina.

The chapter is organized as follows. Section 5.1 describes the database used in this study. Section 5.2 subsequently presents a detailed description of the proposed hierarchical method together with the validation framework. Section 5.3 then presents the results and validation with the conventional PCA model. Lastly, section 5.4 discusses the experimental findings, with a conclusion in section 5.5 in addition to final considerations and future work.

5.1 Data

We included the training and validation databases previously described in Chapters 2. Population-based models were thus trained using the training database. Meanwhile, the prediction performance of the model was evaluated by following leave-one-out cross validation in the training database and also using the validation database.

5.2 Methods

Fig. 5.1 describes the steps followed to train the hierarchical population-based PCA model. The first and second step were also to spatially normalize all the bladders in the same spatial referential and to parameterize the bladder surface using SPHARM coefficients, respectively. The third step was then to perform a dimensionality reduction using hierarchical eigenmodes, followed by mixed effects models. Finally, the last step was the validation framework, where we also developed a conventional population-based PCA model to test the performance of our proposed model.

5.2.1 Hierarchical Principal Component Analysis

This step was sought to determine a hierarchical structure of modes that properly characterized the patient-specific modes from the population. We performed a hierarchical visualization algorithm proposed by Bishop and Tipping (1998) in order to design a population-based PCA model (see Fig. 5.1).

5.2.1.1 Top-level PCA model

This step aimed to determine the most important modes that describe all the bladder shapes and sizes observed in the training database, i.e. it was aimed to characterize the bladder space as in Chapter 3. A data matrix $\mathbf{S}_{snapshot}$ was then obtained by stacking as a column each vector shape represented in spherical harmonics. Denoting the observed bladder shape of the i-th patient at the j-th CT parametrized as c_{ij}, the data matrix $\mathbf{S}_{snapshot}$ was defined as follows:

$$\mathbf{S}_{snapshot} = \begin{bmatrix} c_{10} & c_{11} & \cdots & c_{1j_1} & c_{21} & \cdots & c_{n1} & \cdots & c_{nj_n} \end{bmatrix} = \mathbf{U}\mathbf{\Sigma}\mathbf{V}^T \tag{5.1}$$

where j_i was the number of observations available for the i-th patient, $\mathbf{\Sigma}$ was the diagonal singular value matrix, and $\mathbf{U}$ and $\mathbf{V}$ were left and right singular vectors,

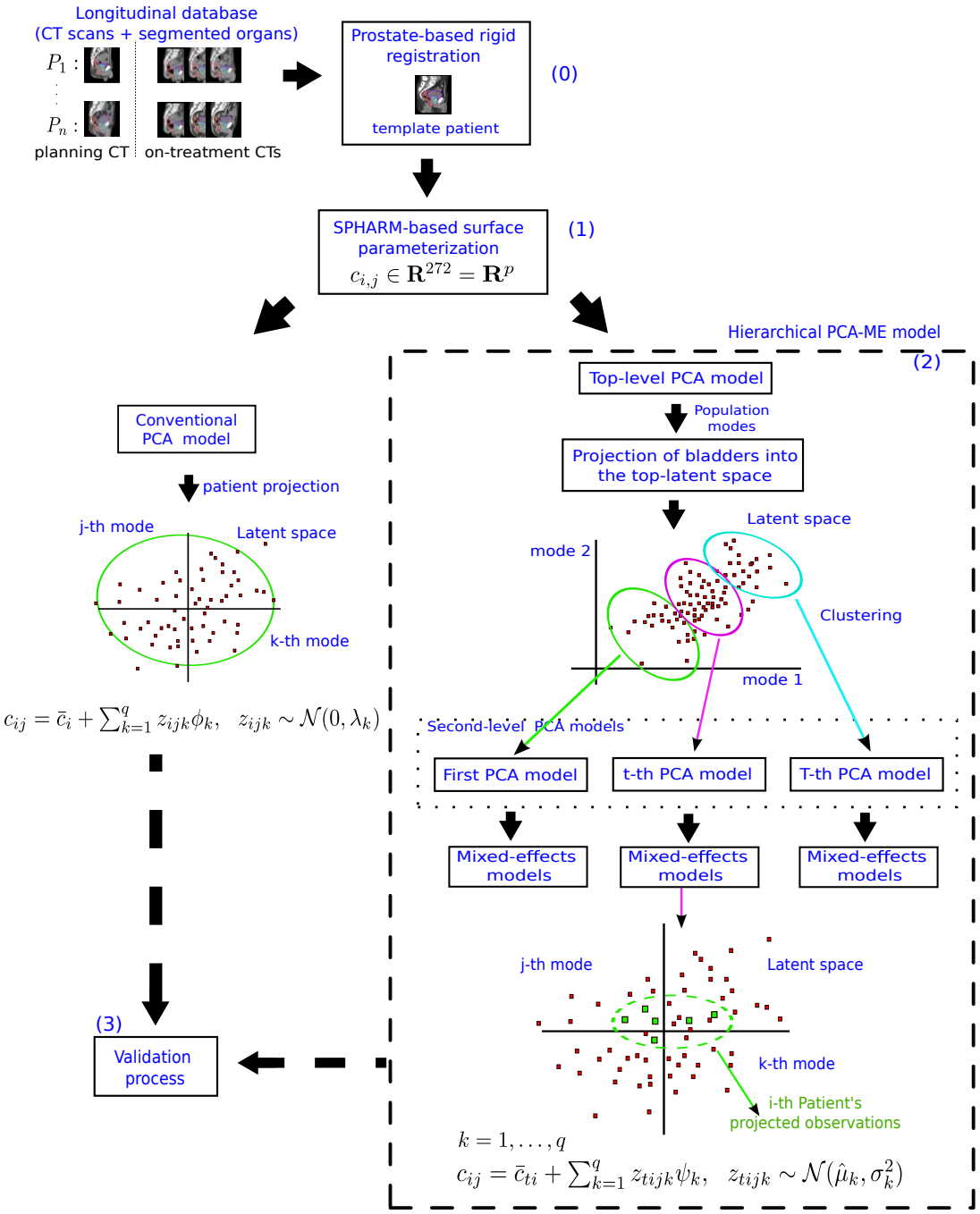

Figure 5.1: Workflow of the method used to train the hierarchical population-based model. 1) prostate-based registration, 2) parameterization of bladder surface using SPHARM coefficients, 3) hierarchical principal component analysis (PCA) followed by mixed effects models, 4) leave-one-out cross validation.

respectively. The column vectors of matrix $\mathbf{U}$ defined the directions of variability of the bladders called modes. Singular values of matrix $\mathbf{\Sigma}$ defined a significance ranking for the data variability represented by each mode, attesting $var(\varphi_1) = \sigma_1^2 \geq var(\varphi_2) = \sigma_2^2 \geq \cdots \geq var(\varphi_r) = \sigma_r^2$, where r was the rank of the data matrix $\mathbf{S}_{snapshot}$ and φ_i was the i-th left singular vector of matrix $\mathbf{U}$.

5.2.1.2 Projection and clustering of bladder into latent space

This step sought to represent each shape vector c_{ij} as an linear combination of the first three modes of the top-level model, as is described as follows:

$$c_{ij} \approx \hat{c}_{ij} = w_{ij1}\,\varphi_1 + w_{ij2}\,\varphi_2 + w_{ij3}\,\varphi_3 \tag{5.2}$$

where $w_{ij,\,k} = c_{ij}^T\,\varphi_k$ for $k = 1, 2, 3$. The first three modes φ_k defined a new coordinate system, henceforth called top-latent space, where each bladder c_{ij} was represented by the three new coordinates $(w_{ij1}, w_{ij2}, w_{ij3})$. We then sought to display the entire structure of the longitudinal database revealing the presence of clusters of bladders with similar shapes on the top-latent space using K-means algorithm. As in Chapter 3, we used well-defined regions of bladders with similar shapes to define the number $\mathcal{T}$ of clusters. As a result, mean bladder shape of well-defined regions were used as initial values for the K-means algorithm [114].

Let $w = (w_1, w_2, w_3)$ be the measure of geometric variation of an organ along a mode in the top-latent space. Considering the patient as the unit of observation state (subject), we used an index i, ranging from 1 to n, to differentiate among patients, and an index j to differentiate between observation times in a patient. The encoded longitudinal data was thus defined as follows:

$$\{w_{11}, \ldots, w_{1j_1}\}, \{w_{21}, \ldots, w_{2j_2}\}, \cdots, \{w_{n1}, \ldots, w_{nj_n}\} \tag{5.3}$$

Our goal was then to partition the data in $\mathcal{T}$ clusters. So, we firstly introduced a set of 3-dimensional vector m_t, where $t = 1, \ldots, \mathcal{T}$, in which m_t was the mean associated with the $t-th$ cluster (i.e. m_t represented the cluster center). Let $\pi_{tij} \in \{0, 1\}$ be also a binary indicator that described which of the $\mathcal{T}$ clusters the data point w_{ij} was assigned to, i.e. if the data point w_{ij} was assigned to cluster t, then $\pi_{tij} = 1$ and $\pi_{ijb} = 0$ for $b \neq t$. We then aimed to find the values of π_{tij} and m_t that minimized the following objective function:

$$J = \sum_{t=1}^{\mathcal{T}} \sum_{i=1}^{n} \sum_{j=1}^{j_n} \pi_{tij} \|w_{ij} - m_t\|^2 \tag{5.4}$$

This function was minimized following an iterative procedure, which is described as follows: firstly a set of initial values for m_t were proposed. Function J was then minimized with respect to π_{tij}, keeping m_t fixed. Subsequently, function J was minimized with respect to m_t, keeping π_{tij} fixed [114]. This two-step optimization, known as expectation-maximization (EM) algorithm, was then repeated until convergence.

Now consider first the optimization J with respect to π_{tij}, keeping m_t fixed. The objective function J was a linear function of π_{tij}, where the terms of the function J involving different ij were independent. As a result, each term $\pi_{tij}\|w_{ij} - m_t\|^2$ was optimized separately by choosing π_{tij} to be 1 for whichever value of t that gave the minimum value of $\|w_{ij} - m_t\|^2$. In other words, we assigned the ij-th data to the closest cluster center. This can thus be expressed as follows:

$$\pi_{tij} = \begin{cases} 1, \text{ if } t = \arg\min_b \|w_{ij} - m_b\|^2 = \arg\max_b w_{ij}^T m_b - \frac{\|m_b\|^2}{2} \\ 0, \text{ otherwise} \end{cases} \tag{5.5}$$

The equality between both arguments arg in Eq. 5.5 can be found in Appendix B. Consider then the optimization J with respect to m_t, keeping π_{tij} fixed. The objective function J was then a quadratic function of m_t, and it can be minimized by setting its derivative with respect to m_t to zero to obtain that:

$$m_t = \frac{\sum_{ij} \pi_{tij} w_{ij}}{\sum_{ij} \pi_{tij}} \tag{5.6}$$

namely that m_t was equal to the mean of the data points w_{ij} assigned to cluster t.

5.2.1.3 Second-level PCA

We subsequently selected the corresponding shape vectors $c_{tij} = w_{ij1}\,\varphi_1 + w_{ij2}\,\varphi_2 + w_{ij3}\,\varphi_3$ such that $w_{ij} = (w_{ij1}, w_{ij2}, w_{ij3}) \in \Omega_t$ with $t = 1, \ldots, \mathcal{T}$. For each cluster Ω_t, a second level PCA model was then derived from an empirical covariance matrix $\mathbf{C}_t$, as follows:

$$\begin{aligned} \mathbf{C}_t &= \frac{1}{n_t} \sum_{i=1}^{n_t} \frac{1}{j_{ti} - 1} \sum_{j=1}^{j_{ti}} (c_{tij} - \bar{c}_{ti})(c_{tij} - \bar{c}_{ti})^T \\ &= \frac{1}{n_t} \sum_{i=1}^{n_t} \frac{1}{j_{ti} - 1} \sum_{j=1}^{j_{ti}} d_{tij} d_{tij}^T = \mathbf{U}_t \mathbf{D}_t \mathbf{U}_t^T \end{aligned} \tag{5.7}$$

where $\bar{c}_{ti}$ was the average bladder shape of the i-th Patient at the t-th cluster. n_t and j_{t_i} were the number of patients and patient's observation in the t-th cluster, respectively. The vector $d_{tij} = c_{tij} - \bar{c}_{ti}$ described the difference between the observed bladder c_{kij} and patient mean bladder shape. Similarly, $\mathbf{U}_t$ was a matrix composed of eigenvectors ψ_{tk} of $\mathbf{C}_t$, and $\mathbf{D}_t$ was the diagonal matrix constructed from its corresponding eigenvalues λ_{tk}, i.e, $\mathbf{C}_t \psi_{tk} = \lambda_{tk} \psi_{tk}$. Eigenvectors ψ_{tk} thus defined the directions of geometric variability observed in the cluster Ω_t. The eigenvalues of matrix D also defined a significance ranking for the data variability represented by each mode, attesting $var(\psi_{t1}) = \lambda_{t1} \geq var(\psi_{t2}) = \lambda_{t2} \geq \cdots \geq var(\psi_{tn_t}) = \lambda_{tr_t}$, and showing that data variability was dominated by the first q_t modes with $q_t << r_t = n_t$ (r_t was the

rank of the matrix $\mathbf{C}_t$). As a result, each bladder shape of Ω_t was expressed as a linear combination of the first q_t modes, as follows:

$$c_{tij} = \bar{c}_{ti} + z_{tij1}\,\psi_{t1} + \cdots + z_{tijq_t}\,\psi_{tq_t} \tag{5.8}$$

where $z_{tijk} = d_{tij}^T\,\psi_{tk}$. According to theory of PCA, each coefficient z_{tijk} obeyed a Gaussian distribution with mean of zero and the corresponding eigenvalue as variance. The accumulated variability contained in the first q_t modes was determined as follows:

$$P_{q_t} = \frac{\sum_{k=1}^{q_t} \lambda_{tk}}{\sum_{k=1}^{r_t} \lambda_{tk}}, \qquad q_t = 1, \ldots, r_t \tag{5.9}$$

The corresponding population-based hierarchical PCA model is thus described as follows:

$$\begin{aligned} \text{Hierarchical Local PCA model} := \quad & c_{ij} = \sum_{t=1}^{\mathcal{T}} \pi_t\,\Theta_t, \quad \pi_t \in \{0,1\} \\ & \Theta_t = \bar{c}_{ti} + z_{tij\,1}\,\psi_{t1} + \cdots + z_{tij\,q_t}\,\psi_{tq_t} \\ & \pi_t = \begin{cases} 1, & \text{if } t = \arg\max_b w_{ij}^T\,m_b - \frac{\|m_b\|^2}{2} \\ 0, & \text{otherwise} \end{cases} \end{aligned} \tag{5.10}$$

In addition, we proposed an additional hierarchical model that used two second-level PCA models, if the bladder c_{ij} was almost at the same distance to two cluster centers. The corresponding population-based hierarchical PCA model is described as follows:

$$\begin{aligned} \text{Hierarchical mixed-Local PCA model} := \quad & c_{ij} = \sum_{t=1}^{\mathcal{T}} \pi_t\,\Theta_t, \\ & \Theta_t = \bar{c}_{ti} + z_{tij\,1}\,\psi_{t1} + \cdots + z_{tij\,q_t}\,\psi_{tq_t} \\ & \pi_t = \begin{cases} 1, & \text{if } \frac{w_{ij}^T\,m_t - \frac{\|m_t\|^2}{2}}{\max_b w_{ij}^T\,m_b - \frac{\|m_b\|^2}{2}} > \delta \\ 0, & \text{otherwise} \end{cases} \end{aligned} \tag{5.11}$$

where $\delta > 0$ is threshold for ratio between two distance. As a result, the bladder c_{ij} can be assigned to the two nearest clusters. Observe that both hierarchical PCA models shared the same top-level and second-level PCA models.

We evaluated the capability of the hierarchical PCA model to represent a typical bladder using only a few dominating modes. So, we performed leave-one out cross validation on the training database using a reconstruction error metric e. This means that one patient and his images were used as validation set, and the remaining patients were used to train the model. The error assessing the difference between the original and reconstructed motion-deformation error was defined as follows:

$$e_i = \frac{\| d_i - \hat{d}_i \|}{\| d_i \|} \tag{5.12}$$

where d_i and $\hat{d}_i$ were the i-th bladder motion-deformation vector and its approximation, respectively. If the reconstruction of c_i was exact, then e_i was equal to 0; otherwise, the value of e_i was between 0 and 1. The mean of the reconstruction error e_i in all the motion-deformation vectors was also calculated, i.e., $\mathcal{M} = (1/N) \cdot \sum_{i=1}^{N} e_i$, where e_i denoted the approximation error of an i-th motion-deformation vector d and N the number of the available images, either in the hierarchical PCA model or left-out patients.

We also defined error metrics in order to measure the quality of the K-means classifier in the left-out patients, as follows:

$$\text{Precision}(g) = 1 - \frac{1}{N} \sum_{i=1}^{N} 1_{g(c_i) \neq y_i} \tag{5.13a}$$

$$\text{Sensitivity}_t(g) = \frac{\sum_{m=1}^{n_t} 1_{g(c_i)=y_i}}{n_t}, \quad \text{for } t = 1, \ldots, \mathcal{T} \tag{5.13b}$$

$$\text{Specificity}_t(g) = \frac{\sum_{m=1}^{n_t} 1_{g(c_i) \neq y_i}}{N - n_t} \tag{5.13c}$$

where g denoted the classifier, c_i was an observed bladder in the left-out patients, y_i was respective class, and N the number of images in the training database. In addition, an conventional population PCA-based model was also used to compare the reconstruction performance of our proposed model. Such PCA model taken from Budiarto et al. (2011) is described as follows:

$$c = \bar{c}_i + \sum_{k=1}^{q} z_{ik}\, \phi_k, \tag{5.14}$$

$$\text{Local PCA model} := \; z_k \sim \mathcal{N}(0, \lambda_k) \quad \wedge \quad \bar{c}_i = \frac{1}{j_i} \sum_{j=1}^{j_i} c_{ij}$$

$$\begin{aligned} \mathbf{C}_{empirical} &= \frac{1}{n} \sum_{i=1}^{n} \frac{1}{j_i - 1} \sum_{j=1}^{j_i} (c_{ij} - \bar{c}_i)(c_{ij} - \bar{c}_i)^T \\ &= \frac{1}{n} \sum_{i=1}^{n} \frac{1}{j_i - 1} \sum_{j=1}^{j_i} d_{ij} d_{ij}^T\, \phi_k = \lambda_k\, \phi_k \end{aligned}$$

where n was the number of patients, j_i was the number of observations available for the i-th patient, and $\bar{c}_i$ the average shape of the i-th patient.

5.2.2 Linear mixed-effects models

As in fourth chapter, the longitudinal data was encoded in the second-level modes by projecting the observed motion-deformation vectors of the training database over each mode. A linear mixed-effects model was then fit to each mode aiming to characterize patient-specific variance from population.

Denoting the measure of motion/deformation of an organ along the k-th mode of the i-th Patient at the j-th observation and in the t-th cluster as z_{tijk}. The encoded longitudinal data was thus defined as follows:

$$\{z_{t11k}, \ldots, z_{t1j_1k}\}, \{z_{t21k}, \ldots, z_{t2j_2k}\}, \cdots, \{z_{tn1k}, \ldots, z_{tnj_nk}\}, \qquad k = 1, \ldots, q_t \quad (5.15)$$

with the linear mixed-effects model proposed for each mode described as follows:

$$\begin{gathered} z_{tijk} = \mu_{tk} + b_{tik} + \varepsilon_{tij\,k}, \qquad i = 1, \ldots, n,\ j = 1, \ldots, j_i, \\ b_{tik} \sim \mathcal{N}(0, \sigma^2_{tbk}),\ \epsilon_{tijk} \sim \mathcal{N}(0, \sigma^2_{tk}), \end{gathered} \quad (5.16)$$

where μ_{tk} was the mean projection along the k-th mode for the whole population in the t-th cluster. b_{tik} was also a random variable representing the deviation of the i-th patient mean from the population mean, and ε_{tijk} was a random variable representing the deviation for j-th projection of the i-th patient from the i-th patient mean in the t-th cluster. In addition, variances σ^2_{tbk} and σ^2_{tk} denote inter and intra-patient variability, respectively. The second-level PCA models with mixed-effects were thus described as follows:

$$\begin{gathered} \Theta_t = \bar{c}_{ti} + W_t z_t \\ c = \begin{bmatrix} c_0^0 & c_1^0 & \cdots & c_L^{-L} \end{bmatrix},\ W_t = \begin{bmatrix} \varphi_{t1} & \cdots & \varphi_{tq} \end{bmatrix},\ z_t = \begin{bmatrix} z_{t1} & \cdots & z_{tq} \end{bmatrix} \end{gathered} \quad (5.17)$$

where $\bar{c}_{ti}$ was the patient mean shape, $z_{tk} \sim \mathcal{N}(\mu_{tk}, \sigma^2_{tbk} + \sigma^2_{tk})$, for $k = 1, \ldots, q_t$.

5.2.3 Out-of-sample problem

We also sought to predict a likely motion-deformation region of the bladder for a new patient P_l using only his planning CT information. As shown in Fig. 5.2, the first step was also to spatially normalize the out-of-sample patient P_l to match the template patient; secondly, the SPHARM representation of his delineated bladder $c_{l,0}$ was obtained and classified in the top-latent space; and thirdly, second-level Local-PCA models were adapted to the new patient by estimating his patient-specific mean and variance $\hat{\mu}_{tlk}$ and $\hat{\sigma}_{tljk}$.

Consider the adaptation of each second-level PCA models to the new patient P_l. We sought to estimate the following linear model:

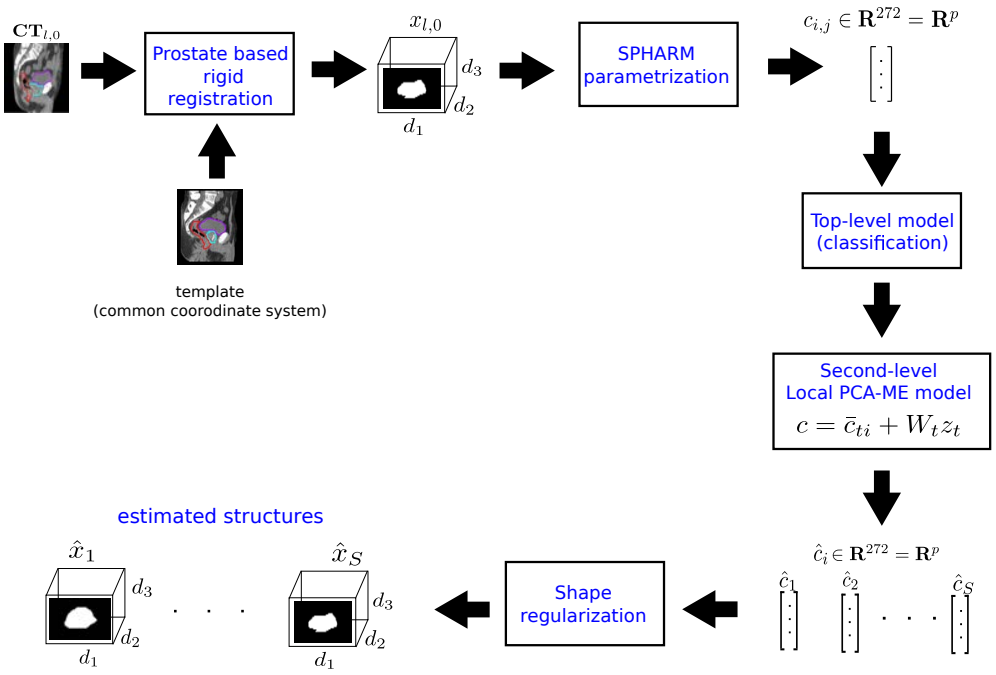

Figure 5.2: Workflow to estimate new structures based on the planning CT for a new patient for the hierarchical-based PCA model.

$$z_{tljk} = \mu_{tk} + b_{tlk} + \epsilon_{tljk} \sim \mathcal{N}(\hat{\mu}_{tlk}, \hat{\sigma}^2_{tlk}), \qquad j = 1, \ldots, j_{tl},\ k = 1, \ldots, q_t \tag{5.18}$$

A shrinkage estimator of $\hat{\mu}_{tlk} = \mu_{tk} + b_{tlk}$ was then given by:

$$\hat{\mu}_{tlk} = \mu_{tk} + \zeta_{tk}\,(\mu_{tlk} - \mu_{tk}), \quad \zeta_{tk} = \frac{j_{tl}}{j_{tl} + \sigma^2_{tk}/\sigma^2_{tbk}}, \quad k = 1, \ldots, q_t \tag{5.19}$$

where μ_{tlk} was the mean of the l-th patient at the k-th mode, and j_{tl} was the number of patient's observations. Term ζ_{tk} was known as the credibility factor. Similarly, the variance of the prediction error $\hat{\sigma}^2_{tlk} = var(\epsilon_{tlk})$ was given by:

$$\hat{\sigma}^2_{tlk} = \left(1 - \frac{\sigma^2_{tbk}}{\sigma^2_{tk} + \sigma^2_{tbk}}\right) \frac{n_t}{\sigma^2_{tk} + \sigma^2_{tbk}} \left(1 - \frac{\sigma^2_{tbk}}{\sigma^2_{tk} + \sigma^2_{tbk}}\right) - \frac{(\sigma^2_{tbk})^2}{\sigma^2_{tk} + \sigma^2_{tbk}} + \sigma^2_{tk} + \sigma^2_{tbk} \tag{5.20}$$

In our study, $\bar{c}_{tl} = c_{tl,0}$, $\mu_l = W_t^T(\bar{c}_{tl} - c_{tl,0}) = z_{tl} = 0$ and $j_{tl} = 1$ due to we only had the information obtained from the planning CT. In this way, probable structures of the bladder during treatment were thus inferred after sampling S times the Normal distributed vector z_t. Subsequently, each sample of z_t was mapped to a vector c in the spherical harmonic space using matrix W_t. Then, binary images representing probable

bladder configurations were obtained from the parameterized surfaces that were coded in vectors c. Following this, an estimation of the motion/deformation region was calculated by the ratio between the number of times that a voxel was occupied by the bladder and the S generated samples.

5.2.4 Evaluation of prediction performance

The models' prediction performance was also evaluated by following leave-one-out cross validation in the training database and also using the independent database. We thus estimated probability maps with each model and compared with the observed PM in both databases. Seven PMs were thus calculated for each out-sample patient: one PM obtained from the patient's observed available images, labeled PM_{obs}; one PM estimated by using the local PCA model, labeled $PM_{Local\,PCA}$; one PM estimated by means of the local PCA model with mixed-effects, labeled $PM_{Local\,PCA-ME}$; one PM estimated by means of the Hierarchical-Local PCA model, labeled $PM_{HR\,PCA}$; one PM estimated by means of the Hierarchical-Local PCA model with mixed-effects models, labeled $PM_{HR\,PCA-ME}$; one PM estimated by means of the Hierarchical Mixed-Local PCA model, labeled $PM_{HR-ML\,PCA}$; and one PM estimated by means of the Hierarchical Mixed-Local PCA model with mixed-effects models, labeled $PM_{HR-ML\,PCA-ME}$.

Estimated PMs were derived for each model and patient, as follows: firstly, 40 bladder structures were generated using the bladder observed at the planning CT (i.e. $S = 40$, see Fig. 5.2); and secondly, a distribution of 15 PMs were derived from the 40 estimated structures, where each PM was obtained from a sub-set of estimated bladders (without replacement) whose cardinality was equal to the number of available CT/CBCTs. We also used the mutual information-based metric to assess the similarity between two PMs X and Y (see Eq. 4.14).

5.3 Results

5.3.1 Hierarchical PCA representation

The number of columns of the data matrix $\mathbf{S}_{snapshot}$ varied from 151 to 154. The first, second and third mode contributed, on average, 52.91%, 4.75%, and 3.34% of the variability, respectively. Fig. 5.6 presents sagittal views of the first three modes of the top-level PCA model over the population mean bladder. The first mode was also associated with bladder volume, i.e it describes the direction of maximum volume variability observed in the database. Meanwhile, the second and third mode describe directions that dilate and shrink regions in the bladder. For example, the second mode indicated dilation/contraction in the upper-ventral and medial-dorsal regions of the bladder whereas the third mode indicated dilation/contraction in the inferior and medial-ventral regions.

Fig. 5.4a depicts the projection of all the bladder instances in the space spanned by the first two and three modes. In this reduced space, it can be observed several well-defined regions or clusters of bladder shapes. For example, oval-like bladders are found in the rectangular region $(-120, -60) \times (-10, 10) \times (-5, 10)$. As in Chapter 3, it can

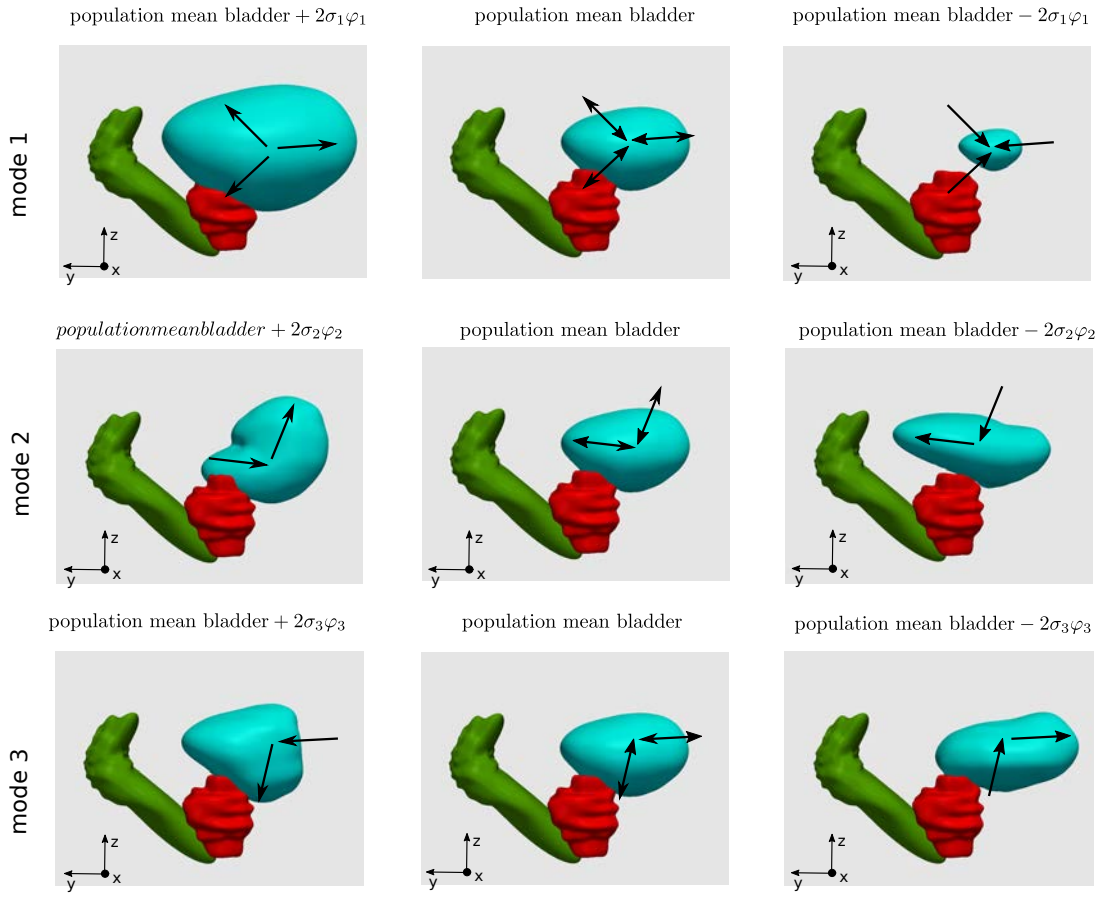

Figure 5.3: 3D sagittal views of the first three top-level modes applied on the population mean bladder (center column). The left and right columns correspond to geometric variations along the respective mode φ_i, defined as *population mean bladder* $\pm 2\sigma_i\varphi_i$, where σ_i^2 is the mode variance. The prostate (red color) and rectum (green color) of the template patient were also included as spatial reference).

be also observed that each patient had a motion/deformation region (see Patient 6 and 7). As the first mode had the largest variance contribution, we used this mode to define the number of clusters and the groups of patients to initialize the cluster centers for the K-means algorithm. We then proposed two and three clusters in the top-latent space defining two hierarchical models, as follows: a first clustering made by those patients with $c_{ij}^T\varphi_k < -100$ and $c_{ij}^T\varphi_k \geq -100$; and a second clustering made by those patients with $c_{ij}^T\varphi_k < -120$, $-120 \leq c_{ij}^T\varphi_k < -80$, and $c_{ij}^T\varphi_k \geq -80$. Figs. 5.4b and 5.4c show the K-means clustering results in the top-latent space. Figs. 5.4d and 5.4e also depict the accumulated variability of the eigenvalues for these second-level Local PCA models. Fixing a threshold of 0.95%, we obtained a conventional Local PCA model with 16 modes, on average. Similarly, we obtained 8 and 17 modes for the hierarchical PCA model with Local PCA model in the second-level, and 7, 13 and 15 modes for the

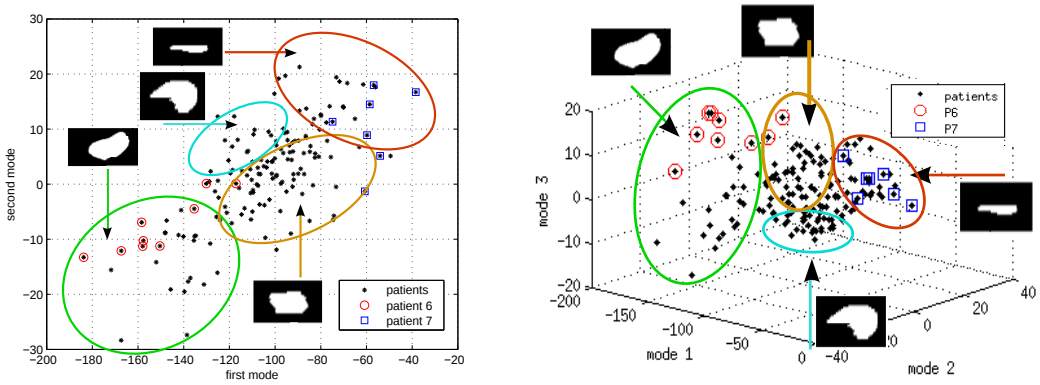

(a) Regions of bladders with similar shape

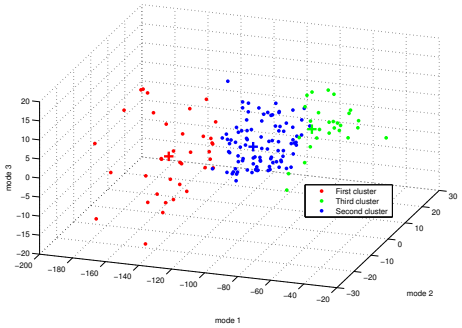

(b) Top latent-space partitioned in three clusters

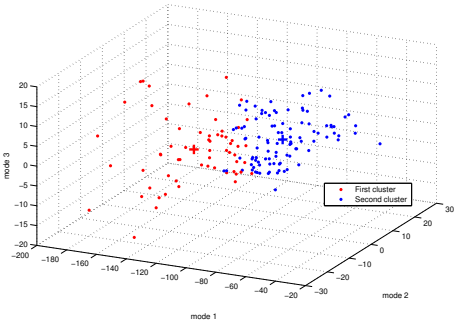

(c) Top latent-space partitioned in two clusters

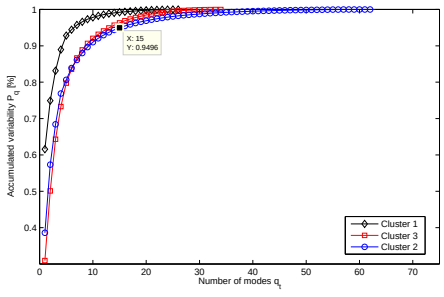

(d) P_{q_t} for two PCA models in the second-level

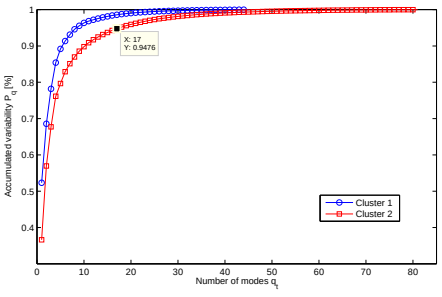

(e) P_{q_t} for three PCA models in the second-level

Figure 5.4: a) Scatterplot of the patients projected in the space spanned by the first two and three modes (Black points). b)-c) Color circles and squares correspond to the vectors of two individuals. b) Top-latent space partitioned in two and three clusters using k-means algorithm. Cluster centers are marked using larger + symbol. d)-e) Accumulated mode variance P_{q_t} using PCA in each cluster of the second-level.

hierarchical PCA model with three Local PCA model in the second-level.

Fig. 5.5 and 5.6 present sagittal views of the first three second-level modes over the

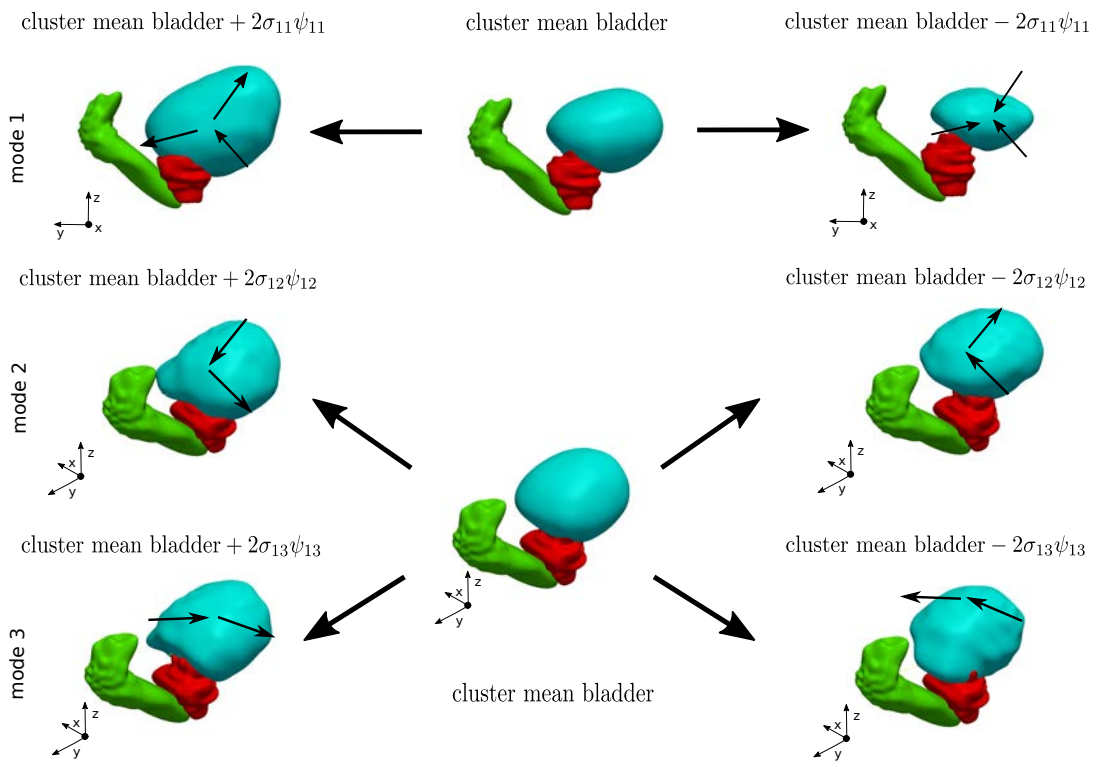

Figure 5.5: 3D sagittal views of the first three motion/deformation modes for the first cluster applied on the mean bladder (center column), when the top-latent space is divided into two clusters. The left and right columns correspond to geometric variations along the respective mode ψ_{1i}, defined as *cluster mean bladder* $\pm 2\sigma_{1i}\psi_{1i}$ is the mode variance. The prostate (red color) and rectum (green color) of the template patient were also included as spatial reference.

mean bladder of each cluster for the hierarchical model with two Local PCA models in the second-level. As in previous results, the first mode also describes the direction of maximum volume variability. Meanwhile, the second and third mode also describe directions that dilate and shrink regions in the bladder. For example, the second and third mode in the first cluster indicated dilation/contraction in the medial-ventral and lateral regions of the bladder whereas in the second cluster indicated dilation/contraction in the medial-anterior and lateral regions. Fig. 5.7 presents the mean approximation error $\mathcal{M}$ in both the training and left-out patients for the three PCA models. Table 5.1 also presents the error metrics of the classifier for both hierarchical models. The precision metric was 0.025 and 0.0313 for the hierarchical model with two and three second-level clusters, respectively.

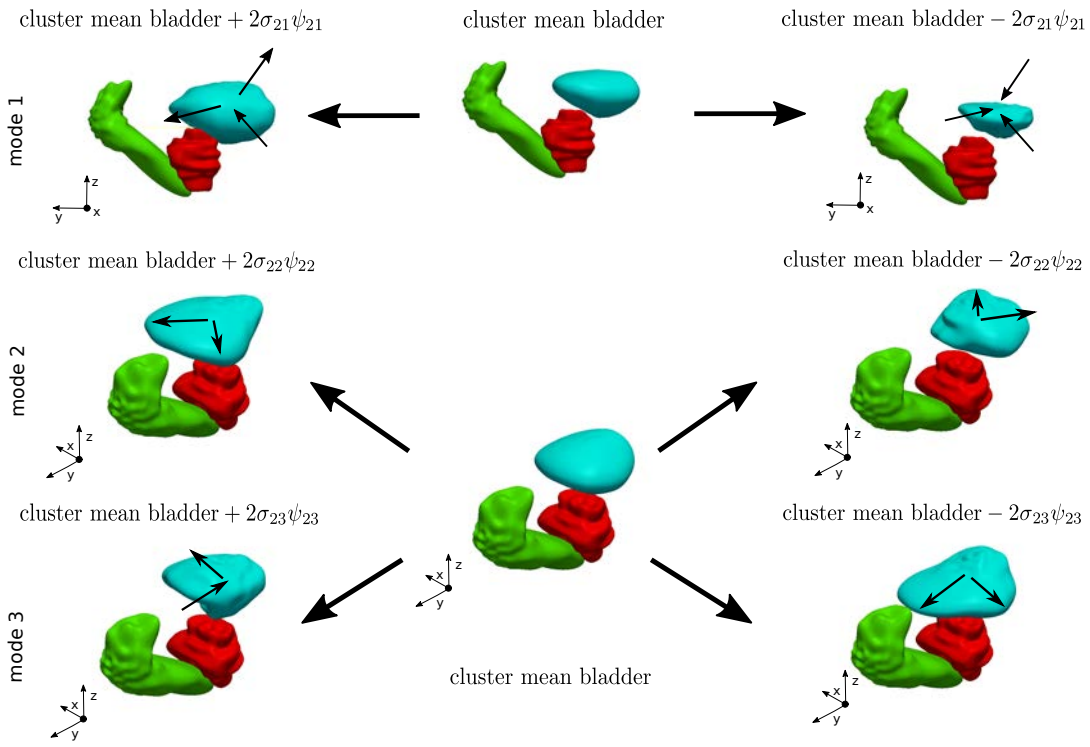

Figure 5.6: 3D sagittal views of the first three motion/deformation modes for the first cluster applied on the mean bladder (center column), when the top-latent space is divided into two clusters. The left and right columns correspond to geometric variations along the respective mode ψ_{2i}, defined as *cluster mean bladder* $\pm 2\sigma_{2i}\psi_{2i}$ is the mode variance. The prostate (red color) and rectum (green color) of the template patient were also included as spatial reference.

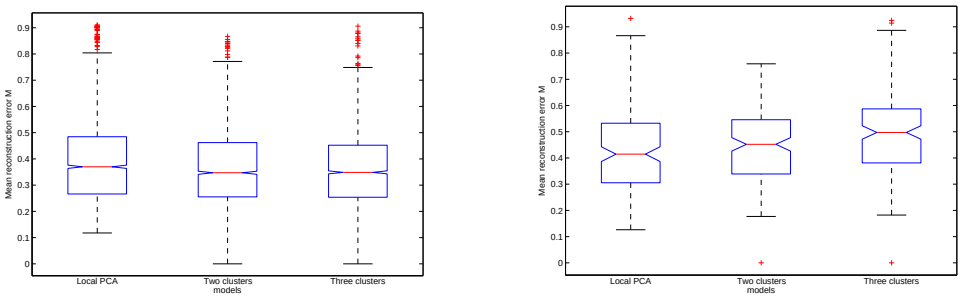

(a) Training database (b) Validation database

Figure 5.7: Mean approximation error $\mathcal{M}$ of the Hierarchical PCA models compared to the conventional Local PCA model in the training and left-out patients

Table 5.1: Error metrics of the classifier for both hierarchical models

Cluster	Hierarchical model Two clusters		Hierarchical model Three clusters	
	Sensitivity(g)	Specificity(g)	Sensitivity(g)	Specificity(g)
Cluster 1	0.95	0.99	0.94	1
Cluster 2	0.99	0.95	0.95	1
Cluster 3	–	–	1	0.94

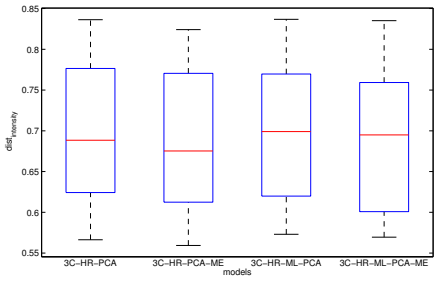

(a) Two clusters in the second-level

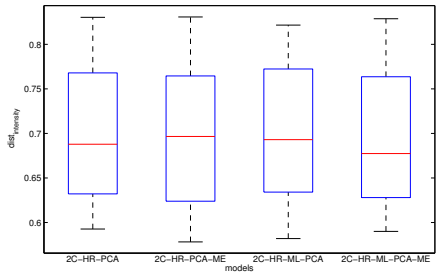

(b) Three clusters in the second-level

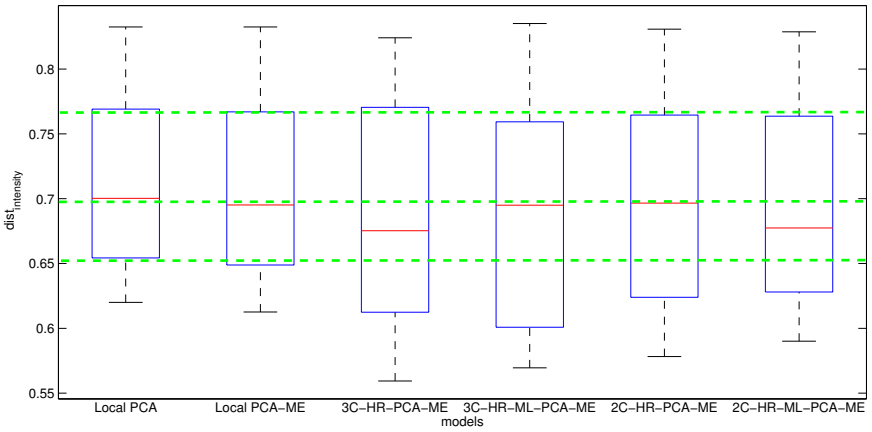

(c) Local models vs Hierarchical models

Figure 5.8: Average $dist_{intensity}$ values of observed and estimated PMs for patients in the training database using Hierarchical PCA models.

5.3.2 Evaluation of performance prediction with groundwork models

Defining a threshold $\delta = 0.95$, Fig. 5.8 and Fig. 5.9 depict the averages of the metric $dist_{intensity}$ for patients in both databases. On average, the Local PCA model obtained the highest measures of dissimilarity in both databases while the hierarchical model

obtained the lowest measures. Similarly, Figs. 5.10 and 5.11 also show the averages of the metric Accuracy for patients in both databases. On average, the Local PCA model also obtained the lowest accuracy in both databases while the hierarchical models obtained the highest. In both metrics, we obtained that the HR-ML PCA-ME models with two and three clusters obtained the best performances. For each patient and metric, a significant test was also made between the HR-ML PCA-ME and Local PCA models using the Wilcoxon rank sum test for all 15 $dist_{intensity}$ and Accuracy values. Table 5.2 shows the number of patients that had significant difference in both databases. We also obtained three variance distributions by deriving the variance of the 15 values for each metric and patient in both databases. Table 5.3 presents the p-values of the significant tests that were made between these variance distributions of the Local PCA and HR-ML PCA-ME models using the Wilcoxon rank sum test.

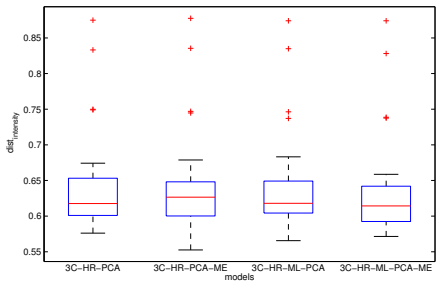

(a) Two clusters in the second-level

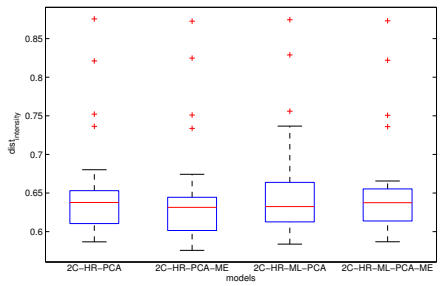

(b) Three clusters in the second-level

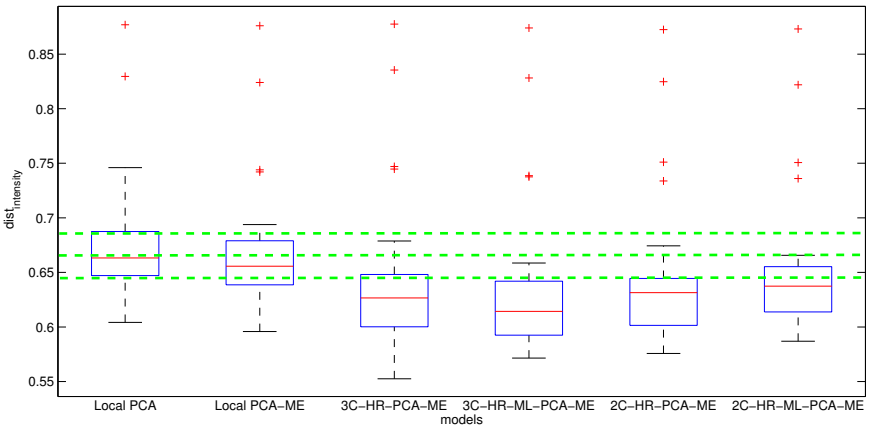

(c) Local models vs Hierarchical models

Figure 5.9: Average $dist_{intensity}$ values of observed and estimated PMs for patients in the validation databases using Hierarchical PCA models.

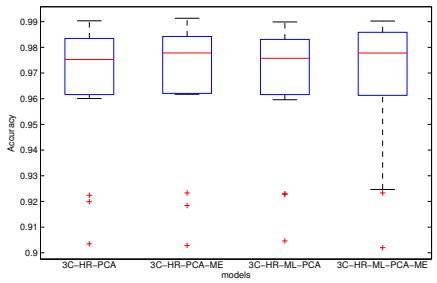

(a) Two clusters in the second-level

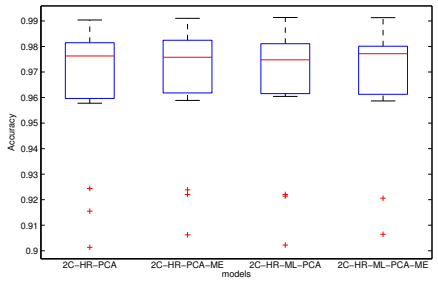

(b) Three clusters in the second-level

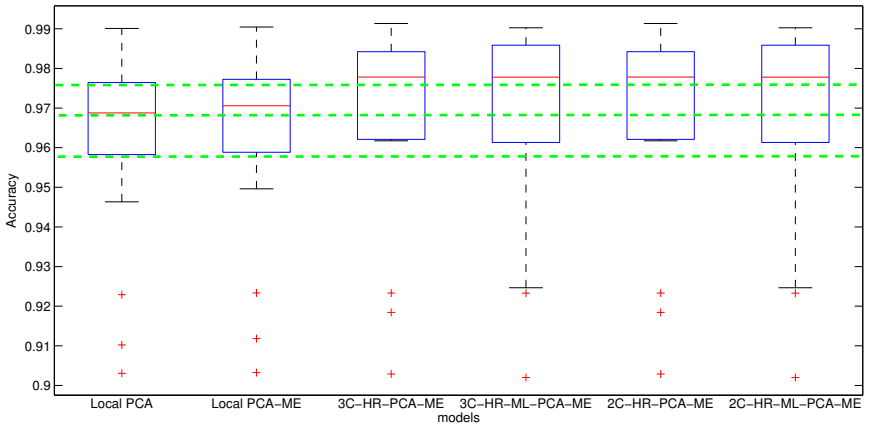

(c) Local models vs Hierarchical models

Figure 5.10: Average $dist_{intensity}$ values of observed and estimated PMs for patients in the training database using Hierarchical PCA models.

5.4 Discussion

We have hereby proposed a new methodology for predicting uncertainties produced by inter-fraction shape variations of the bladder in prostate cancer radiotherapy via population analysis. We firstly used a visualization algorithm to obtain hierarchical modes that enables us to reveal the latent structure of a longitudinal database of bladders. The idea was then to properly characterize the patient-specific modes from the population. We secondly fit a ME model along each mode to the longitudinal data defined by the projections of the motion/deformation vectors observed in the training database. In addition, bladder shapes and motion/deformation regions were characterized in the top-latent space while bladders with similar shape were then characterized in the lower-level subspaces. We proposed reconstruction error metrics to assess the capability of the modes to represent a typical bladder following leave-one-cross validation. Bladder motion and deformation regions were also computed using solely the planning CT scan, and

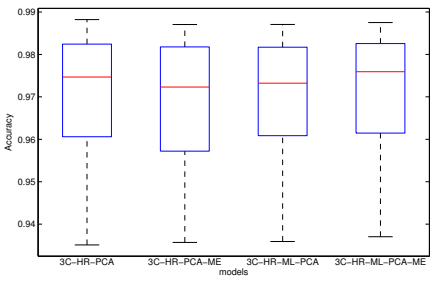

(a) Two clusters in the second-level

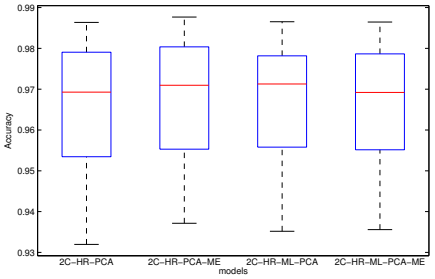

(b) Three clusters in the second-level

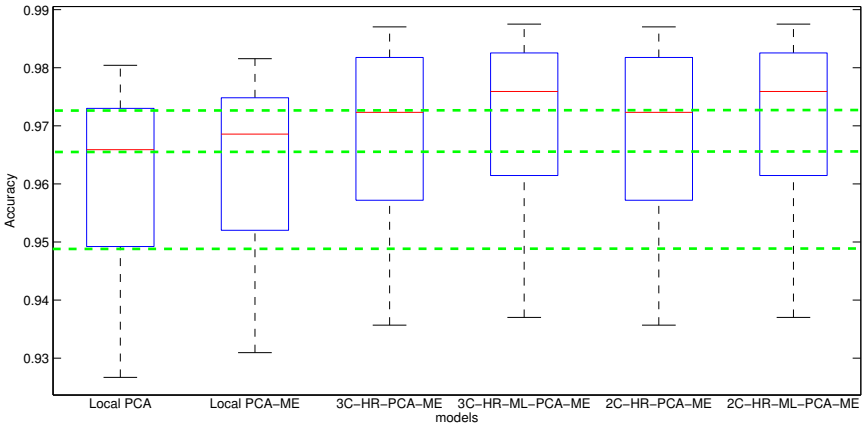

(c) Local models vs Hierarchical models

Figure 5.11: Average *Accuracy* values of observed and estimated PMs for patients in the validation databases using Hierarchical PCA models.

we used leave-one-cross validation on the training database and an external database to validate the model. We used a conventional population PCA model in order to compare the performance of the hierarchical models. Motion/deformation regions were also characterized by means of PMs and metrics were used to measure similarities between observed and estimated PMs.

From the algorithm proposed by Bishop et al [106], we have obtained a set of fundamental modes that were hierarchical nested to separate intra- and inter-patient directions of geometric variability observed in the database. As in Fig. 3.3 and 4.5, the first modes also described the directions of maximum volume variability that were observed in each level and cluster. Meanwhile, further modes also described directions of geometric variability that dilated or shrunk certain regions of the bladders. From Figs. 4.5, 5.5 and 5.6, it can be observed that the number of geometrical directions described by the first modes in the hierarchical models has been increased compared to the Local PCA model. We therefore conclude that hierarchically nesting PCA models enable us

Table 5.2: Number of patients exhibiting significance difference using the Wilcoxon rank sum test in both databases between the Local PCA and HR-ML PCA-ME models.

Database	Local PCA model vs 2C-HR-ML PCA-ME $dist_{intensity}$/Accuracy	Local PCA model vs 3C-HR-ML PCA-ME $dist_{intensity}$/Accuracy
Training	14/17	13/16
Validation	19/24	17/26

Table 5.3: p-values of the Wilcoxon rank sum tests for the variance distributions between PCA models in both databases the Local PCA and HR-ML PCA-ME models.

Database	Local PCA model vs 2C-HR-ML PCA-ME $dist_{intensity}$/Accuracy	Local PCA model vs 3C-HR-ML PCA-ME $dist_{intensity}$/Accuracy
Training	0.19/0.13	$0.0239/6 \cdot 10^{-4}$
Validation	0.99/0.017	$0.75/5 \cdot 10^{-4}$

to increase the degree of freedom of the overall motion-deformation model. However, we consider that hierarchical PCA models introduce a higher number of parameters, increasing the model complexity. For instance, the hierarchical models required more modes than the conventional model to describe the same threshold of accumulated variability.

As in Chapter 2, we characterized bladder shapes and patients' motion/deformation regions in the top-latent space. Although a voxel-based representation was used in Chapter 2, we obtained that the distribution of the patients and bladders with similar shapes was preserved in both latent spaces. We thereby conclude that the characterization of the bladder space remains invariant from orthogonal basis (modes). We in turn conclude that SPHARM reduces the number of variables required to represent the bladder surface while preserving shape information. From Fig. 5.4a, we also consider that the motion/deformation region of a patient in the latent space is mainly described by the bladder volume. We have thus proposed to use the first mode to define groups of patients that were used as initial centers for the clusters.

From Fig. 5.7, we obtained that the mean reconstruction error of the Local PCA model was higher than the hierarchical models in the training database. Meanwhile, the hierarchical model with two clusters only outperformed the reconstruction error in the validation database. As opposed in Rios et al in [115], we consider that this outcome was produced as some patients with a single observation in a cluster could not be considered to derive the empirical covariance matrix to train the Local PCA models in the second-level (see Eq. 5.2). As a result, this resulted in a loss of information that reflected in a lower description for bladders not included in the training set compared to the conventional model. As a future work, for those patients with a single observation, it could be used a prior patient-specific covariance matrix. For instance, an estimation of the patient's mean bladder shape can be obtained either using observations from all the patients or only those patients that are closer. It is worth mentioning that in hierarchical models with Global PCA models hierarchically nested as derived in Rios et al in [115], all the bladder observations of a cluster were used to derive the covariance matrix. Concerning the clustering method, we have used a conventional algorithm like K-means as our main gaol in this study was to prove that the hierarchical methodology outperformed conventional PCA models to predict motion/deformation regions. However, we also used used Gaussian mixture models, and we obtained similar results of classification. Future studies could then focus on testing different clustering methods (e.g Fuzzy C-means) in the top-level latent space in order to study the effect of the clustering algorithm in the reconstruction error. Concerning this issue, we consider that the reconstruction error may also be reduced by adding a constraint that avoids that observations of the patients were divided into two clusters, i.e, by achieving a longitudinal classification of the patients.

As it was previously established, PCA-based shape models achieve a good performance for organs whose shape variations can be captured by a reasonable number of modes [108]. From Fig. 5.9 to 5.11, we consider that conventional PCA models are not be suitable to properly capture the latent structure of longitudinal databases with highly varying soft-tissue as they require a large number of modes. For instance, in our study we required 8 modes to describe 90% of the cumulative variance while 40 modes to generate an population PCA model. As consequence, we conclude that the first 8 modes of the conventional model did not accomplish to properly describe the main modes for all the patients. Instead the proposed hierarchical methodology has enabled us to better describe the patient-specific modes by increasing the number of geometric directions observed in the first modes compared to conventional model. As observed in 5.9 to 5.11, the best predictions were achieved by those models designed with hierarchical modes and mixed-effects models, accomplishing to reduce the uncertainties in the estimation of the probable motion/deformation region. For example, comparing the performance of the hierarchical models with mixed-effects and Local PCA model, we obtained more patients with significance differences in both metrics and databases; moreover, we accomplished to significantly reduce the variance of the estimated motion/deformation region regarding the Local PCA model in the training and validation databases (see Table 5.3). Finally, we consider that this methodology enables us to increase the degrees of freedom outperforming the characterization of organ shape variations in a wide

range of applications including segmentation [60, 108], modeling of organ motion and deformation [53–55, 57], margin evaluation [51, 55], delivered dose estimation [50], and the design of robust treatment plans [43, 50, 52, 116], among others.

5.5 Conclusion

We proposed hierarchical population-based PCA model to characterize and predict shape variations of the bladder between fractions in prostate cancer radiotherapy. This hierarchical structure enables us to increase the degree of freedom of the model and to better reveal the latent structure of the longitudinal database than the conventional PCA model. In comparison with previous studies, our proposed hierarchical model with mixed-effects accomplished to significantly reduce the uncertainties in the estimation of the region where the bladder will likely moves and deforms. We also demonstrated that using hierarchically nesting modes, it was possible to separate the patient-specific directions of geometric variability from the population reducing uncertainties in the estimation of the motion/deformation region. The potential applications of this model include organ segmentation, margin evaluation, delivered dose estimation, toxicity prediction, and the design of robust treatment plans, among others. Future studies should be focused to study the relationship among bladder motion and deformation, delivered dose and urinary symptoms in prostate cancer radiotherapy.

Part III

Quantification of dose uncertainties for the bladder using PCA-based models

Chapter 6

Quantification of dose uncertainties for the bladder in prostate cancer radiotherapy based on PCA-based models

The radiotherapy goal is to deliver a dose distribution that enables a high dose to the tumor and preserves at most neighboring healthy organs. This dose distribution is usually obtained based on the organ delineations made in the planning CT. However, organs move and deform between treatment fractions leading to geometries that are not exactly to those delineated in the planning CT. As a result, non-trivial deviations may arise between the planning and delivered dose to the tumor and OARs, reducing the treatment quality. For example, such deviations may lead to highly irradiated OARs and increase the patient's probability of developing side-effects. Although new technologies such as IGRT have enabled us to determine the actual position and shape of organs, the acquisition of patient-specific data during treatment is time-intensive, costly and thereby not always feasible in clinical practice. Methods that enable us to simulate or monitor the actual delivered dose are therefore vital to assess or replan treatments during treatment course.

PCA has been used as virtual tool to evaluate dosimetric uncertainties produced by organ motion and deformation [50, 116]. In this context, PCA was used to calculate mean and variance of the accumulated dose via Monte Carlo simulations or integration over the probability distribution. However, some questions have not been addressed yet: firstly, how many modes are required for dosimetric treatment course simulations?; secondly, how many modes are required for an adequate estimation of patient-specific dosimetric uncertainties?. As accumulated dose only varies at the points that move in or out of the beams [111], it is expected that a limited number of modes would have a significant effect on dosimetric uncertainties produced by organ motion and deformation between fractions.

This chapter presents PCA models as a tool to estimate dosimetric uncertainties

for the bladder produced by inter-fraction motion and deformation. We used three patients treated for prostate cancer radiotherapy that underwent a planning CT as well as 35-39 on-treatment CBCTs for each. For each patient, we trained an individual PCA models using the bladder samples available from the on-treatment CT/CBCTs. Our objective was to determine the number of modes required for an adequate estimation of the patient-specific dosimetric variability. We then obtained three accumulated doses: one reference accumulated dose that was calculated via deformable image registration (DIR); one accumulated dose that was computed by sampling the multivariate Gaussian distribution of the PCA model followed by a Monte Carlo approach; and a accumulated dose computed by integrating the planning dose over the Gaussian probability distribution of the PCA model. We finally compared the three accumulated doses using iterative procedure to determine our objective.

The chapter is organized as follows. Section 6.1 describes the database used in this study. Section 6.2 presents the methodology used to quantify dose uncertainties via Monte Carlo simulation and integration over the probability distribution. Section 6.3 subsequently presents the results and comparison to groundwork methods. Lastly, section 6.4 discusses the experimental findings, with a conclusion in section 6.5 in addition to final considerations and future work.

6.1 Data

We used the three patients having a planning CT and on-treatment CBCTs of the validation database described in Chapter 2. The resolution of the CT scans were $512 \times 512 \times 80$, with a voxel size of $1mm \times 1\ mm \times 3\ mm$.

6.2 Methods

Fig. 6.1 describes the methodology performed to quantify dose uncertainties of the bladder using PCA models. Firstly, we derived an individual PCA model for each patient in the database using the observations obtained from the on-treatment CT/CBCTS; secondly, we calculated a reference accumulated dose using the patient's on-treatment CBCTs via DIR; thirdly, we estimated an accumulated dose by integrating the planning dose over the Gaussian probability distribution of the PCA model; fourthly, we estimated an accumulated dose by simulating treatment courses via a Monte Carlo approach. Finally, we compared the planning dose with the three accumulated doses, and we calculated average voxel doses, local dose variability and dose-volume histogram uncertainties.

6.2.1 Principal component analysis

This step was aimed to derive an individual PCA model for each patient from the on-treatment CT/CBCTS, following the same work of Shön et al. [57]. For each patient, an empirical covariance matrix $\mathbf{C}$ of motion-deformation vectors was thus defined in order

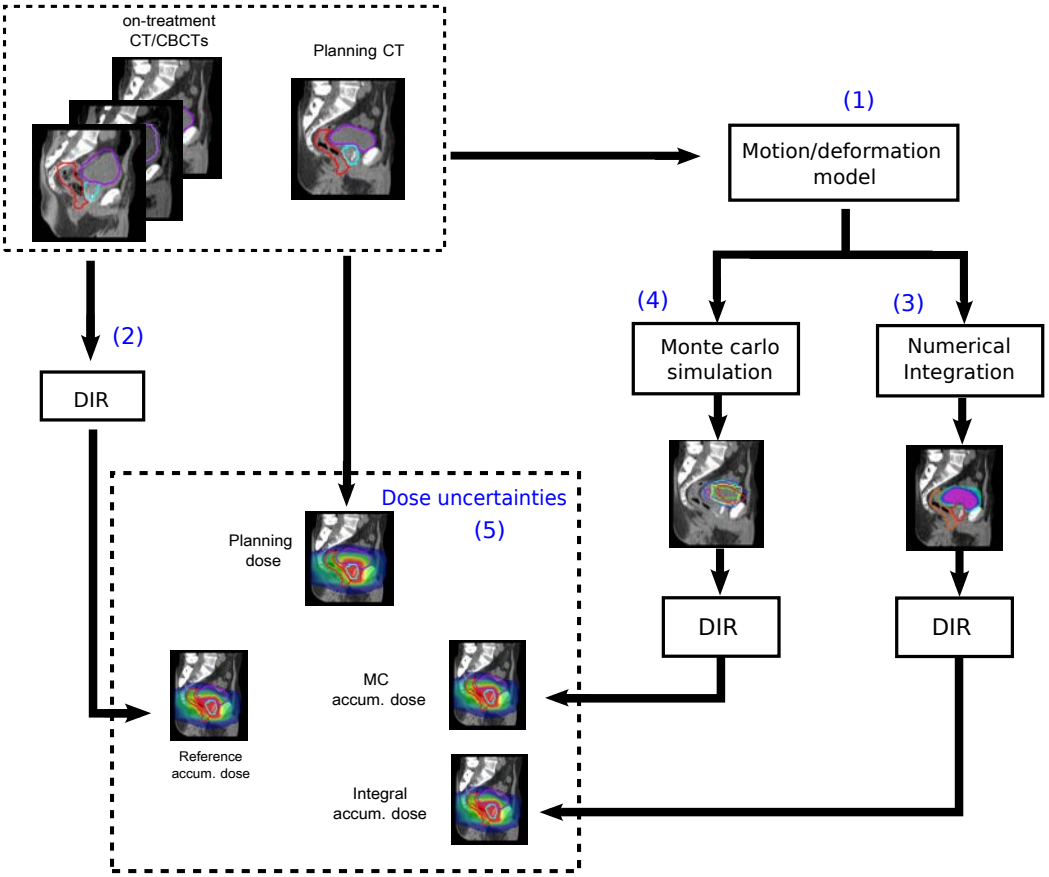

Figure 6.1: Workflow of the method used to quantify dose uncertainties of the bladder. 1) principal component analysis (PCA) reduction, 2) reference accumulated dose via deformable image registration (DIR), 3) accumulated dose via dose integration, 4) accumulated dose via Monte Carlo simulation (MC), 5) comparison of the planning dose and the three accumulated doses.

to calculate the directions of maximum variability by using matrix diagonalization. Here, a motion-deformation vector defined the difference between the observed bladder and patient mean bladder. Thus, denoting the observed bladder at the j-th CT as c_j, the empirical covariance matrix $\mathbf{C}$ was defined as follows:

$$\begin{aligned}\mathbf{C}_{empirical} &= \frac{1}{N-1}\sum_{j=1}^{N}(c_j-\bar{c})(c_j-\bar{c})^T \\ &= \frac{1}{N-1}\sum_{j=1}^{N} d_j d_j^T = \mathbf{UDU}^T\end{aligned} \tag{6.1}$$

where $d_j = c_j - \bar{c}$, N was the number of observations available for the patient, and $\bar{c}$ the average shape of the patient. Similarly, $\mathbf{U}$ was a matrix composed of eigenvectors φ_k of $\mathbf{C}_{empirical}$, and $\mathbf{D}$ was the diagonal matrix constructed from its corresponding eigenvalues λ_k, i.e, $\mathbf{C}_{empirical}\varphi_k = \lambda_k\varphi_k$. Eigenvectors φ_k defined the directions of geometric variability of the bladder, called modes. As a result, each bladder in the spherical harmonic space was expressed as a linear combination of the modes, as follows:

$$c_j = \bar{c} + z_{j\,1}\,\varphi_1 + \cdots + z_{j\,r}\,\varphi_r \tag{6.2}$$

where r was the rank of covariance matrix $\mathbf{C}_{empirical}$, and equal to the number of available images for the patient. Each coefficient $z_{jk} = d_j^T\,\varphi_k$ denoted a geometric variation of the bladder c_j along the mode φ_k. Modes $\{\varphi_k\}_k$ defined a new coordinate system, where each vector d_{ij} was represented by new r coordinates $z_{j\,1}, \ldots, z_{j\,r}$. The eigenvalues of matrix D defined a significance ranking for the data variability represented by each mode, attesting $var(\varphi_1) = \lambda_1 \geq var(\varphi_2) = \lambda_2 \geq \cdots \geq var(\varphi_r) = \lambda_r$, and showing that data variability was dominated by the first q modes with $q << r$. The accumulated variability contained in the first q modes was determined as follows:

$$P_q = \frac{\sum_{k=1}^{q} \lambda_k}{\sum_{k=1}^{r} \lambda_k}, \qquad q = 1, \ldots, r \tag{6.3}$$

According to theory of PCA, each coefficient z_k obeyed a Gaussian distribution with mean of zero and the corresponding eigenvalue λ_k as variance. The corresponding patient-specific PCA model is thus described as follows:

$$\text{Patient-specific PCA model} := \quad c = \bar{c} + z_{j\,1}\,\varphi_1 + \cdots + z_{j\,q}\,\varphi_q \tag{6.4a}$$

$$f_z(z_1, \ldots, z_q) = \prod_{k=1}^{q} \frac{1}{\sqrt{2\pi\lambda_k}} exp\Big(\frac{1}{2} z_k^2/\lambda_k\Big) \tag{6.4b}$$

where f_z was a multivariate Gaussian probability density function. Bladder contours with their probability of occurrence can be generated byâ sampling vector z. â

As in Chapter 4, we also described regions of motion/deformation in terms of 3D probability maps (PM) that express the probability of a voxel being occupied by the bladder during treatment. Estimated PMs were derived for each patient by generating S bladder structures from Eq. 6.4. Two PMs were thus calculated for each patient: one PM estimated by means of the Patient-specific PCA model, labeled PM_{indPCA}; and one PM obtained from the patient's available images, labeled PM_{obs}.

6.2.2 Estimation of the reference accumulated dose distribution

As in [117,118], we computed for each patient an accumulated dose distribution, called the reference accumulated dose $d_{cum,ref}$, using four steps: firstly, the dose at fraction was computed; secondly, a geometrical transformation U was computed between the

planning CT scan and each CBCT scan using DIR; thirdly, the fraction dose was deformed using the deformation field U; and fourthly, the deformed doses were summed to obtain the accumulated dose $d_{cum,ref}$. The fractional dose distribution D_s was assessed for each CBCT by translating the planned dose distribution $D_{planned}$ according to the transformation T resulting from the alignment of the prostate barycenters, since we assumed invariant dose distributions between the planning and fractions. Meanwhile, the DIR was not applied to the original grayscale images but to images resulting from the manual delineations of the bladder on the CT and CBCT images. For this purpose, for both the CT and CBCT images, distance maps were computed, representing for each voxel the signed squared Euclidean distance from the organ surface. Distance maps obtained from CT and CBCT delineations were then registered with a variant of Demons algorithm providing the estimated deformation field U, further details can be found in [117, 118]. The fraction dose D_s was finally deformed using the deformation field U and resampled in the planning CT with a trilinear interpolation. As a result, the daily cumulative dose distribution $d_{cum,ref}$ can be calculated as follows:

$$D_{cum,ref} = \sum_{s=1}^{N_{frac}} D_s(x_{s,obs}) \approx \frac{1}{N_{frac}} \sum_{s=1}^{N_{frac}} D_{planned}(x_{s,obs}) \tag{6.5}$$

where $D_s \approx D_{planned}/N_{frac}$, $x_{s,obs}$ was the delineated bladder observed at the s-th CBCT scan (i.e. at the s-th dose fraction), and N_{frac} was the number of treatment fractions. For each patient, the $D_{cum,ref}$ was calculated from the available on-treatment CBCTs. As a result, N_{frac} was equal to the number of patient's CBCTs. We denoted $DVH_{cum,ref}$ as the DVH obtained from the reference accumulated dose, and $DVH_{obs,s}$ as the DVH of the dose fraction D_s applied to the observed bladder structure $x_{s,obs}$.

6.2.3 Mean and variance accumulated dose via integration

According to Eqs. 6.4, the delivered dose is as well a random variable as the bladder randomly moves and deforms following a Gaussian probability distribution. As in [116], the density function of the dose D can then be estimated by integrating the planning dose over the motion and deformation probability density function f_z (see Eq. 6.4b). The first two moments can thus be computed as follows:

$$\mu_{cum,int} = \int_z D(x(z)) f_z(z) d_z \tag{6.6a}$$

$$= \int_{z_1} \cdots \int_{z_q} D(x(z)) \prod_{k=1}^{q} \frac{1}{\sqrt{2\pi\lambda_k}} exp\Big(\frac{1}{2} z_k^2/\lambda_k\Big) d_{z_1} \cdots d_{z_q}$$

$$\sigma_{cum,int} = \int_z (\, D(x(z)) - \mu_{cum,int}\,)^2 f_z(z) d_z \tag{6.7a}$$

$$= \int_z D^2(x(z)) f_z(z) d_z - \mu^2_{cum,int} \tag{6.7b}$$

where $\mu_{cum,int}$ and $\sigma_{cum,int}$ denoted the mean and variance of the accumulated dose, respectively. Defining $\mu_{cum,int,k}$ and $\sigma_{cum,int,k}$ as the mean and variance of the accumulated dose restricted to the first k modes, respectively, we proposed the following iterative procedure to determine the number of modes required to quantify patient-specific dose uncertainties:

Step 1 To calculate $\mu_{cum,int,1}$ and $\sigma_{cum,int,1}$

Step 2 To calculate $\mu_{cum,int,2}$ and $\sigma_{cum,int,2}$

Step 3 To calculate $dist_{int,2}(\mu_{cum,int,2}, \mu_{cum,int,1}) = \frac{\|\mu_{cum,int,2} - \mu_{cum,int,1}\|}{\|\mu_{cum,int,2}\|}$

Step 4 To repeat step 2 and 3 for $k = 3, \ldots, q$, if $dist_{int,k} > \varepsilon$

where ε defined a tolerance value. For each value of k, the integrals of Eqs. 6.6 and 6.7 were solved numerically using the composite Simpson's Rule to calculate $\mu_{cum,MC,k}$ and $\sigma_{cum,MC,k}$. Fig. 6.2 illustrates a Pareto curve that shows the quantification of dose uncertainties as a function of the number of modes in the PCA model. It is worth mentioning that computational complexity of the numerical solution increases as function of the number of modes. Appendix C provides numerical details for solving these multi-dimensional integrals. We denoted the DVH of the mean accumulated dose distribution $\mu_{cum,int,k}$ as $DVH_{\mu_{cum,int,k}}$. In addition, we denoted $DVH_{int,k,s}$ as the DVH of the s-th dose fraction applied to the s-th estimated bladder structure $x_{int,k,s}$ in the numerical solution of $\mu_{cum,int,k}$.

6.2.4 Mean and variance accumulated dose via Monte Carlo simulation

As in [50], single treatment courses can be simulated by drawing random vectors from the probability function f_z (Eqs. 6.4), and their corresponding accumulated dose obtained using DIR. As a result, we also propose to use a Monte Carlo approach to estimate the first two moments of the dose density probability function. Monte Carlo approach is described as follows.

Let $x_s = \{v_{i_1,i_2,i_3}\}_{i_1,i_2,i_3} \in \mathbb{R}^{d_1 \times d_2 \times d_3}$ and

$$D_s(x_s) = (D_s(v_{1,1,1}), D_s(v_{1,1,2}), \ldots, D_s(v_{d_1,d_2,d_3})) \in \mathbb{R}^{d_1 \times d_2 \times d_3} \tag{6.8}$$

be the bladder obtained by shape regularization from the parameterized bladder c_s, and the dose fraction associated to the bladder structure x_s, respectively. $D_s(v_{i_1,i_2,i_3})$

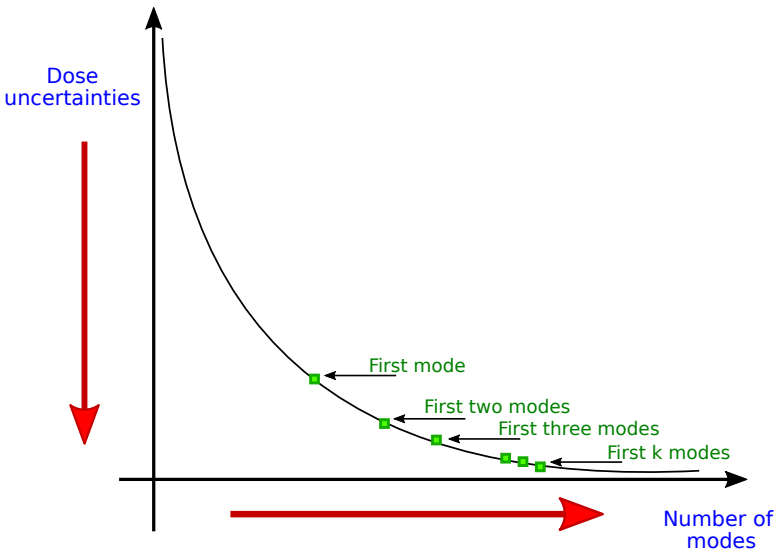

Figure 6.2: Pareto curve used to determine the number of modes required to properly estimate the patient-specific dose uncertainties.

then represented the dose at the voxel v_{i_1,i_2,i_3} of the bladder structure x_s. Similarly, $D_{planned}(x_{planned})$ denoted the dose associated to the bladder contour $x_{planned}$ at the treatment planning CT.

Generating N_{frac} random bladder structures $\{x_{s,est}\}_{s=1}^{N_{frac}}$ from Eq. 6.4, a treatment course can then be simulated and its corresponding accumulated dose computed as follows:

$$d_{cum,MC} = \sum_{s=1}^{N_{frac}} D_s(x_{s,est}) \approx \frac{1}{N_{frac}} \sum_{s=1}^{N_{frac}} D_0(x_{s,est}) \tag{6.9}$$

where $D_s \approx D_{planned}/N_{frac}$ was the dose fraction applied to the estimated bladder structure $x_{s,est}$. Considering $d_{cum,MC}$ as a random variable, a Monte Carlo approach was performed for each patient in order to obtain realizations of single-treatment courses, as follows: firstly, we drew S random vectors of the PCA scores in Matlab from Eq. 6.4b; secondly, we mapped these vectors to SPHARM coordinates using the orthogonal transformation obtained from Eq. 6.4a; thirdly, a set of S binary images representing probable bladder contours were obtained from the parameterized surfaces that were coded in SPHARM vectors (this set was denoted as $\Delta = \{x_{s,est}\}_{s=1}^{S}$); finally, a distribution of $\mathcal{N}$ accumulated doses $\{d_{cum,MC,m}\}_{m=1}^{\mathcal{N}}$ were derived using Eq. 6.9 by simulating treatment courses with N_{frac} bladder structures taken (without replacement) from the Δ set. Each accumulated dose $d_{cum,MC,m}$ was calculated by applying the DIR process to $x_{planned}$ and $x_{s,est}$ contours. Distance maps were also computed, and they were then registered with a variant of Demons algorithm providing the estimated deformation fields.

From the distribution of accumulated doses $\{d_{cum,MC,m}\}_{m=1}^{\mathcal{N}}$, we obtained the mean and variance accumulated doses as follows:

$$\mu_{cum,MC} = \frac{1}{\mathcal{N}} \sum_{m=1}^{\mathcal{N}} d_{cum,MC,m} \tag{6.10a}$$

$$\sigma_{cum,MC} = \frac{1}{\mathcal{N}-1} \sum_{m=1}^{\mathcal{N}} (d_{cum,MC,m} - \mu_{cum,MC})^2 \tag{6.10b}$$

We also computed the DVH of the expected mean accumulated dose distribution $\mu_{cum,MC}$, denoted as $DVH_{cum,MC}$; as well as, the DVH of each simulated accumulated dose $d_{cum,MC,m}$, denoted as $DVH_{cum,MC,m}$. We also denoted $DVH_{MC,s}$ as the DVH of the dose fraction D_s applied to the estimated bladder structure $x_{s,est}$.

6.2.4.1 Dose confidence region for single fractions

From the probability density function f_z in Eq. 6.4b, it was possible to obtain contours of bladder structures with equal probability mass. Contours are useful as they provide confidence regions that are analogous to the confidence intervals for the univariate distribution [119]. Contours were defined for those vectors z such that:

$$(z-\mu)^T \mathbf{D}^{-1}(z-\mu) = \theta^2 = \chi_q^2(\alpha) \tag{6.11}$$

where μ was the mean of z, $\mathbf{D} = \mathrm{diag}(\lambda_1, \ldots, \lambda_q)$ was the diagonal matrix made from eigenvalues of the covariance matrix, and θ was derived from the Chi-Squared distribution χ_q^2 with q degrees of freedom. The value of α provided the confidence region (CR) containing $1-\alpha$ of the probability mass of the probability density function f_z. These contours defined hyper-ellipsoids in the latent space spanned by the first k modes, whose axes were in the direction of the eigenvectors φ_k while the lengths of the axes were proportional to the square root of the eigenvalues $\theta\sqrt{\lambda_k}$, as it is described as follows:

$$\begin{aligned} (z-\mu)^T \mathbf{D}^{-1}(z-\mu) &= \theta^2 = \chi_q^2(\alpha) \\ (\beta_1 e_1 + \cdots + \beta_q e_q)^T \,\mathrm{diag}(\lambda_1^{-1}, \ldots, \lambda_q^{-1})(\beta_1 e_1 + \cdots + \beta_q e_q) &= \theta^2 = \chi_q^2(\alpha) \\ \frac{\beta_1^2}{\lambda_1} + \cdots + \frac{\beta_q^2}{\lambda_q} &= \theta^2 = \chi_q^2(\alpha) \end{aligned} \tag{6.12}$$

where $z - \mu = \sum_{k=1}^{q} \beta_k e_k$, and the vectors e_k were the canonical basis of the latent space. The coefficients β_k thus represented the coordinates of $z-\mu$ in the latent space.

Bladders structures with 95% of probability to fall can thereby be parameterized by the hyper-ellipsoid derived from Eq. 6.11 with $\theta^2 = \chi_q^2(0.05)$. Boundaries of this

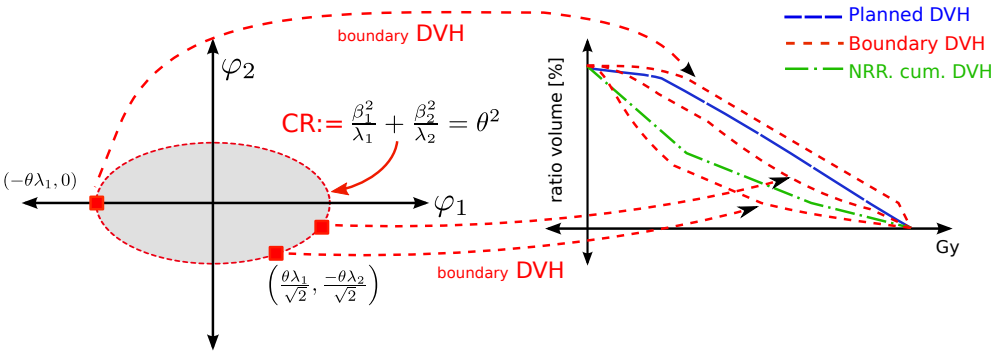

Figure 6.3: Visualization of the dose confidence region for single fractions in the space spanned by first two modes.

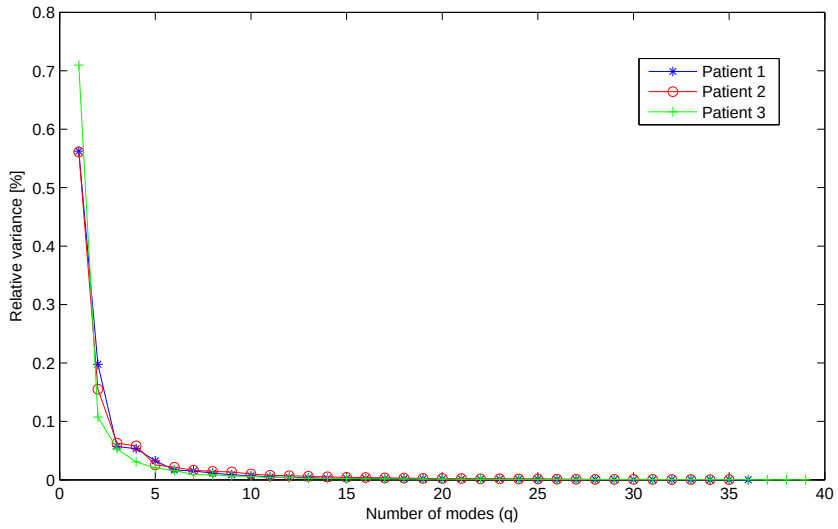

Figure 6.4: Relative mode variances obtained for the three patients (relative values: sum of all eigenvalues normalized to 100%).

confidence region then provided the uncertainty region of the fraction doses with 95% of probability to be delivered on accounting for geometric variations of the bladder during treatment. We hereby denoted $D_{Boundary,q} = D(x(z_{Boundary,q}))$ as the dose vector associated to the bladder structure obtained by the vector $z_{Boundary,q} = \sum_{k=1}^{q} \beta_k e_k$ and coefficients $\beta_1, \ldots, \beta_q$ holding Eq. 6.11. We also denoted $DVH_{Boundary,q,s}$ as the DVH of the boundary dose $D_{Boundary,q,s}$.

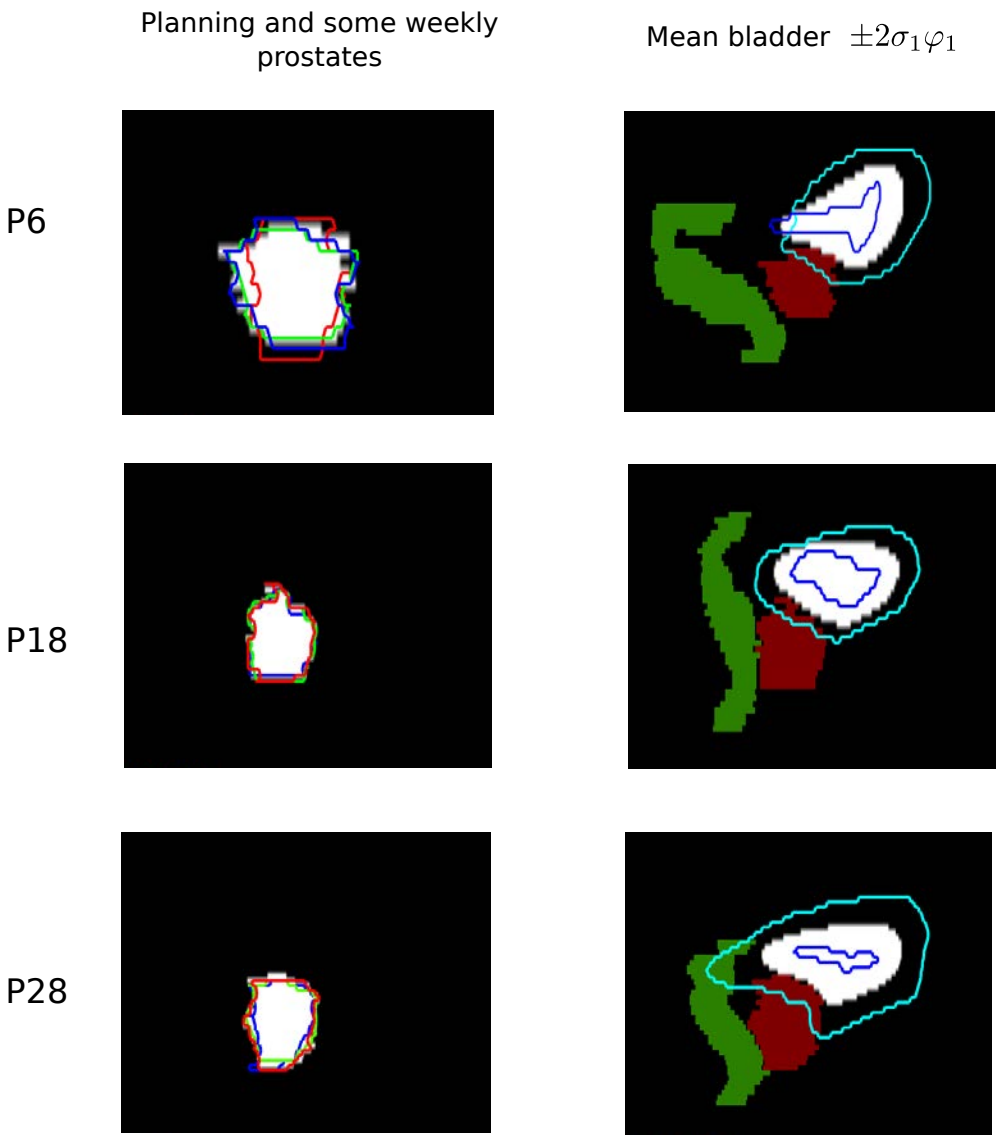

Figure 6.5: Intra-patient analysis for patients with on-treatment CBCTs. Left column depicts 3D sagittal views of the segmented prostate (white) at the planning CT with two observations (color contours) during treatment. Right columns shows 3D sagittal views of geometric variations (blue and cyan) along the first mode applied on the mean bladder (white), where σ_1^2 is the mode variance. The prostate (red) and rectum (green) of the patient were also included as spatial reference.

6.3 Results

Fig. 6.4 provides the eigenvalue spectrum for all the three patients. For Patient 1 and 2 having $N_{frac} = 36$ and $N_{frac} = 35$, the first mode contributed 0.56% of the

Table 6.1: Mean and standard deviation of the Dice Scores (DS) obtained following DIR for each bladder and estimated bladder structure.

Patient	Obs. bladders in the CBCTs	Est. bladders for MC simulation	Est.bladders for dose integration	Est. bladders for CR
Patient 1	0.97 ± 0.0064	0.96 ± 0.0031	0.96 ± 0.0011	0.96 ± 0.0037
Patient 2	0.97 ± 0.0001	0.97 ± 0.0016	0.97 ± 0.0030	0.97 ± 0.0021
Patient 3	0.98 ± 0.0001	0.98 ± 0.0011	0.97 ± 0.0052	0.98 ± 0.0022

variability while the first eight and 11 modes described 95% of the cumulative variance, respectively. Meanwhile, for Patient 3 having $N_{frac} = 39$, the first mode contributed 0.71% of the variability while the first seven modes described 95% of the cumulative variance. Fig. 6.5 provides 3D sagittal views of the first mode for each patient, where Patient 1 is denoted as P6, Patient 2 as P18 and Patient 3 as P28. As is observed from Fig. 6.5, the first mode describes the direction of maximum volume variability observed in the patient images.

For each patient, we calculated the reference accumulated dose together with its respective $DVHcum, ref$. Figs. 6.7a to 6.9a show the reference accumulated DVHs. Table 6.1 provides the mean and standard deviation of the Dice Scores (DS) obtained following DIR for each delineated bladder in the CBCTs. Similarly, we generated $S = 80$ bladder structures based on the above PCA models with $P_q = 95\%$. According to Eq. 6.4, the coefficients z_q were sampled from the multivariate Gaussian distribution aiming to estimate probable bladder geometries during treatment. Fig. 6.6 shows the observed and estimated PMs that were obtained for each patient. Table 6.1 also provides the mean and standard deviation of the Dice Scores (DS) obtained following DIR for each estimated bladder structure. We then simulated $\mathcal{N} = 100$ treatment courses using Eq. 6.8, where N_{frac} estimated bladder structures were taken without replacement from the bladder set Δ. Fig. 6.7a, 6.8a and 6.9a show the accumulated DVHs of 100 simulated treatment courses together with the average of these DVHs ($DVH_{cum,MC}$).

Fig. 6.10 provides 3D sagittal views of the variance dose $\sigma_{cum,MC}$ for each patient. Fig. 6.7b, 6.8b and 6.9b also show the DVH uncertainties resulting from MC simulation. These figures depict the variability of the dose fractions delivered to each delineated bladder on the patient's CBCTs as well as to each estimated bladder from the MC simulation (i.e. the set of bladder Δ). Dose fractions were rescaled to the total dose for easier visual comparison.

We also sought to determine the number of modes that are required to quantify patient-specific dose uncertainties. For each patient we calculated the mean and variance dose via integration of the planned dose over the Gaussian distribution of the first mode, the first two modes and the first three modes (see numerical details in Appendix C). We then used 10 subintervals along the z_1-axis to calculate $\mu_{cum,int,1}$ while 8 subintervals along the z_1-, z_2- and z_3-axes to calculate $\mu_{cum,int,2}$ and $\mu_{cum,int,3}$. As a result, a mesh of 11, 81 and 729 bladder geometries were generated to calculate $\mu_{cum,int,1}$, $\mu_{cum,int,2}$ and

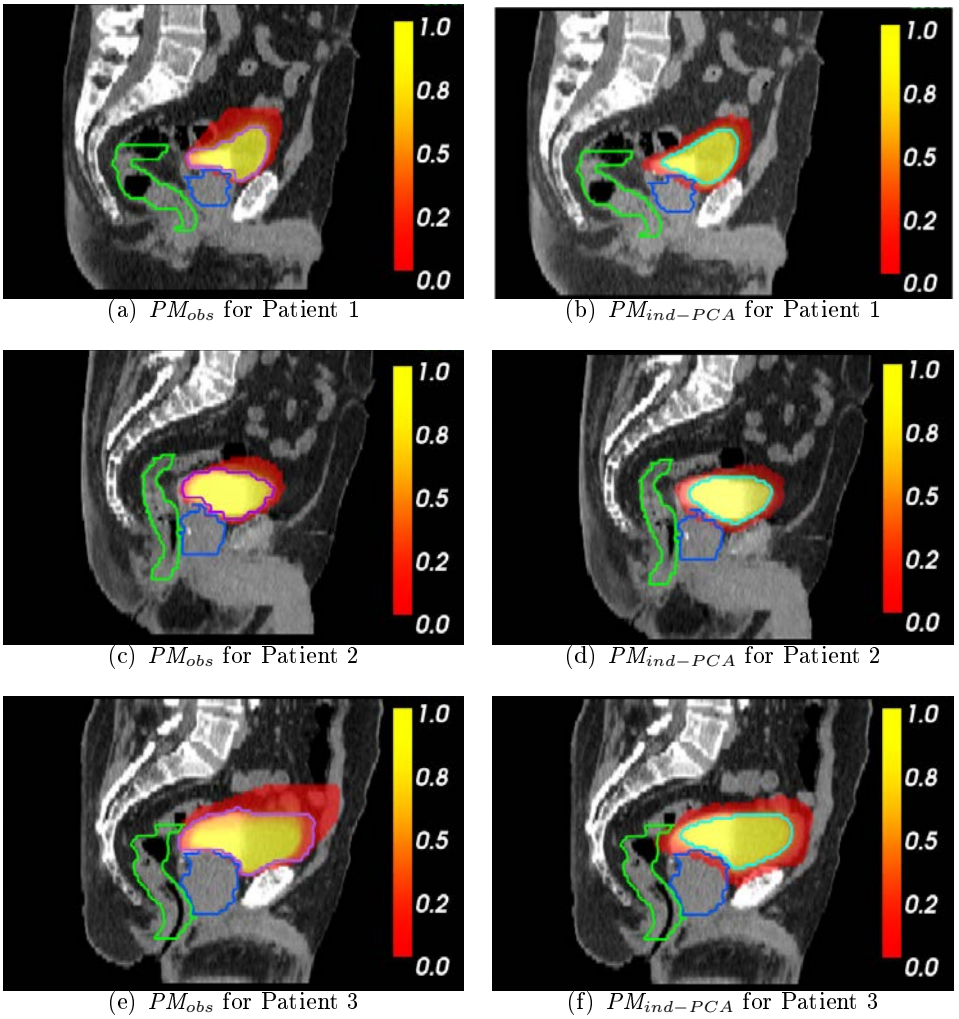

(a) PM_{obs} for Patient 1 (b) $PM_{ind-PCA}$ for Patient 1

(c) PM_{obs} for Patient 2 (d) $PM_{ind-PCA}$ for Patient 2

(e) PM_{obs} for Patient 3 (f) $PM_{ind-PCA}$ for Patient 3

Figure 6.6: 3D sagittal views of PMs obtained for each patient. Segmented prostate (blue), bladder (purple) and rectum (green) at the planning CT scan are overlaid. Patient's mean bladder (cyan) is also depicted.

$\mu_{cum,int,3}$, respectively. Table 6.2, 6.3 and 6.4 provide the values of the metric $dist_{int,k}$ for each integral for all the three patients. Besides, Fig. 6.7c, 6.8c and 6.9c provide the single-fraction DVHs of each bladder geometry generated from the mesh used to calculate $\mu_{cum,int,3}$. These figures also depict DVHs for some bladder structures from the CR (ellipsoid) generated with the first three modes. This ellipsoid corresponded to the contour of 95% of probability to fall defined by $\chi^2_3(0.05) = 7.92$.

Fig. 6.11a shows the DVH differences between the reference and accumulated doses obtained via DIR and MC simulation. Meanwhile, Fig. 6.11b show the DVH differences between the accumulated $DVH_{cum,int.3}$ obtained with dose integration over the first three modes and the mean accumulated $DVH_{cum,MC}$ obtained via MC simulation.

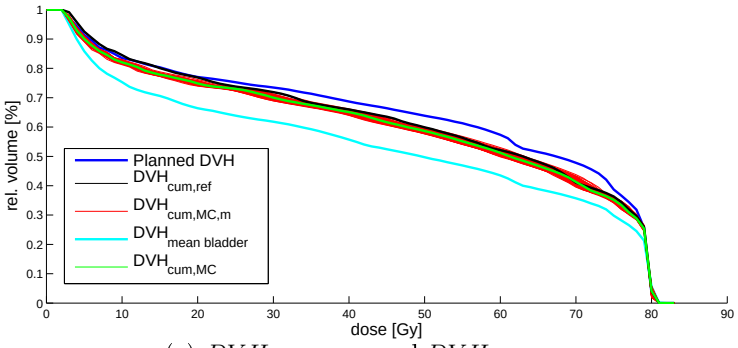

(a) $DVH_{cum,MC,m}$ and $DVH_{cum,MC}$

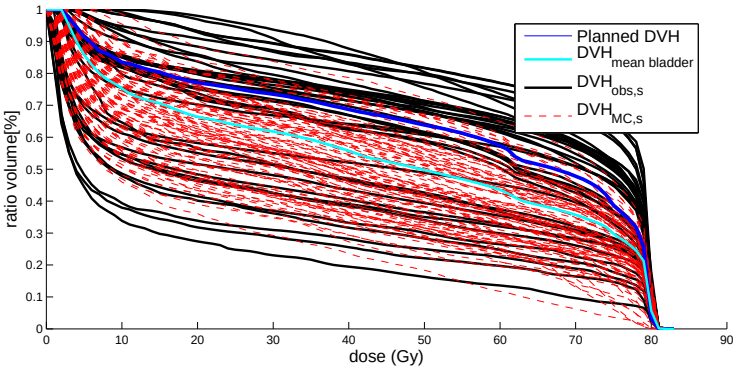

(b) DVH uncertainties resulting from MC simulation

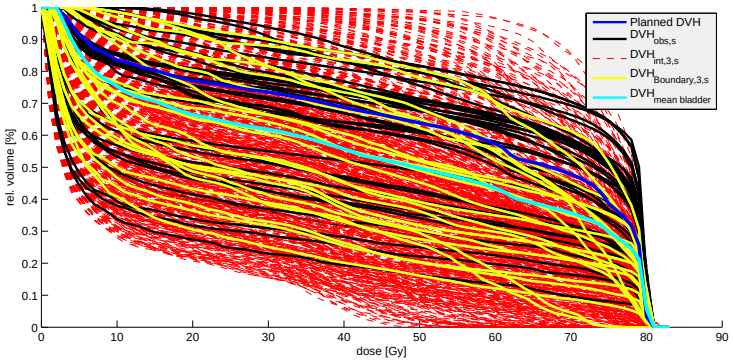

(c) DVH uncertainties resulting from dose integration

Figure 6.7: Visualization of DVH uncertainties for Patient 1. (a) Mean (green) and accumulated DVHs (red) resulting from Monte Carlo (MC) simulation are depicted. Planned DVH (blue) and DVH (cyan) obtained from the patient's mean bladder shape are also illustrated. (b) DVH uncertainties resulting from observed and estimated bladder structures (rescaled to the total dose) in the MC simulation. (c) DVH uncertainties resulting from observed and estimated bladder structures (rescaled to the total dose) in the dose integration and confidence region (CR).

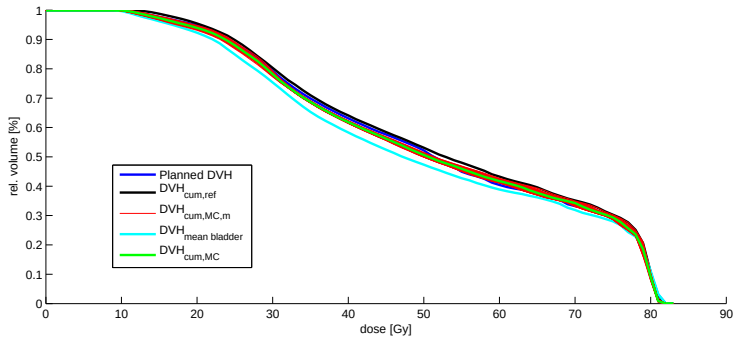

(a) $DVH_{cum,MC,m}$ and $DVH_{cum,MC}$

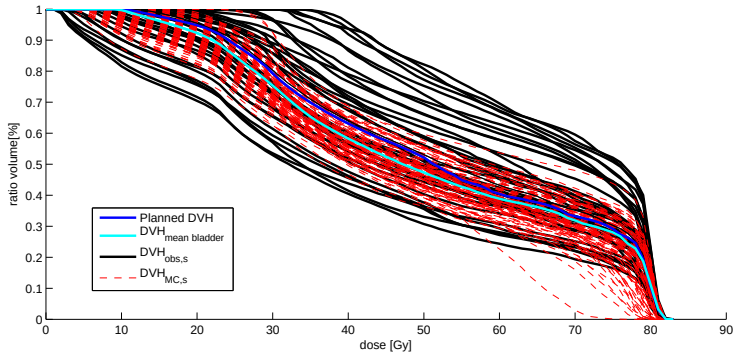

(b) DVH uncertainties resulting from MC simulation

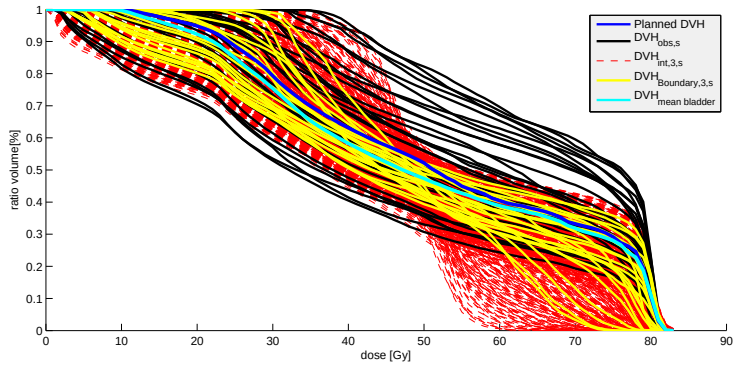

(c) DVH uncertainties resulting from dose integration

Figure 6.8: Visualization of DVH uncertainties for Patient 2. (a) Mean (green) and accumulated DVHs (red) resulting from Monte Carlo (MC) simulation are depicted. Planned DVH (blue) and DVH (cyan) obtained from the patient's mean bladder shape are also illustrated. (b) DVH uncertainties resulting from observed and estimated bladder structures (rescaled to the total dose) in the MC simulation. (c) DVH uncertainties resulting from observed and estimated bladder structures (rescaled to the total dose) in the dose integration and confidence region (CR).

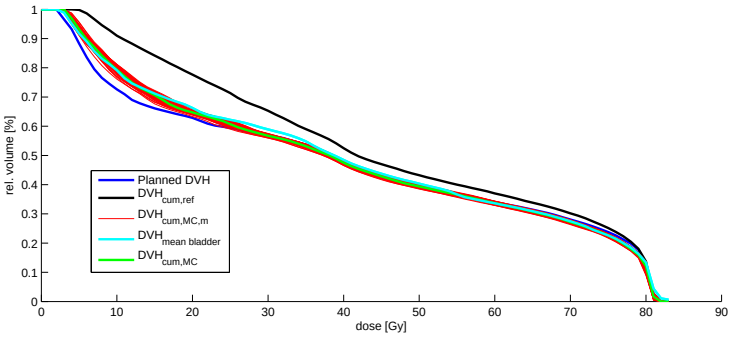

(a) $DVH_{cum,MC,m}$ and $DVH_{cum,MC}$

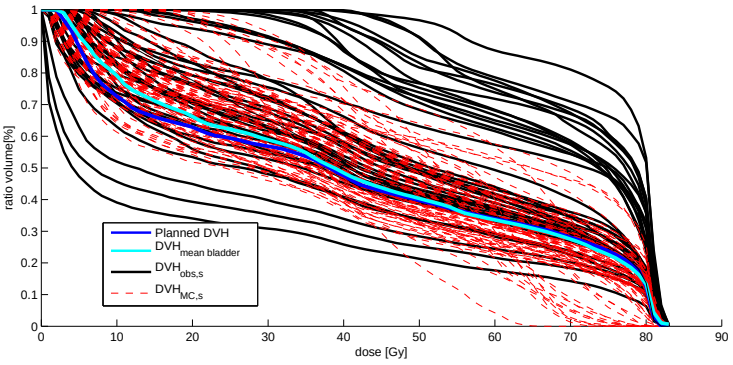

(b) DVH uncertainties resulting from MC simulation

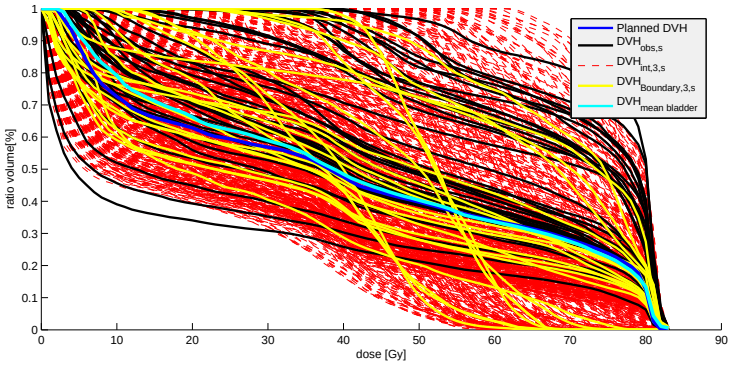

(c) DVH uncertainties resulting from dose integration

Figure 6.9: Visualization of DVH uncertainties for Patient 3. (a) Mean (green) and accumulated DVHs (red) resulting from Monte Carlo (MC) simulation are depicted. Planned DVH (blue) and DVH (cyan) obtained from the patient's mean bladder shape are also illustrated. (b) DVH uncertainties resulting from observed and estimated bladder structures (rescaled to the total dose) in the MC simulation. (c) DVH uncertainties resulting from observed and estimated bladder structures (rescaled to the total dose) in the dose integration and confidence region (CR).

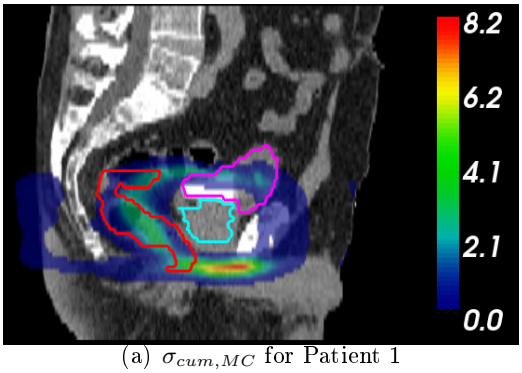

(a) $\sigma_{cum,MC}$ for Patient 1

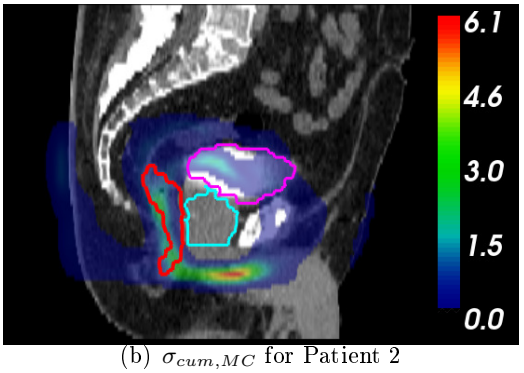

(b) $\sigma_{cum,MC}$ for Patient 2

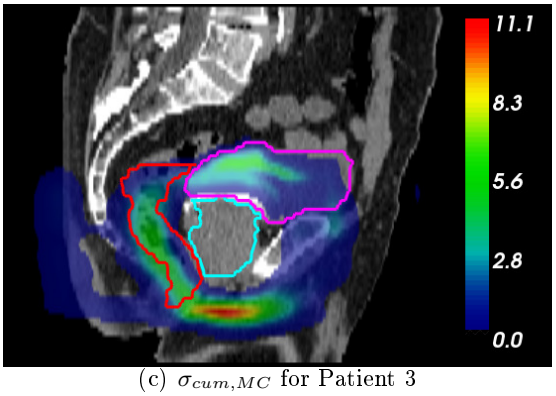

(c) $\sigma_{cum,MC}$ for Patient 3

Figure 6.10: 3D sagittal views of $\sigma_{cum,MC}$ for each patient. Segmented prostate (cyan), bladder (purple) and rectum (red) at the planning CT scan are overlaid.

6.4 Discussion

We have quantified dosimetric uncertainties produced by geometric variations of the bladder between fractions using PCA models. For each patient in the study we trained an individual PCA model using the available bladder samples from the on-treatment CT/CBCTs. We also calculated three accumulated doses: a reference accumulated dose obtained from the available CT/CBCTs via DIR; an accumulated dose derived via Monte Carlo simulation of treatment courses; and an accumulated dose computed via dose integration. We sought to determine the number of modes required to properly estimate patient-specific dose uncertainties using an iterative procedure. We subsequently compared the three accumulated doses, and we calculated average voxel doses, local dose variability and dose-volume histogram uncertainties.

Concerning to patient-specific models, we obtained that at least $q \sim 8 - 11$ modes were required to describe most of the geometric variability observed in the on-treatment CBCTs. Although, Shön et al (2005) studied a composite of prostate/bladder/ rectum for individual patients, results from eigenvalue spectrum showed that the same range of mode number was required to describe the same level of accumulated variability for

Table 6.2: Relative errors from the metric $dist_{dose}$ for the mean and variance accumulated dose via integration for Patient 1.

Modes	$dist_{dose}$ $(\mu_{cum,int,q}, \mu_{cum,int,q-1})$	$dist_{dose}$ $(\mu_{cum,int,q}, \mu_{cum,MC})$	$dist_{dose}$ $(\sigma_{cum,int,q}, \sigma_{cum,int,q-1})$
1	–	3%	–
1 and 2	2.5%	1.8%	72%
1,2 and 3	0.8%	1.6%	17%

Table 6.3: Relative errors from the metric $dist_{dose}$ for the mean and variance accumulated dose via integration for Patient 2.

Modes	$dist_{dose}$ $(\mu_{cum,int,q}, \mu_{cum,int,q-1})$	$dist_{dose}$ $(\mu_{cum,int,q}, \mu_{cum,MC})$	$dist_{dose}$ $(\sigma_{cum,int,q}, \sigma_{cum,int,q-1})$
1	–	2.5%	–
1 and 2	1.4%	1.5%	45%
1,2 and 3	0.45%	1.4%	8.4%

Table 6.4: Relative errors from the metric $dist_{dose}$ for the mean and variance accumulated dose via integration for Patient 3.

Modes	$dist_{dose}$ $(\mu_{cum,int,q}, \mu_{cum,int,q-1})$	$dist_{dose}$ $(\mu_{cum,int,q}, \mu_{cum,MC})$	$dist_{dose}$ $(\sigma_{cum,int,q}, \sigma_{cum,int,q-1})$
1	–	3.2%	–
1 and 2	2%	2%	20%
1,2 and 3	1%	1.7%	9%

the studied patients. As a result, we consider that at least an input sample of $N = 12$ on treatment CT/CBCTs would be necessary to obtain a patient-specific PCA model. From Fig. 6.6, it can be observed that PCA may be sensible to outlier observations. For Patient 3, for instance, few large volume variations were observed in the upper-ventral region of the bladder while most of its geometric variations were in the central and lower region. Nevertheless, these outlier observations led to include this direction in the modes obtained by the PCA and to estimate geometric variations along this mode (see Fig. 6.6f). As a result, we consider that motion-deformation models based on PCA are mainly affected by outlier observations in two aspects: in overestimating directions of geometric variability and in misestimating the average bladder shape. It can also be observed that PCA models estimated a motion/deformation region that looks like an ellipsoid around the patient's average bladder. This result can be explained as PCA models estimate bladder geometries by linearly deforming the average bladder shape along the dominating modes following a normal distribution. From Fig. 6.6e and 6.6f, we consider that PCA models may have limitations to properly describe geometric

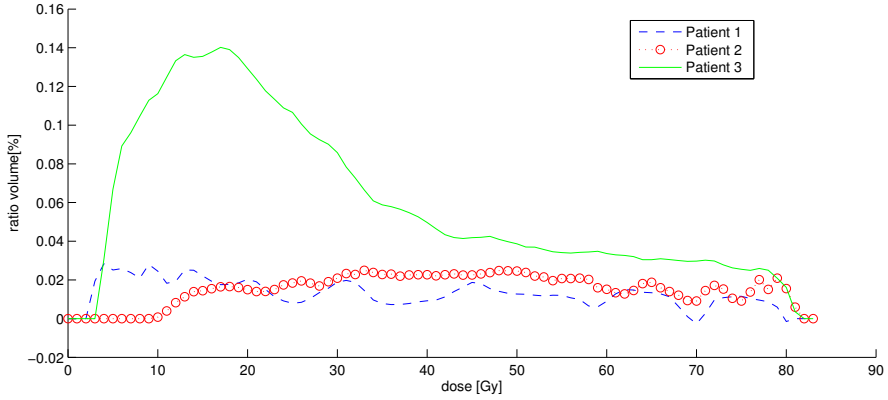

(a) $DVH_{cum,ref} - DVH_{cum,MC}$

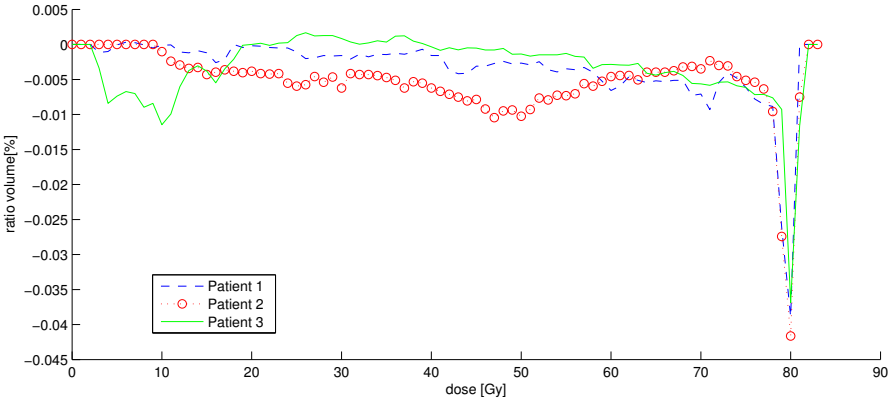

(b) $DVH_{Int,ref,3} - DVH_{cum,MC}$

Figure 6.11: DVH differences between the reference and estimated accumulated doses for all the three patients. (a) DVH differences between the reference accumulated $DVH_{cum,ref}$ and the mean accumulated $DVH_{cum,MC}$ via MC simulation. (b) DVH differences between the accumulated DVH $DVH_{cum,int.3}$ obtained with dose integration over the first three modes and the mean accumulated $DVH_{cum,MC}$ obtained via MC simulation.

variations of highly varying tissue like the bladder as contours of equal probability in the observed PMs did not follow an elliptical behavior.

From Fig. 6.7b and 6.9b, we think that the average bladder shape may not be feasible to estimate the accumulated dose as geometric variations of the bladder were not symmetrically distributed around the patient's average bladder shape. For Patient 1 and 3, it can be observed that single-fraction DVHs from observed bladder geometries ($DVH_{obs,s}$) were highly distributed above the DVH obtained from the average bladder shape ($DVH_{\text{mean bladder}}$). As a result, this may also indicate that geometric variations of the bladder may not follow a Gaussian distribution along the limited set of orthogonal

modes. A possible solution may thus consider a non-Gaussian parametric probability density function (PDF) to represent the distribution of PCA scores related to intra-subject organ motion. However, as it may be reasonable to assume that an organ moves and deforms following a Gaussian distribution along a set of dominating directions, future works can be focused to apply Kernel PCA in order to determine non-orthogonal directions that better describe geometric variations of the bladder. Previously, Kernel PCA has been used to develop 4D motion models for the lung [67].

From Fig. 6.7c, 6.8c and 6.9c, it is observed that the CR of 95% of probability described by the first three modes included most of the bladder geometries estimated in the MC simulation. We thereby consider that it is possible to estimate the uncertainty region of bladder motion and deformation by using solely the joint distribution of the first three modes. This CR thus enable us to infer those dose fractions that are more probable of being delivered during treatment for a patient. However, relative dose errors in Tables 6.2, 6.3 and 6.4 established that the mean accumulated dose was mainly described by the first mode. These relative errors indicated that the first mode enable us to obtain a good approximation of the estimated accumulated dose with errors less than 5%, and also that including a second mode would reduce at most a 2% of the estimation error. As a result, we conclude that the first mode is enough to obtain good estimation of the accumulated dose during treatment. It is important to highlight that results in this study have established that the first mode described the direction of maximum volume variability, and we therefore think that the accumulated dose is mainly described by those volume changes that takes places along this direction.

Concerning dosimetric uncertainties, relative dose errors in Tables 6.2, 6.3 and 6.4 indicated that the estimation of the dose variance converged as the number of modes was increased. Nevertheless, at least four modes would be required to reduce the converge error to a value lower than 10%. As in [50,111], it is observed from Fig. 6.10 that those voxels with highest dose variations were obtained in the center region of the bladder, i.e., the region of the bladder that is not directly connected to the prostate. We consider that this can be understood as dose varies only on tissue elements that move in or out of the beams and not at the border region to the prostate. Future studies should now be conducted to determine the number of modes to fully determine dosimetric uncertainties for the bladder.

6.5 Conclusion

We have hereby presented PCA models as a tool to quantify and predict dosimetric uncertainties produced by inter-fraction geometric variations of the bladder. We have provided the number of modes required to determine motion/deformation regions as well as to estimate the accumulated dose of the bladder. We also showed some limitations of PCA models to describe bladder motion and deformation between fractions. Future studies should now be conducted to validate the number of modes required to estimate the accumulated dose by means of a large cohort of patients who have undergone prostate cancer radiotherapy. Future studies could also be focused on the relationship

between inter-fraction bladder motion/deformation, delivered dose, and late GU toxicity in the prostate cancer radiotherapy context.

Conclusion and perspectives

Conclusion and perspectives

This final chapter contains general remarks on the main results presented in this dissertation. Perspectives are made to further extend the research presented in this work in several directions.

Concluding remarks

In this thesis we have presented a methodology to characterize and predict bladder motion and deformation between fractions using solely the planning CT scan for prostate cancer radiotherapy. In this study we have followed a population approach as in clinical practice only the planning CT scan is available for a typical patient, while on-treatment CT/CBCT scans are seldom available. In this study we have considered that bladder motion and deformation between fractions is not a chaotic process and neither a deterministic. We have instead considered that the bladder randomly moves and deforms along a limited number of geometric directions in a relatively stable overall shape. As previous work these directions were also determined using PCA based on the assumption that principal directions of geometric variations are similar in all patients, despite the potential variations in organ size and shape across the population.

This dissertation considered three main research subjects. Firstly, it focused on the characterization of shapes and motion/deformation regions of the bladder for a database of patients using PCA; secondly, it proposed to use a longitudinal approach to predict patient-specific bladder motion and deformation for an unseen patient by learning from a longitudinal training database; thirdly, this thesis presented PCA models as virtual tool to evaluate dosimetric uncertainties produced by bladder motion and deformation between fractions. Concerning the first research subject, we have the following concluding remarks:

- A normalization method was proposed to anatomically align the pelvic structures (prostate and bladder) for all the patients in the same spatial referential. This method was a prostate-based rigid registration that enabled bladder motion and deformations to be quantified with respect to the prostate barycenter of a template patient. However, this spatial normalization introduces inter-patient geometric variations in the lower posterior part of the bladder – the region that presented the geometric variations produced by the barycenter alignment– that may be captured by higher modes. Although in our study, these geometric variations

were not captured by the most significant modes, higher modes describing these geometric variations may lead to estimate unrealistic deformations in the most stable part of the bladder. Nevertheless, such modes may have a low impact in the estimation of motion-deformation regions and cumulated doses.

- Surface parametrization by means of SPHARM offered the advantage of significantly reducing the number of variables required to represent the bladder surface without resulting in a loss of information. This parametrization thus enabled us to reduce computation time, numerical errors by affording finite arithmetic operations, and data storage.
- As in previously-proposed population-based models, the main directions of geometric variability were determined using PCA. These directions enabled us to characterize shapes and motion/deformation regions of the bladder; and subsequently, to visualize and quantify the heterogeneous variability observed in the database.

Concerning the second research subject, our aim was to characterize intra and inter-patient variability of the bladder observed in a population database to subsequently infer a probable region of bladder motion and deformation. We have the subsequent concluding remarks:

- We firstly sought to characterize patient-specific variance from the population using mixed-effects models. This technique enables us to consider the inherent correlation of intra-individual observations, while reducing observed population variance by grouping repeated observations per patient by means of a "patient factor". However, in population databases of highly varying soft-tissue like the bladder, a large number of modes may be required to properly capture the complex shape variations observed in the training database. We consider that the large number of modes makes the inference and analysis of the ME models' parameters difficult.
- We secondly sought to characterize patient-specific modes from the population using hierarchical PCA. This methodology increased the degree of freedom of the motion/deformation model as the number of geometrical directions described by the first modes in the hierarchical models has been increased compared to the groundwork PCA models. Nevertheless, hierarchical PCA models introduced a higher number of parameters, increasing the model complexity.

From both remarks, we conclude that both techniques enabled us to reduce the uncertainties in the estimation of the probable motion/deformation region. Finally, we have the subsequent concluding remarks concerning the third research subject of this dissertation:

- Patient-specific PCA models were presented as tools to quantify and predict dosimetric uncertainties produced by inter-fraction geometric variations of the bladder. Our main contributions were the number of modes required to determine

motion/deformation regions as well as to estimate the cumulated dose of the bladder.

- The delivered dose only varies on tissue elements that move in or out of the beams and not at the border region to the prostate. We have showed that only the first mode had a significant impact on the cumulated dose estimation as it described the most significant changes in volume outside the beams.

It is worth mentioning that in this study we have defined several covariance matrices in order to determine modes of bladder geometrical variability. Physical interpretations of such modes were provided as a qualitative validation along this study. The first mode, for instance, always described the main direction where changes in volume were observed. This direction enabled us to describe the shape and motion/deformation region of the bladder for a typical patient in longitudinal analysis, and the probable cumulated dose for intra-patient analysis.

Finally, we consider that PCA models have two main limitations to model organ motion and deformation between fractions. The first limitation is related the organ mean shape used to estimate geometrical uncertainties. PCA models deform the organ mean shape along the modes with their corresponding variances to estimate new organ structures. However, several images should be required to obtain a good estimation of the true mean shape, and the organ shape delineated in the planning CT scan may only capture a momentary shape during treatment. In our study, the estimated mean shape had strong impact in the estimation of both the motion/deformation region and cumulated dose. Nevertheless, this limitation can be overcome whenever more CT scans are available during treatment in an adaptive radiotherapy scheme. The second limitation is related to assuming that bladder moves and deforms between fractions following a Gaussian distribution. For some patients, we have observed that geometric variations of the bladder did not distributed like a bell-curve around the mean shape. As PCA models assume that geometric variations obey a Gaussian distribution along a limited number of modes, we consider orthogonal directions may not properly describe the geometric variations of the bladder between fractions. A result, future work may be extended to determine non-orthogonal directions of geometric variability that better describe bladder motion and deformation.

Perspectives

The research presented in this work can be further extended in several directions.

- We have used SPHARM to model bladder shape obtaining a significant reduction on the variables required to represent the surface. However, we consider that surface shape modeling should be improved as not all the bladder shapes were properly parameterized using the radial sampling in spherical coordinates. A first option is to extend the SPHARM methodology to model a much larger class of simply connected closed shapes using an area-preserving, distortion minimizing spherical mapping as expressed in [73,80]. A second option is also to use a

different computational technique called isogeometric analysis, which generalizes and improves on the standard finite element method [84,85]. In population data, this technique offers the advantage of obtaining a surface parameterization with corresponding points in all organ instances without requiring a mesh relaxation procedure. This methodology defines a transformation to a canonical domain, where it is made the parametrization and extrapolated to any organ instance.

- In this study, we have observed that outlier observations may lead to incorrect the model's parameters (like patient-specific variance and modes, and average bladder shape). As a result, a future research topic to be explored is to analyze the robustness of the methodology for handling outlier patients using robust PCA either in population or individual motion/deformation models.

- Future work can also be focused to determine general forms of covariates that may correlate with the modes. We consider that there may be some covariates that underlie the motion/deformation region for an arbitrary patient. For example, the bladder size or volume could be considered as fixed-effects that may determine the volume changes and directions of geometric variations. In an adaptive radiotherapy scheme, it can also be added a time covariate, as a random or fixed variable, that describes the daily volume changes of the bladder.

- Future studies should also be focused on studying the impact of dosimetric uncertainties produced by inter-fraction variations of the bladder on the prediction of late GU toxicity in prostate cancer radiotherapy [35,69,111]. A recurrent criticism to DVH-based toxicity models is that they reduce 3D dose distributions to a set of dose-volume parameters [e.g. the fraction of the organ volume receiving at least X Gy (VX), or equivalent uniform dose (EUD)] in order to provide a probability for a patient of developing side effects after radiation [69,120–123]. Although this reduction enables us to study, under the same framework, patients undergoing the same treatment, crucial information may be disregarded that may help to discriminate between high-risk and low-risk treatments. For example, two patients could have the same dose-volume parameters but different dose distributions. It may therefore be important to introduce new information like inter-fraction geometric variations of organs to overcome limitations of DVH-based toxicity models [124–126].

- From a clinical point of view, the proposed methodology can be applied to tailor treatment plans to specific needs of patient. For example, it has potential applications for margin evaluation, estimation of delivered dose, on-treatment dose adaptation and the design of robust treatment plans, among others. In an adaptive radiotherapy scheme, population-based models can be used to estimate probable single dose fractions and motion-including doses for a typical patient while on-treatment CT/CBCT scans are acquired to subsequently fit a patient-specific PCA model (Söhn et al. [50] has been established 5 scans as the minimum number of observations for intra-patient models). Estimated motion-including doses

can then be used to adapt the dose during treatment. Besides of dose estimation, this methodology can also be used to adapt margins during fractions to further personalise treatment plans. As in [55], the most probable bladder contours can be generated from the population or patient-specific models in order to estimate the percentage of bladder volume inside the PTV and CTV volumes. As a result, motion-inclusive margins can be determined in order to ensure an adequate dose coverage.

Appendices

List of publications

International journal papers

R. Rios, R. de Crevoisier, J. D. Ospina, F. Commandeur, C. Lafond, A. Simon, P. Haigron , J. Espinosa, O. Acosta. Population model of motion and deformation based on eigenmodes and mixed-effects models in prostate cancer radiotherapy. Med. Image Anal., 2017, 38, 133-149.

R. Rios, J. D. Ospina, C. Lafond, O. Acosta, J. Espinosa, R. de Crevoisier. Characterization of Bladder Motion and Deformation in Prostate Cancer Radiotherapy. IRBM 37 (56), 276-283.

Peer-reviewed conference papers

R. Rios, J. D. Ospina, C. Lafond, O. Acosta, J. Espinosa, R.de Crovoiser. Characterization of geometric variations of the bladder in image guided radiotherapy of prostate cancer. Recherche en Imagarie et Technologies pour la Santé (RITS) 2015, Dourdan, France, 2015.

R. Rios, J. D. Ospina, A. Le Maitre, G. Cazoulat, R. Mathieu, A. Simon, V. Beckendorf, O. Acosta, J. Espinosa, R. de Crovoiser. Modifying the planned dose volume histogram to estimate the normal tissue complication probability. Recherche en Imagarie et Technologies pour la Santé (RITS) 2013, April, Bordeaux, France, 2013.

J. D. Ospina, F. Commandeur, R. Rios, G. Dréa, J.C. Correa, A. Simon, P. Haigron, R. , de Crevoisier, O. Acosta. A Tensor-Based Population Value Decomposition to Explain Rectal Toxicity after Prostate Cancer Radiotherapy. In Medical Image Computing and Computer-Assisted Intervention-MICCAI 2013, pp. 387-394. Springer Berlin Heidelberg, 2013.

Communications in international conferences

R. Rios, F. Commandeur, C. Lafond, O. Acosta, J. Espinosa, R. de Crovoiser. Hierarchical eigenmodes to characterize bladder motion and deformation in prostate cancer radiotherapy. In Proc. SPIE 10160, 12th International Symposium on Medical Information Processing and Analysis, vol. 10160, 2017, pp. 101 601Eâ101 601Eâ13. http://dx.doi.org/10.1117/12.2 256 916.

R. Rios, J. D. Ospina, C. Lafond, O. Acosta, J. Espinosa, R. de Crovoiser. Prediction of Geometrical Variations of the Bladder in Image Guided Radiotherapy for Prostate Cancer. ICART Workshoop MICCAI 9th October, Munich, Germany, 2015.

R. Rios, A. Le Maitre, G. Cazoulat, O. Acosta, J. Espinosa, R. de Crovoiser. Prediction of cumulative DVH in Prostate Cancer IGRT with PLS model. Proceeding in Green Journal-2nd ESTRO Forum 19-23 April 2013, Geneva, Switzerland.

Appendix A

Supplementary material for characterization of bladder motion and deformation

In this appendix, we provide supplementary material for the prostate-based rigid registration performed to normalize the patients in the training database.

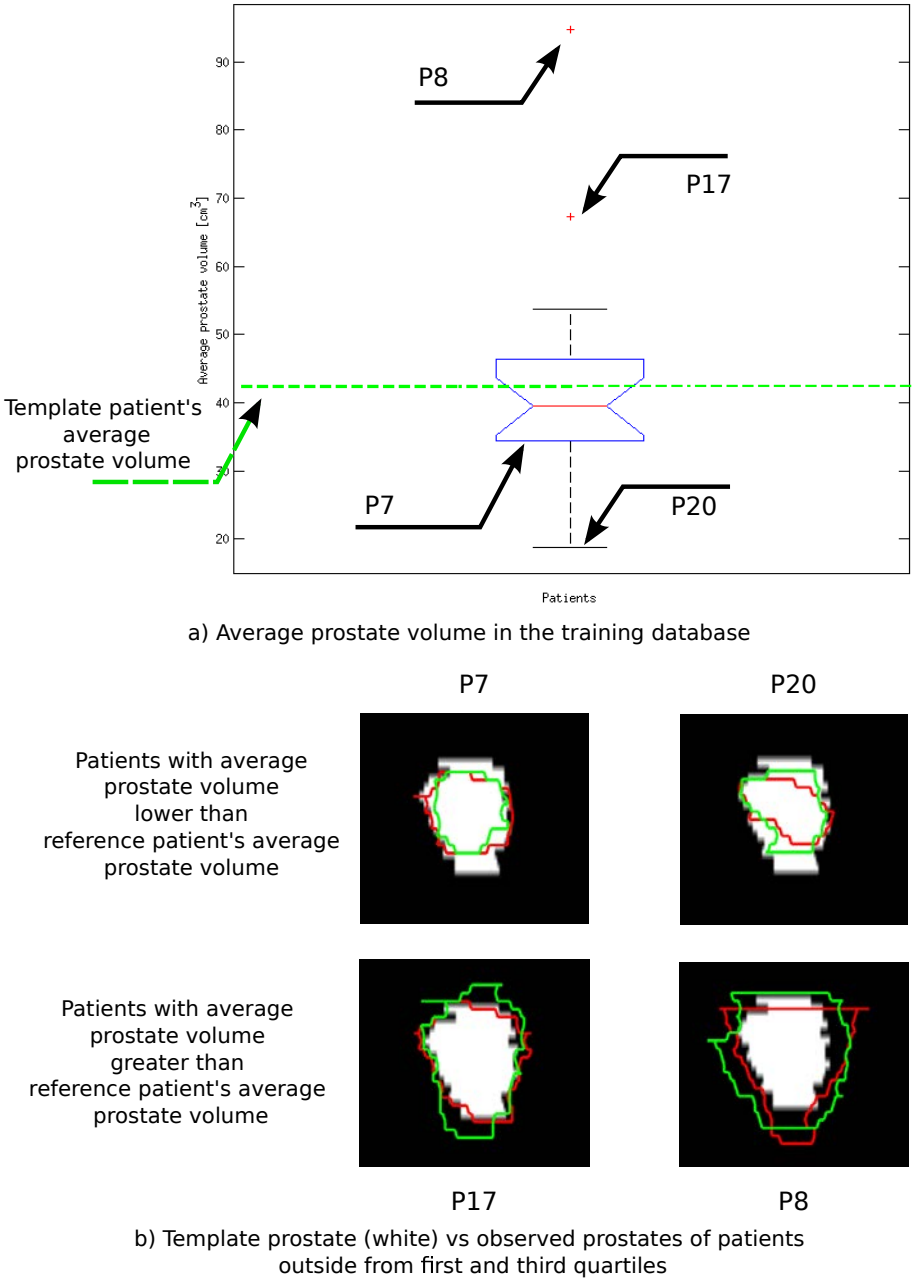

Figure A.1: (a) Boxplot of average prostate volume in the training database. Green line shows the average volume of the template prostate. (b) Overlays of some observed prostates (green and red) of patients outside from first and third quartiles vs template prostate (white).

Appendix B

Cluster center that minimizes the distance to data point in K-means clustering

In this appendix, we outline the mathematical details that prove the equality between both arguments arg in Eq. 5.5.

Corollary

Let $m_1, m_2, \ldots, m_{\mathcal{T}}$ and w be vectors in $\mathbf{R}^n$. We thus aim to prove that:

$$t = \arg\min_b \|w - m_b\|^2 = \arg\max_b \; w^T m_b - \frac{\|m_b\|^2}{2} \tag{B.1}$$

For an arbitrary m_b, it holds that

$$\begin{aligned} \|w - m_b\|^2 &= \langle w - m_b, w - m_b \rangle \\ &= \|w\|^2 - 2\langle w, m_b \rangle + \|m_b\|^2 \\ -\frac{\|w - m_b\|^2}{2} &= \langle w, m_b \rangle - \frac{\|w\|^2}{2} - \frac{\|m_b\|^2}{2} \end{aligned} \tag{B.2}$$

Because m_b was arbitrary and w fixed, it then means that

$$
\begin{aligned}
t = \arg\min_b \ \|w - m_b\|^2 &= \arg\max_b \ -\frac{\|w - m_b\|^2}{2} \\
&= \arg\max_b \ \langle w, m_b \rangle - \frac{\|w\|^2}{2} - \frac{\|m_b\|^2}{2} \\
&= \arg\max_b \ \langle w, m_b \rangle - \frac{\|m_b\|^2}{2}
\end{aligned}
\tag{B.3}
$$

This establishes the equality.

Appendix C

Elements of numerical analysis for solving mean and variance dose integrals

In this appendix we describe the numerical details used to solve the multidimensional integrals involved in the computation of the mean and variance cumulated dose (see Eqs. 6.6). We describe algorithms to calculate both integrals restricted to the first three modes. The generalization to further modes can be done following an inductive procedure. Further elements about numerical integration can be found in [127].

The mean and variance cumulated dose restricted to the first mode

Let's firstly solve the integral of the cumulative distribution function (CDF) of the Gaussian distribution for the first mode using the Composite Simpson's rule, as follows:

$$\begin{aligned} CDF &= \int_{-\infty}^{\infty} f_z(z_1) d_{z_1} = \int_{-\infty}^{\infty} \frac{1}{\sqrt{2\pi\lambda_1}} exp\Big(\frac{1}{2} z_1^2/\lambda_1\Big) d_{z_1} \\ &= 1 \approx \int_{-3.5\sigma_1}^{3.5\sigma_1} \frac{1}{\sqrt{2\pi\lambda_1}} exp\Big(\frac{1}{2} z_1^2/\lambda_1\Big) d_{z_1} \end{aligned} \tag{C.1}$$

where $\sigma_1 = \sqrt{\lambda_1}$. As for the normal distribution, the values less than three standard deviations away from the mean account for 99.73% of the set, the improper integral in Eq. C.1 can then be approximated by a definite integral defined in the interval $[-3.5\sigma_1, 3.5\sigma_1]$. The interval $[-3.5\sigma_1, 3.5\sigma_1]$ is split up into a even number n_1 of subintervals and evenly spaced mesh points $z_{1,0}, \ldots, z_{1,n}$ to apply the Composite Simpson's rule. The improper integral can then be approximated as follows:

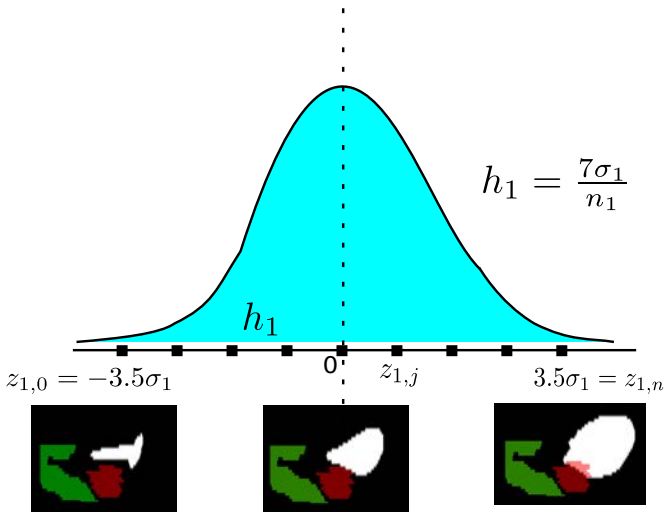

Figure C.1: Visualization of the Gaussian distribution of the first mode for a patient in the interval $[-3.5\sigma_1, 3.5\sigma_1]$. The interval was split up into a even number n_1 of subintervals equally spaced by h_1.

$$\begin{aligned} CDF &= \int_{-\infty}^{\infty} f_z(z_1) d_{z_1} \\ &\approx \frac{h_1}{3}\Big(f_z(-3.5\sigma_1) + f_z(3.5\sigma_1) + 4\sum_{i=1}^{n_1/2} f_z(z_{1,2i-1}) + 2\sum_{i=1}^{n_1/2} f_z(z_{1,2i})\Big) \end{aligned} \tag{C.2}$$

where $h_1 = 7\sigma_1/n_1$ is the size of the subintervals. For $n_1 = 10$, the relative error of the integral is lower than 0.05%. Defining $F_z(z_1) = D(z_1)f_z(z_1)$, the mean dose can then be calculated as follows:

$$\mu_{cum,int,1} \approx \frac{h_1}{3}\Big(F_z(-3.5\sigma_1) + F_z(3.5\sigma_1) + 4\sum_{i=1}^{n_1/2} F(z_{1,2i-1}) + 2\sum_{i=1}^{n_1/2} F(z_{1,2i})\Big) \tag{C.3}$$

where $D = D_{planned}$. The dose $D_{planned}(z_{1,i})$ was deformed using the deformation field U obtained from the DIR process between the two images resulting from the bladder contours $x_{planned}$ and $x(z_{1,i})$. For this purpose, for both the $x_{planned}$ and $x(z_{1,i})$ contours, distance maps were computed, representing for each voxel the signed squared Euclidean distance from the organ surface. Distance maps were then registered with a variant of Demons algorithm providing the estimated deformation fields. Fig.C.1 shows the Gaussian distribution of the first mode for a patient in the interval $[-3.5\sigma_1, 3.5\sigma_1]$. Similarly, the variance dose can also be calculated as follows:

$$\sigma_{cum,int,1} \approx \frac{h_1}{3}\Big(F_z(-3.5\sigma_1) + F_z(3.5\sigma_1) + 4\sum_{i=1}^{n_1/2} F(z_{1,2i-1}) + 2\sum_{i=1}^{n_1/2} F(z_{1,2i})\Big) \quad \text{(C.4)}$$

where $F_z(z_{1,i}) = (D(z_{1,i}) - \mu_{cum,int,1})^2 f_z(z_{1,i})$. We did not use the expression $D^2(z_{1,i})f_z(z_{1,i})$ because the rounding errors produced by finite-digit calculation were higher, i.e., digits of significance were lost on account of the multiplications of numbers with large magnitude ($D^2(z_{1,i})$) and subtraction of nearly equal numbers ($\int D^2 f_z dz - \mu^2$) (see Chapter 1 in [127]). Besides, it is worth highlighting that the dose was a vector where $D_{planned}(z_{1,i}) \in \mathbb{R}^{d_1 \times d_2 \times d_3}$. As a result, the numerical solutions of the integrals in Eqs. C.3 and C.4 could challenge the CPU's storage capacity and computation time, if we decided to load the $n+1$ doses at the same time. We then proposed an algorithm that can feasibly be implemented in an i7-4510U CPU @2.00GHz with 8G RAM. This algorithm is described in Algorithm 1 for the integral of Eq. C.3 (while for the integral of Eq. C.4 is straightforward by changing $s = (D(z_{1,i}) - \mu_{cum,int,1})^2 f_z(z_{1,i}) + s$).

```
Input: values of σ1; even positive integer n1; function of density probability
       fz(z)
Output: approximation s to integral
set h1 = 7σ1/n1;
set s = 0;
for i = 0 : n1 do
    load D(z1,i);
    if i is 0 then
        s = D(z1,i)f(z1,i) + s;
    else if i is n1 then
        s = D(z1,i)f(z1,i) + s;
    else if i is even then
        s = 2D(z1,i)f(z1,i) + s;
    else
        s = 4D(z1,i)f(z1,i) + s;
    end
end
s = (h1/3) s
```

Algorithm 1: Numerical algorithm to approximate the integral mean cumulated dose restricted to the first mode.

The mean and variance cumulated dose restricted to the first two modes

Let's consider the integral of the cumulative distribution function (CDF) of the Gaussian distribution for the first two modes using the Composite Simpson's rule, as follows:

$$CDF = \int_{-\infty}^{\infty}\int_{-\infty}^{\infty} f_z(z_1)d_{z_1}d_{z_2} = \int_{-\infty}^{\infty}\int_{-\infty}^{\infty}\prod_{k=1}^{2}\frac{1}{\sqrt{2\pi\lambda_k}}exp\Big(\frac{1}{2}z_k^2/\lambda_k\Big)d_{z_1}d_{z_2} \tag{C.5}$$
$$= 1 \approx \int_{-3.5\sigma_1}^{3.5\sigma_1}\int_{-3.5\sigma_2}^{3.5\sigma_2}\prod_{k=1}^{2}\frac{1}{\sqrt{2\pi\lambda_k}}exp\Big(\frac{1}{2}z_k^2/\lambda_k\Big)d_{z_1}d_{z_2}$$

where $\sigma_1 = \sqrt{\lambda_1}$ and $\sigma_2 = \sqrt{\lambda_2}$. To apply the Composite Simpson's rule, both intervals $[-3.5\sigma_1, 3.5\sigma_1]$ and $[-3.5\sigma_2, 3.5\sigma_2]$ are also divided into a even number of subintervals of equal size. To simplify the notation, we use even integers n_1 and n_2 and partitions with the evenly spaced mesh points $z_{1,0}, \ldots, z_{1,n}$ and $z_{2,0}, \ldots, z_{2,n}$ for the intervals $[-3.5\sigma_1, 3.5\sigma_1]$ and $[-3.5\sigma_2, 3.5\sigma_2]$, respectively. The improper integral can then be approximated as follows:

$$CDF = \int_{-\infty}^{\infty}\int_{-\infty}^{\infty} f_z(z_1)d_{z_1}d_{z_2} \tag{C.6}$$
$$\approx \frac{h_1}{3}\Big(G_z(-3.5\sigma_1) + G_z(3.5\sigma_1) + 4\sum_{i=1}^{n_1/2} G_z(z_{1,2i-1}) + 2\sum_{i=1}^{n_1/2} G_z(z_{1,2i})\Big)$$

where for $i = 0, \ldots, n_1$,

$$G_z(z_{1,i}) \approx \frac{h_2}{3}\Big(f_z(z_{1,i}, -3.5\sigma_2) + f_z(z_{1,i}, 3.5\sigma_2) + 4\sum_{j=1}^{n_2/2} f_z(z_{1,i}, z_{2,2j-1}) + 2\sum_{j=1}^{n_2/2} f_z(z_{1,i}, z_{2,2j})\Big) \tag{C.7}$$

The constants $h_1 = 7\sigma_1/n_1$ and $h_2 = 7\sigma_2/n_2$ are the size of the subintervals. For $n_1 = n_2 = 8$, the relative error of the integral is lower than 0.33%. Defining $F_z(z_1, z_2) = D(z_1, z_2)f_z(z_1, z_2)$ and $D = D_{planned}$, the mean dose can thus be calculated as follows:

$$\mu_{cum,int,2} = \int_{-\infty}^{\infty}\int_{-\infty}^{\infty} F_z(z_1)d_{z_1}d_{z_2} \tag{C.8}$$
$$\approx \frac{h_1}{3}\Big(G_z(-3.5\sigma_1) + G_z(3.5\sigma_1) + 4\sum_{i=1}^{n_1/2} G_z(z_{1,2i-1}) + 2\sum_{i=1}^{n_1/2} G_z(z_{1,2i})\Big)$$

where for $i = 0, \ldots, n_1$,

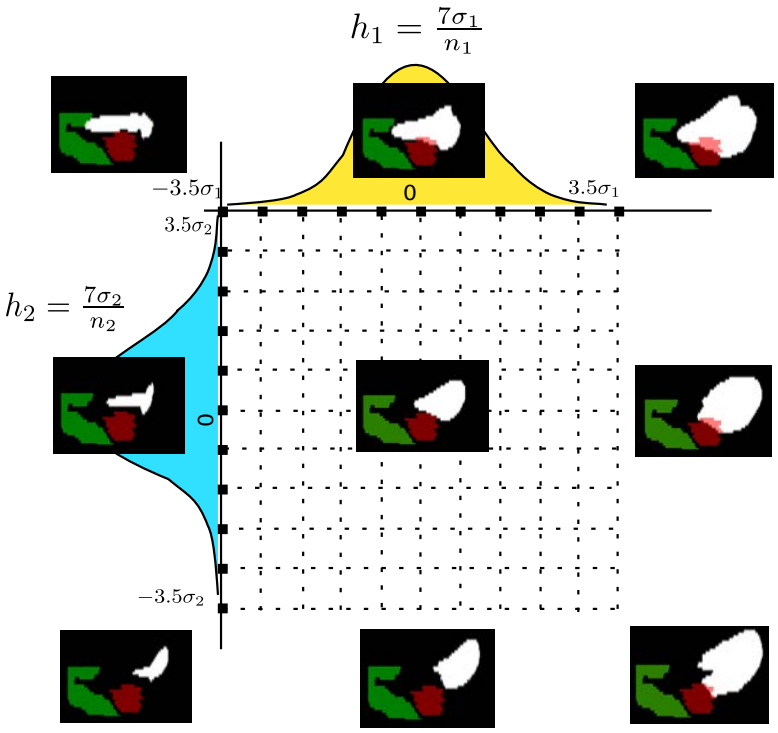

Figure C.2: Visualization of the multivariate Gaussian distribution of the first two mode for a patient in the square region $R = \{(z_1, z_2)| - 3.5\sigma_1 \leq z_1 \leq 3.5\sigma_2, -3.5\sigma_2 \leq z_2 \leq 3.5\sigma_2\}$. The square region was divided into a mesh of points $(z_{1,i}, z_{2,j})$ with $z_{1,i} = -3.5\sigma_1 + h_1 i$ and $z_{2,j} = -3.5\sigma_2 + h_2 j$ for $i = 1, \ldots, n_1$ and $j = 1, \ldots, n_2$.

$$G_z(z_{1,i}) = \frac{h_2}{3}\Big(F_z(z_{1,i}, -3.5\sigma_2) + F_z(z_{1,i}, 3.5\sigma_2) + 4\sum_{j=1}^{n_2/2} F_z(z_{1,i}, z_{2,2j-1}) + 2\sum_{j=1}^{n_2/2} F_z(z_{1,i}, z_{2,2j})\Big) \quad \text{(C.9)}$$

The dose $D_{planned}(z_{1,j}, z_{2,j})$ was also deformed using the deformation field U obtained from the DIR process between the two images resulting from the bladder $x_{planned}$ and $x(z_{1,i}, z_{2,j})$. The dose $D_{planned}(z_{1,j}, z_{2,j})$ was subsequently resampled in the planning CT with a trilinear interpolation. Fig.C.2 shows the multivariate Gaussian distribution of the first two mode for a patient in the region $R = \{(z_1, z_2)| - 3.5\sigma_1 \leq z_1 \leq 3.5\sigma_2, -3.5\sigma_2 \leq z_2 \leq 3.5\sigma_2\}$. The integral for the variance dose can also be approximated as follows:

$$\sigma_{cum,int,2} = \int_{-\infty}^{\infty}\int_{-\infty}^{\infty} F_z(z_1, z_2) d_{z_1} d_{z_2} \tag{C.10}$$
$$\approx \frac{h_1}{3}\Big(G_z(-3.5\sigma_1) + G_z(3.5\sigma_1) + 4\sum_{i=1}^{n_1/2} G_z(z_{1,2i-1}) + 2\sum_{i=1}^{n_1/2} G_z(z_{1,2i})\Big)$$

where $F_z(z_i, z_j) = (D(z_{1,i}, z_{2,j}) - \mu_{cum,int,1-2})^2 f_z(z_{1,i}, z_{2,j})$. Algorithm 2 describes the steps required to calculate the mean dose $\mu_{cum,int,1-2}$ while for the variance dose is straightforward. Because of the dose vectors $D(z_{1,i}, z_{2,j}) \in \mathbb{R}^{d_1 \times d_2 \times d_3}$, this algorithm enables us to iteratively load each deformed dose.

Input: values of σ_1 and σ_2; even positive integer n_1 and n_2; function of density probability $f_z(z)$
Output: approximation s to integral
set $h_1 = 7\sigma_1/n_1$;
set $s_1 = 0$ and $s_2 = 0$;
for $i = 0 : n_1$ **do**
  $s_2 \leftarrow$ Algorithm 1(σ_2,n_2, $f_z(z_{1,i}, :)$);
  if i *is* 0 **then**
    $s_1 = s_2 + s_1$;
  else if i *is* n_1 **then**
    $s_1 = s_2 + s_1$;
  else if i *is even* **then**
    $s_1 = s_2 + s_1$;
  else
    $s_1 = s_2 + s_1$;
  end
end
$s = \frac{h_1}{3} s_1$

Algorithm 2: Numerical algorithm to approximate the integral mean cumulated dose restricted to the first two modes.

The mean and variance cumulated dose restricted to the first three modes

Let's consider the integral of the cumulative distribution function (CDF) of the Gaussian distribution for the first three modes using the Composite Simpson's rule, as follows:

$$CDF = \int_{-\infty}^{\infty}\int_{-\infty}^{\infty}\int_{-\infty}^{\infty} f_z(z_1)d_{z_1}d_{z_2}d_{z_3} \tag{C.11}$$
$$= 1 \approx \int_{-3.5\sigma_1}^{3.5\sigma_1}\int_{-3.5\sigma_2}^{3.5\sigma_2}\int_{-3.5\sigma_3}^{3.5\sigma_3}\prod_{k=1}^{3}\frac{1}{\sqrt{2\pi\lambda_k}}exp\Big(\frac{1}{2}z_k^2/\lambda_k\Big)d_{z_1}d_{z_2}d_{z_3}$$

where $\sigma_1 = \sqrt{\lambda_1}$, $\sigma_2 = \sqrt{\lambda_2}$ and $\sigma_3 = \sqrt{\lambda_3}$. To apply the Composite Simpson's rule, the intervals $[-3.5\sigma_1, 3.5\sigma_1]$, $[-3.5\sigma_2, 3.5\sigma_2]$ and $[-3.5\sigma_3, 3.5\sigma_3]$ are also divided into a even number of subintervals of equal size. To simplify the notation, we use even integers n_1, n_3 and n_2 and partitions with the evenly spaced mesh points $z_{1,0}, \ldots, z_{1,n}$, $z_{2,0}, \ldots, z_{2,n}$ and $z_{3,0}, \ldots, z_{3,n}$ for the intervals $[-3.5\sigma_1,\ 3.5\sigma_1]$, $[-3.5\sigma_2, 3.5\sigma_2]$ and $[-3.5\sigma_3,\ 3.5\sigma_3]$, respectively. The improper integral can then be approximated as follows:

$$CDF = \int_{-\infty}^{\infty}\int_{-\infty}^{\infty}\int_{-\infty}^{\infty} f_z(z_1)d_{z_1}d_{z_2}d_{z_3} \tag{C.12}$$
$$\approx \frac{h_3}{3}\Big(H_z(-3.5\sigma_3) + H_z(3.5\sigma_3) + 4\sum_{r=1}^{n_3/2} H_z(z_{3,2r-1}) + 2\sum_{r=1}^{n_3/2} H_z(z_{3,2r})\Big)$$

where for $r = 0, \ldots, n_3$ and $i = 0, \ldots, n_1$,

$$H_z(z_{3,r}) = \frac{h_1}{3}\Big(G_z(-3.5\sigma_1, z_{3,r}) + G_z(3.5\sigma_1, z_{3,r}) + 4\sum_{i=1}^{n_1/2} G_z(z_{1,2i-1}, z_{3,r}) + 2\sum_{i=1}^{n_1/2} G_z(z_{1,2i}, z_{3,r})\Big) \tag{C.13}$$

$$G_z(z_{1,i}, z_{3,r}) = \frac{h_2}{3}\Big(f_z(z_{1,i}, -3.5\sigma_2, z_{3,r}) + f_z(z_{1,i}, 3.5\sigma_2, z_{3,r}) + 4\sum_{j=1}^{n_2/2} f_z(z_{1,i}, z_{2,2j-1}, z_{3,r}) + 2\sum_{j=1}^{n_2/2} f_z(z_{1,i}, z_{2,2j}, z_{3,2r})\Big) \tag{C.14}$$

The constants $h_1 = 7\sigma_1/n_1$, $h_2 = 7\sigma_2/n_2$ and $h_3 = 7\sigma_3/n_3$ are the size of the subintervals. For $n_1 = n_2 = n_3 = 8$, the relative error of the integral is lower than 0.5%. Defining $F_z(z) = D(z_1, z_3, z_3)f_z(z_1, z_2, z_3)$ and $D = D_{planned}$, the mean dose can thus be calculated as follows:

$$\mu_{cum,int,3} = \int_{-\infty}^{\infty}\int_{-\infty}^{\infty}\int_{-\infty}^{\infty} F_z(z) d_{z_1} d_{z_2} d_{z_3} \tag{C.15}$$
$$\approx \frac{h_3}{3}\Big(H_z(-3.5\sigma_3) + H_z(3.5\sigma_3) + 4\sum_{r=1}^{n_3/2} H_z(z_{3,2r-1}) + 2\sum_{r=1}^{n_1/2} G_z(z_{3,2r})\Big)$$

where for $r = 0, \ldots, n_3$ and $i = 0, \ldots, n_1$ in Eq. C.14,

$$G_z(z_{1,i}, z_{3,r}) = \frac{h_2}{3}\Big(F_z(z_{1,i}, -3.5\sigma_2, z_{3,r}) + F_z(z_{1,i}, 3.5\sigma_2, z_{3,r}) + 4\sum_{j=1}^{n_2/2} F_z(z_{1,i}, z_{2,2j-1}, z_{3,r}) + 2\sum_{j=1}^{n_2/2} F_z(z_{1,i}, z_{2,2j}, z_{3,2r})\Big) \tag{C.16}$$

The dose $D_{planned}(z_{1,j}, z_{2,j}, z_{3,r})$ was also deformed using the deformation field U obtained from the DIR process between the two images resulting from the bladder $x_{planned}$ and $x(z_{1,i}, z_{2,j}, z_{3,r})$. The dose $D_{planned}(z_{1,j}, z_{2,j}, z_{3,r})$ was subsequently resampled in the planning CT with a trilinear interpolation. The integral for the variance dose can also be approximated as follows:

$$\sigma_{cum,int,3} = \int_{-\infty}^{\infty}\int_{-\infty}^{\infty}\int_{-\infty}^{\infty} F_z(z) d_{z_1} d_{z_2} d_{z_3} \tag{C.17}$$
$$\approx \frac{h_3}{3}\Big(H_z(-3.5\sigma_3) + H_z(3.5\sigma_3) + 4\sum_{r=1}^{n_3/2} H_z(z_{3,2r-1}) + 2\sum_{r=1}^{n_3/2} H_z(z_{3,2r})\Big)$$

where $F_z(z) = (D(z) - \mu_{cum,int,1-3})^2 f_z(z)$. Algorithm 3 describes the steps required to calculate the mean dose $\mu_{cum,int,1-3}$ while for the variance dose is also straightforward. Because of the dose vectors $D(z) \in \mathbb{R}^{d_1 \times d_2 \times d_3}$, this algorithm also enables us to iteratively load each deformed dose.

Data: value of σ_1, σ_2 and σ_3; even positive integer n_1, n_2 and n_3; function of density probability $f(z)$
Result: approximation s to integral
set $h_3 = 7\sigma_3/n_3$;
set $s_1 = 0$ and $s_2 = 0$;
for $r = 0 : n_3$ **do**
  $s_2 \leftarrow$ Algorithm 2(σ_1,σ_2,n_1,n_2, $f_z(:,:,z_{3,r})$);
  if r *is* 0 **then**
    $s_1 = s_2 + s_1$;
  else if r *is* n_3 **then**
    $s_1 = s_2 + s_1$;
  else if r *is even* **then**
    $s_1 = s_2 + s_1$;
  else
    $s_1 = s_2 + s_1$;
  end
end
$s = \frac{h_3}{3} s_1$

Algorithm 3: Numerical algorithm to approximate the integral mean cumulated dose restricted to the first three modes.

Bibliography

[1] B. W. Sterwart and C. P. Wild, "World cancer report 2014," World Health Organization, Tech. Rep., 2014.

[2] INCa, "Les cancers en france en 2014," Institut National du Cancer (INCa), Boulogne-Billancourt,, Tech. Rep., octobre 2011.

[3] INC, "Guia de atencion integral para la deteccion temprana, diagnostico, tratamiento, seguimiento y rehabilitacion del cancer de prostata," Instituo Nacional de Cancerlogia, Ministerio de Salud y Proteccion Social, Colciencias,, Tech. Rep., 2013.

[4] "Cancer country profiles 2014," World Health Organization, Tech. Rep., 2014.

[5] A. Stangelberger, M. Waldert, and B. Djavan, "Prostate Cancer in Elderly Men," Rev. Urol., vol. 10, no. 2, pp. 111–119, 2008.

[6] H. Scher, J. Isaacs, and M. J. Zelefsky, Prostate cancer, 2nd ed. Abeloff MD, Armitage JO, Lichter AS, et al., editors. Clinical Oncology. New York, NY : Churchill Livingstone, pages 1823 -1884., 2000.

[7] A. Heidenreich, P. J. Bastian, J. Bellmunt, M. Bolla, S. Joniau, T. van der Kwast, M. Mason, V. Matveev, T. Wiegel, F. Zattoni, and N. Mottet, "EAU Guidelines on Prostate Cancer. Part 1: Screening, Diagnosis, and Local Treatment with Curative Intent-Update 2013," European Urology, vol. 65, no. 1, pp. 124–137, Jan. 2014.

[8] A. Heidenreich, G. Aus, M. Bolla, S. Joniau, V. B. Matveev, H. P. Schmid, and F. Zattoni, "EAU Guidelines on Prostate Cancer," European Urology, vol. 53, no. 1, pp. 68–80, Jan. 2008.

[9] L. Lemaitre, A. Villers, D. Mouton, and P. Puech, "Echographie et biopsies de prostate," J. Radiol., vol. 87, no. 2, pp. 201–209, Feb. 2006.

[10] M. Ghei, S. Pericleous, A. Kumar, R. Miller, S. Nathan, and B. H. Maraj, "Finger-guided transrectal biopsy of the prostate: a modified, safer technique." Ann. R. Coll. Surg. Engl., vol. 87, no. 5, pp. 386–387, Sep. 2005.

[11] J. I. Epstein, W. C. Allsbrook, M. B. Amin, L. L. Egevad, and ISUP Grading Committee, "The 2005 International Society of Urological Pathology (ISUP) Consensus Conference on Gleason Grading of Prostatic Carcinoma," Am. J. Surg. Pathol., vol. 29, no. 9, pp. 1228–1242, Sep. 2005.

[12] J. I. Epstein, L. Egevad, M. B. Amin, B. Delahunt, J. R. Srigley, P. A. Humphrey, and Grading Committee, "The 2014 International Society of Urological Pathology (ISUP) Consensus Conference on Gleason Grading of Prostatic Carcinoma: Definition of Grading Patterns and Proposal for a New Grading System," Am. J. Surg. Pathol., vol. 40, no. 2, pp. 244–252, Feb. 2016.

[13] M. J. Barry, "Clinical practice. Prostate-specific-antigen testing for early diagnosis of prostate cancer," N. Engl. J. Med., vol. 344, no. 18, pp. 1373–1377, May 2001.

[14] M. Peyromaure, P. Beuzeboc, L. Salomon, P. Richaud, P. Coloby, B. Malavaud, X. Rebillard, P. Rischmann, A. Villers, and M. Soulie, "Le dépistage du cancer de la prostate en 2009: mise au point du comité de cancérologie de l'association francaise d'urologie," Progrés en Urologie, vol. 20, no. 1, pp. 17–23, Jan. 2010.

[15] S. Natarajan, L. S. Marks, D. J. A. Margolis, J. Huang, M. L. Macairan, P. Lieu, and A. Fenster, "Clinical application of a 3d ultrasound-guided prostate biopsy system," Urologic Oncology: Seminars and Original Investigations, vol. 29, no. 3, pp. 334–342, May 2011.

[16] D. Bonekamp, M. A. Jacobs, R. El-Khouli, D. Stoianovici, and K. J. Macura, "Advancements in MR Imaging of the Prostate: From Diagnosis to Interventions," RadioGraphics, vol. 31, no. 3, pp. 677–703, May 2011.

[17] S. Edge, D. Byrd, C. Compton, A. Fritz, F. Greene, and A. Trotti, Eds., AJCC: Cancer Staging Manual. Springer, 2010.

[18] A. Barrett, J. Dobbs, S. Morris, and T. Roques, Practical Radiotherapy Planning, 4th ed. Hodder Education, an Hachette UK Company, London, UK, 2009.

[19] A. Magheli and A. L. Burnett, "Erectile dysfunction following prostatectomy: prevention and treatment," Nat Rev Urol, vol. 6, no. 8, pp. 415–427, Aug. 2009.

[20] B. Hardemark, A. Liander, H. Rehbinder, and J. Löf, "Direct machine parameter optimization with raymachine® in pinnacle3®" RaySearch White Paper. Stockholm, Sweden: RaySearch Laboratories AB, 2003.

[21] D. Verellen, M. De Ridder, N. Linthout, K. Tournel, G. Soete, and G. Storme, "Innovations in image-guided radiotherapy," Nat. Rev. Cancer, vol. 7, no. 12, pp. 949–960, Dec. 2007.

[22] H. Shirato, S. Shimizu, K. Kitamura, and R. Onimaru, "Organ motion in image-guided radiotherapy: lessons from real-time tumor-tracking radiotherapy," Int. J. Clin. Oncol., vol. 12, no. 1, pp. 8–16, Feb. 2007.

[23] International Commission on Radiation Units and Measurements, "Prescribing, recording, and reporting photon-beam intensity-modulated radiation therapy-IMRT: ICRU report 83," ICRU, Bethesda, Maryland, USA., Tech. Rep., 2010.

[24] M. Krengli, S. Gaiano, E. Mones, A. Ballarè, D. Beldì, C. Bolchini, and G. Loi, "Reproducibility of patient setup by surface image registration system in conformal radiotherapy of prostate cancer," Radiat. Oncol., vol. 4, p. 9, 2009.

[25] J. C. Stroom, H. C. J. de Boer, H. Huizenga, and A. G. Visser, "Inclusion of geometrical uncertainties in radiotherapy treatment planning by means of coverage probability," Int. J. Radiat. Oncol. Biol. Phys., vol. 43, no. 4, pp. 905–919, Mar. 1999.

[26] J. C. Roeske, J. D. Forman, C. F. Mesina, T. He, C. A. Pelizzari, E. Fontenla, S. Vijayakumar, and G. T. Y. Chen, "Evaluation of changes in the size and location of the prostate, seminal vesicles, bladder, and rectum during a course of external beam radiation therapy," Int. J. Radiat. Oncol. Biol. Phys., vol. 33, no. 5, pp. 1321–1329, Dec. 1995.

[27] G. S. Mageras, G. J. Kutcher, S. A. Leibel, M. J. Zelefsky, E. Melian, R. Mohan, and Z. Fuks, "A method of incorporating organ motion uncertainties into three-dimensional conformal treatment plans," Int. J. Radiat. Oncol. Biol. Phys., vol. 35, no. 2, pp. 333–342, May 1996.

[28] J. M. Crook, Y. Raymond, D. Salhani, H. Yang, and B. Esche, "Prostate motion during standard radiotherapy as assessed by fiducial markers," Radiother. Oncol., vol. 37, no. 1, pp. 35–42, Oct. 1995.

[29] M. van Herk, A. Bruce, A. P. Guus Kroes, T. Shouman, A. Touw, and J. V. Lebesque, "Quantification of organ motion during conformal radiotherapy of the prostate by three dimensional image registration," Int. J. Radiat. Oncol. Biol. Phys., vol. 33, no. 5, pp. 1311–1320, Dec. 1995.

[30] E. Melian, G. S. Mageras, Z. Fuks, S. A. Leibel, A. Niehaus, H. Lorant, M. Zelefsky, B. Baldwin, and G. J. Kutcher, "Variation in prostate position quantitation and implications for three-dimensional conformal treatment planning," Int. J. Radiat. Oncol. Biol. Phys., vol. 38, no. 1, pp. 73–81, Apr. 1997.

[31] S. L. Turner, R. Swindell, N. Bowl, J. Marrs, B. Brookes, G. Read, and R. A. Cowan, "Bladder movement during radiation therapy for bladder cancer: implications for treatment planning," Int. J. Radiat. Oncol. Biol. Phys., vol. 39, no. 2, pp. 355–360, Sep. 1997.

[32] L. P. Muren, R. Smaaland, and O. Dahl, "Organ motion, set-up variation and treatment margins in radical radiotherapy of urinary bladder cancer," Radiother. Oncol., vol. 69, no. 3, pp. 291–304, Dec. 2003.

[33] A. N. Viswanathan, E. D. Yorke, L. B. Marks, P. J. Eifel, and W. U. Shipley, "Radiation dose-volume effects of the urinary bladder," Int. J. Radiat. Oncol. Biol. Phys., vol. 76, no. 3, pp. S116–122, 2010.

[34] T. Rosewall, C. Catton, G. Currie, A. Bayley, P. Chung, J. Wheat, and M. Milosevic, "The relationship between external beam radiotherapy dose and chronic urinary dysfunction â a methodological critique," Radiother. Oncol., vol. 97, no. 1, pp. 40–47, 2010.

[35] M. Thor, L. Bentzen, L. B. Hysing, C. Ekanger, S.-I. Helle, A. Karlsdóttir, and L. P. Muren, "Prediction of rectum and bladder morbidity following radiotherapy of prostate cancer based on motion-inclusive dose distributions," Radiother. Oncol., vol. 107, no. 2, pp. 147–152, May 2013.

[36] R. K. Ten Haken, J. D. Forman, D. K. Heimburger, A. Gerhardsson, D. L. McShan, C. Perez-Tamayo, S. L. Schoeppel, and A. S. Lichter, "Treatment planning issues related to prostate movement in response to differential filling of the rectum and bladder," Int. J. Radiat. Oncol. Biol. Phys., vol. 20, no. 6, pp. 1317–1324, Jun. 1991.

[37] J. M. Balter, H. M. Sandler, K. Lam, R. L. Bree, A. S. Lichter, and R. K. Ten Haken, "Measurement of prostate movement over the course of routine radiotherapy using implanted markers," Int. J. Radiat. Oncol. Biol. Phys., vol. 31, no. 1, pp. 113–118, Jan. 1995.

[38] G. S. Mageras, Z. Fuks, S. A. Leibel, C. C. Ling, M. J. Zelefsky, H. M. Kooy, M. van Herk, and G. J. Kutcher, "Computerized design of target margins for treatment uncertainties in conformal radiotherapy," Int. J. Radiat. Oncol. Biol. Phys., vol. 43, no. 2, pp. 437–445, Jan. 1999.

[39] M. Thor, M. Vaeth, A. Karlsdottir, and L. P. Muren, "Rectum motion and morbidity prediction: Improving correlation between late morbidity and DVH parameters through use of rectum planning organ at risk volumes," Acta Oncol, vol. 49, no. 7, pp. 1061–1068, Oct. 2010.

[40] J. H. Killoran, H. M. Kooy, D. J. Gladstone, F. J. Welte, and C. J. Beard, "A numerical simulation of organ motion and daily setup uncertainties: Implications for radiation therapy," Int. J. Radiat. Oncol. Biol. Phys., vol. 37, no. 1, pp. 213–221, Jan. 1997.

[41] T. Craig, J. Battista, V. Moiseenko, and J. Van Dyk, "Considerations for the implementation of target volume protocols in radiation therapy," Int. J. Radiat. Oncol. Biol. Phys., vol. 49, no. 1, pp. 241–250, Jan. 2001.

[42] T. F. Mutanga, H. C. J. de Boer, G. J. van der Wielen, M. S. Hoogeman, L. Incrocci, and B. J. M. Heijmen, "Margin evaluation in the presence of deformation, rotation, and translation in prostate and entire seminal vesicle irradiation with

daily marker-based setup corrections," Int. J. Radiat. Oncol. Biol. Phys., vol. 81, no. 4, pp. 1160–1167, Nov. 2011.

[43] M. Thor, A. Apte, J. O. Deasy, and L. P. Muren, "Statistical simulations to estimate motion-inclusive dose-volume histograms for prediction of rectal morbidity following radiotherapy," Acta Oncol., vol. 52, no. 3, pp. 666–675, Apr. 2013.

[44] M. S. Hoogeman, M. van Herk, D. Yan, L. J. Boersma, P. C. M. Koper, and J. V. Lebesque, "A model to simulate day-to-day variations in rectum shape," Int. J. Radiat. Oncol. Biol. Phys., vol. 54, no. 2, pp. 615–625, Oct. 2002.

[45] L. M. Pavel-Mititean, C. G. Rowbottom, C. L. Hector, M. Partridge, T. Bortfeld, and W. Schlegel, "A geometric model for evaluating the effects of inter-fraction rectal motion during prostate radiotherapy," Phys. Med. Biol., vol. 49, no. 12, p. 2613, Jun. 2004.

[46] D. Yan, D. Jaffray, and J. Wong, "A model to accumulate fractionated dose in a deforming organ," Int J Radiat Oncol Biol Phys, vol. 44, no. 3, pp. 665–675, Jun. 1999.

[47] M. B. Boubaker, M. Haboussi, J.-F. Ganghoffer, and P. Aletti, "Finite element simulation of interactions between pelvic organs: Predictive model of the prostate motion in the context of radiotherapy," J. Biomech., vol. 42, no. 12, pp. 1862–1868, Aug. 2009.

[48] E. Fontenla, C. A. Pelizzari, J. C. Roeske, and G. T. Y. Chen, "Numerical analysis of a model of organ motion using serial imaging measurements from prostate radiotherapy," Phys. Med. Biol., vol. 46, no. 9, p. 2337, Sep. 2001.

[49] ——, "Using serial imaging data to model variabilities in organ position and shape during radiotherapy," Phys. Med. Biol., vol. 46, no. 9, p. 2317, Sep. 2001.

[50] M. Söhn, B. Sobotta, and M. Alber, "Dosimetric treatment course simulation based on a statistical model of deformable organ motion," Phys. Med. Biol., vol. 57, no. 12, pp. 3693–3709, Jun. 2012.

[51] S. Thörnqvist, L. B. Hysing, A. G. Zolnay, M. Söhn, M. S. Hoogeman, L. P. Muren, L. Bentzen, and B. J. M. Heijmen, "Treatment simulations with a statistical deformable motion model to evaluate margins for multiple targets in radiotherapy for high-risk prostate cancer," Radiother. Oncol., vol. 109, no. 3, pp. 344–349, Dec. 2013.

[52] Q. Zhang, A. Pevsner, A. Hertanto, Y.-C. Hu, K. E. Rosenzweig, C. C. Ling, and G. S. Mageras, "A patient-specific respiratory model of anatomical motion for radiation treatment planning," Med Phys, vol. 34, no. 12, pp. 4772–4781, Dec. 2007.

[53] A. M. Badawi, E. Weiss, W. C. Sleeman, C. Yan, and G. D. Hugo, "Optimizing principal component models for representing interfraction variation in lung cancer radiotherapy," Med. Phys., vol. 37, no. 9, pp. 5080–5091, Sep. 2010.

[54] E. Budiarto, M. Keijzer, P. R. Storchi, M. S. Hoogeman, L. Bondar, T. F. Mutanga, H. C. J. de Boer, and A. W. Heemink, "A population-based model to describe geometrical uncertainties in radiotherapy: applied to prostate cases," Phys. Med. Biol., vol. 56, no. 4, pp. 1045–1061, Feb. 2011.

[55] L. Bondar, M. Intven, J. P. M. Burbach, E. Budiarto, J. P. Kleijnen, M. Philippens, B. van Asselen, E. Seravalli, O. Reerink, and B. Raaymakers, "Statistical modeling of ctv motion and deformation for imrt of early-stage rectalÂ cancer," Int. J. Radiat. Oncol. Biol. Phys., vol. 90, no. 3, pp. 664–672, November 2014.

[56] R. Rios, J. D. Ospina, C. Lafond, O. Acosta, J. Espinosa, and R. de Crevoisier, "Characterization of Bladder Motion and Deformation in Prostate Cancer Radiotherapy," IRBM, vol. 37, no. 5–6, pp. 276–283, Nov. 2016.

[57] M. Söhn, M. Birkner, D. Yan, and M. Alber, "Modelling individual geometric variation based on dominant eigenmodes of organ deformation: implementation and evaluation," Phys. Med. Biol., vol. 50, no. 24, pp. 5893–5908, Dec. 2005.

[58] T. F. Cootes, C. J. Taylor, D. H. Cooper, and J. Graham, "Active Shape Models-Their Training and Application," Computer Vision and Image Understanding, vol. 61, no. 1, pp. 38–59, Jan. 1995.

[59] Y. Jeong, R. J. Radke, and D. M. Lovelock, "Bilinear models for inter- and intra-patient variation of the prostate," Phys. Med. Biol., vol. 55, no. 13, pp. 3725–3739, Jul. 2010.

[60] A. H. Foruzan, Y.-W. Chen, M. Hori, Y. Sato, and N. Tomiyama, "Capturing large shape variations of liver using population-based statistical shape models," Int J Comput Assist Radiol Surg, Apr. 2014.

[61] R. Rios, J. D. Ospina, F. Commandeur, C. Lafond, O. Acosta, J. Espinosa, and R. de Crovoiser, "Prediction of geometrical variations of the bladder in image guided radiotherapy for prostate cancer." in ICART Workshoop MICCAI 9th Octuber, Munich, Germany, 2015.

[62] R. Rios, R. De Crevoisier, J. D. Ospina, F. Commandeur, C. Lafond, A. Simon, P. Haigron, J. Espinosa, and O. Acosta, "Population model of bladder motion and deformation based on dominant eigenmodes and mixed-effects models in prostate cancer radiotherapy," Med. Image Anal., vol. 38, pp. 133–149, May 2017.

[63] J. R. McClelland, D. J. Hawkes, T. Schaeffter, and A. P. King, "Respiratory motion models: A review," Med. Image Anal., vol. 17, no. 1, pp. 19–42, Jan. 2013.

[64] S. Durrleman, X. Pennec, A. Trouvé, J. Braga, G. Gerig, and N. Ayache, "Toward a comprehensive framework for the spatiotemporal statistical analysis of longitudinal shape data," Int J Comput Vis, vol. 103, no. 1, pp. 22–59, May 2013.

[65] J. Pinheiro and D. Bates, Mixed-Effects Models in S and S-PLUS, 1st ed. Springer.

[66] Y. Hu, E. Gibson, H. U. Ahmed, C. M. Moore, M. Emberton, and D. C. Barratt, "Population-based prediction of subject-specific prostate deformation for MR-to-ultrasound image registration," Med. Image Anal., vol. 26, no. 1, pp. 332–344, Dec. 2015.

[67] T. He, Z. Xue, W. Xie, and S. T. C. Wong, "Online 4-D CT Estimation for Patient-Specific Respiratory Motion Based on Real-Time Breathing Signals," in Medical Image Computing and Computer-Assisted Intervention â MICCAI 2010. Springer, Berlin, Heidelberg, Sep. 2010, pp. 392–399.

[68] F. Preiswerk, V. De Luca, P. Arnold, Z. Celicanin, L. Petrusca, C. Tanner, O. Bieri, R. Salomir, and P. C. Cattin, "Model-guided respiratory organ motion prediction of the liver from 2d ultrasound," Med. Image Anal., vol. 18, no. 5, pp. 740–751, Jul. 2014.

[69] C. Fiorino, R. Valdagni, T. Rancati, and G. Sanguineti, "Dose volume effects for normal tissues in external radiotherapy: Pelvis," Radiother. Oncol., vol. 93, no. 2, pp. 153–167, Nov. 2009.

[70] V. Beckendorf, S. Guérif, E. L. Prisé, J. M. Cosset, O. Lefloch, B. Chauvet, N. Salem, O. Chapet, S. Bourdin, J. M. Bachaud, P. Maingon, J.-L. Lagrange, L. Malissard, J.-M. Simon, P. Pommier, M. H. Hay, B. Dubray, E. Luporsi, and P. Bey, "The GETUG 70 Gy vs. 80 Gy randomized trial for localized prostate cancer: Feasibility and acute toxicity," Int. J. Radiat. Oncol. Biol. Phys., vol. 60, no. 4, pp. 1056–1065, Nov. 2004.

[71] C. Lorenz and N. Krahnstöver, "Generation of point-based 3d statistical shape models for anatomical objects," Computer Vision and Image Understanding, vol. 77, no. 2, pp. 175–191, 2000.

[72] D. H. Ballard and C. M. Brown, Computer Vision, first edition ed. Englewood Cliffs, N.J: Prentice Hall, May 1982.

[73] C. Brechbühler, G. Gerig, and O. Kübler, "Parametrization of Closed Surfaces for 3-D Shape Description," Computer Vision and Image Understanding, vol. 61, no. 2, pp. 154–170, Mar. 1995.

[74] G. Székely, A. Kelemen, C. Brechbühler, and G. Gerig, "Segmentation of 2-D and 3-D objects from MRI volume data using constrained elastic deformations of flexible Fourier contour and surface models," Med. Image Anal., vol. 1, no. 1, pp. 19–34, Mar. 1996.

[75] A. Kelemen, G. Szekely, and G. Gerig, "Elastic model-based segmentation of 3-D neuroradiological data sets," IEEE Transactions on Medical Imaging, vol. 18, no. 10, pp. 828–839, Oct. 1999.

[76] L. Shen, J. Ford, F. Makedon, and A. Saykin, "A surface-based approach for classification of 3d neuroanatomical structures," Intelligent Data Analysis, vol. 8, no. 6, pp. pp.519–542, 2004.

[77] M. Styner, J. A. Lieberman, D. Pantazis, and G. Gerig, "Boundary and medial shape analysis of the hippocampus in schizophrenia," Med. Image Anal., vol. 8, no. 3, pp. 197–203, Sep. 2004.

[78] M. Styner, I. Oguz, S. Xu, C. Brechbühler, D. Pantazis, J. J. Levitt, M. E. Shenton, and G. Gerig, "Framework for the Statistical Shape Analysis of Brain Structures using SPHARM-PDM," Insight J, no. 1071, pp. 242–250, 2006.

[79] L. Shen, S. Kim, and A. J. Saykin, "Fourier method for large scale surface modeling and registration," Comput. Graph., vol. 33, no. 3, pp. 299–311, Jun. 2009.

[80] L. Shen, H. Farid, and M. A. McPeek, "Modeling three-dimensional morphological structures using spherical harmonics," Evolution, vol. 63, no. 4, pp. 1003–1016, Apr. 2009.

[81] J.-L. Dillenseger, H. Guillaume, and J.-J. Patard, "Spherical harmonics based intrasubject 3-D kidney modeling/registration technique applied on partial information," IEEE Trans Biomed Eng, vol. 53, no. 11, pp. 2185–2193, Nov. 2006.

[82] G. Gerig, M. Styner, D. Jones, D. Weinberger, and J. Lieberman, "Shape analysis of brain ventricles using SPHARM," in IEEE Workshop on Mathematical Methods in Biomedical Image Analysis, 2001. MMBIA 2001, 2001, pp. 171–178.

[83] T. Tateyama, M. Okegawa, M. Uetani, H. Tanaka, S. Kohara, X. Han, S. Kanasaki, S. Sato, M. Wakamiya, A. Furukawa, H. Jiang, and Y. W. Chen, "Efficient shape representation and statistical shape modeling of the liver using spherical harmonic functions (SPHARM)," in 2012 Joint 6th International Conference on Soft Computing and Intelligent Systems (SCIS) and 13th International Symposium on Advanced Intelligent Systems (ISIS), Nov. 2012, pp. 428–431.

[84] Y. Zhang, Y. Bazilevs, S. Goswami, C. L. Bajaj, and T. J. R. Hughes, "Patient-specific vascular NURBS modeling for isogeometric analysis of blood flow," Computer Methods in Applied Mechanics and Engineering, vol. 196, no. 29, pp. 2943–2959, May 2007.

[85] V. P. Nguyen, C. Anitescu, S. P. A. Bordas, and T. Rabczuk, "Isogeometric analysis: An overview and computer implementation aspects," Mathematics and Computers in Simulation, vol. 117, pp. 89–116, November 2015.

[86] N. M. Laird and J. H. Ware, "Random-effects models for longitudinal data," Biometrics, vol. 38, no. 4, pp. 963–974, Dec. 1982.

[87] R. D. G. Donald Hedeker, Longitudinal Data Analysis. John Wiley & Sons, Inc., Hoboken, New Jersey, USA, 2006.

[88] G. Fitzmaurice, N. Laird, and J. Ware, Applied Longitudinal Analysis, ser. Wiley Series in Probability and Statistics. John Wiley & Sons, Inc., Hoboken, New Jersey, USA, 2011.

[89] E. W. Frees, Longitudinal and Panel Data: Analysis and Applications in the Social Sciences, 1st ed. New York: Cambridge University Press, 2004.

[90] R. S. Prabhu, M. Won, E. G. Shaw, C. Hu, D. G. Brachman, J. C. Buckner, K. J. Stelzer, G. R. Barger, P. D. Brown, M. R. Gilbert, and M. P. Mehta, "Effect of the addition of chemotherapy to radiotherapy on cognitive function in patients with low-grade glioma: Secondary analysis of RTOG 98-02," J. Clin. Oncol., vol. 32, no. 6, pp. 535–541, 2014.

[91] A. L. Hanlon, D. F. Moore, and G. E. Hanks, "Modeling postradiation prostate specific antigen level kinetics," Cancer, vol. 83, no. 1, pp. 130–134, Jul. 1998.

[92] T. Bastogne, A. Samson, P. Vallois, S. Wantz-Mézières, S. Pinel, D. Bechet, and M. Barberi-Heyob, "Phenomenological modeling of tumor diameter growth based on a mixed effects model," J. Theor. Biol., vol. 262, no. 3, pp. 544–552, 2010.

[93] J. L. Bernal-Rusiel, M. Reuter, D. N. Greve, B. Fischl, and M. R. Sabuncu, "Spatiotemporal linear mixed effects modeling for the mass-univariate analysis of longitudinal neuroimage data," Neuroimage, vol. 81, pp. 358–370, November 2013.

[94] G. Ziegler, W. D. Penny, G. R. Ridgway, S. Ourselin, and K. J. Friston, "Estimating anatomical trajectories with Bayesian mixed-effects modeling," Neuroimage, vol. 121, pp. 51–68, Nov. 2015.

[95] X. Liu, "Chapter 3 - linear mixed-effects models," in Methods and Applications of Longitudinal Data Analysis, X. Liu, Ed. Oxford: Academic Press, 2016, pp. 61 – 94.

[96] K.-Y. Liang and S. L. Zeger, "Longitudinal data analysis using generalized linear models," Biometrika, vol. 73, no. 1, pp. 13–22, Apr. 1986.

[97] W. Guo, "Functional Mixed Effects Models," Biometrics, vol. 58, no. 1, pp. 121–128, 2002.

[98] J. S. Morris and R. J. Carroll, "Wavelet-based functional mixed models," J R Stat Soc Series B Stat Methodol, vol. 68, no. 2, pp. 179–199, Apr. 2006.

[99] H. Wu and J.-T. Zhang, "Local Polynomial Mixed-Effects Models for Longitudinal Data," J. Am. Stat. Assoc., vol. 97, no. 459, pp. 883–897, 2002.

[100] J. A. D. Aston, J.-M. Chiou, and J. P. Evans, "Linguistic pitch analysis using functional principal component mixed effect models," Journal of the Royal Statistical Society: Series C (Applied Statistics), vol. 59, no. 2, pp. 297–317, Mar. 2010.

[101] A. Kraskov and P. Grassberger, "MIC: Mutual information based hierarchical clustering," in Information Theory and Statistical Learning, F. Emmert-Streib and M. Dehmer, Eds. Springer US, 2009, pp. 101–123.

[102] D. B. Russakoff, C. Tomasi, T. Rohlfing, and C. R. M. Jr, "Image similarity using mutual information of regions," in Computer Vision - ECCV 2004, ser. Lecture Notes in Computer Science. Springer Berlin Heidelberg, 2004, vol. 3023, pp. 596–607.

[103] F. Maes, A. Collignon, D. Vandermeulen, G. Marchal, and P. Suetens, "Multimodality image registration by maximization of mutual information," IEEE Trans Med Imaging, vol. 16, no. 2, pp. 187–198, 1997.

[104] J. C. Pinheiro and D. M. Bates, "Unconstrained parametrizations for variance-covariance matrices," Statistics and Computing, vol. 6, no. 3, pp. 289–296, 1996.

[105] S. Gill, K. Dang, C. Fox, M. Bressel, T. Kron, N. Bergen, N. Ferris, R. Owen, S. Chander, K. H. Tai, and F. Foroudi, "Seminal vesicle intrafraction motion analysed with cinematic magnetic resonance imaging," Radiat. Oncol., vol. 9, Aug. 2014.

[106] C. Bishop and M. Tipping, "A hierarchical latent variable model for data visualization," IEEE Trans. Pattern Anal. Mach. Intell., vol. 20, no. 3, pp. 281–293, Mar. 1998.

[107] G. J. Price and C. J. Moore, "A method to calculate coverage probability from uncertainties in radiotherapy via a statistical shape model," Phys. Med. Biol., vol. 52, no. 7, pp. 1947–1965, Apr. 2007.

[108] T. Heimann and H.-P. Meinzer, "Statistical shape models for 3d medical image segmentation: A review," Med. Image Anal., vol. 13, no. 4, pp. 543–563, Aug. 2009.

[109] H. Hotelling, "Analysis of a complex of statistical variables into principal components." J. Educ. Psychol., vol. 24, no. 6, pp. 417–441, 1933.

[110] I. T. Jolliffe, Principal Component Analysis. Springer, Oct. 2002.

[111] F. Palorini, A. Botti, V. Carillo, S. Gianolini, I. Improta, C. Iotti, T. Rancati, C. Cozzarini, and C. Fiorino, "Bladder dose–surface maps and urinary toxicity: Robustness with respect to motion in assessing local dose effects," Physica Medica, vol. 32, no. 3, pp. 506–511, Mar. 2016.

[112] C.-Z. Di, C. M. Crainiceanu, B. S. Caffo, and N. M. Punjabi, "Multilevel functional principal component analysis," The Annals of Applied Statistics, vol. 3, no. 1, pp. 458–488, 2009.

[113] S. Greven, C. Crainiceanu, B. Caffo, and D. Reich, "Longitudinal functional principal component analysis," Electron J Stat, vol. 4, pp. 1022–1054, 2010.

[114] C. M. Bishop, Pattern Recognition and Machine Learning. 1st edition, Springer, Cambridge, U.K, 2006.

[115] R. Rios, F. Commandeur, O. Acosta, C. Lafond, J. Espinosa, and R. De Crevoisier, "Hierarchical eigenmodes to characterize bladder motion and deformation in prostate cancer radiotherapy," in Proc. SPIE 10160, 12th International Symposium on Medical Information Processing and Analysis, vol. 10160, 2017, pp. 101 601E–101 601E–13. http://dx.doi.org/10.1117/12.2 256 916.

[116] E. Budiarto, M. Keijzer, P. R. M. Storchi, A. W. Heemink, S. Breedveld, and B. J. M. Heijmen, "Computation of mean and variance of the radiotherapy dose for PCA-modeled random shape and position variations of the target," Phys. Med. Biol., vol. 59, no. 2, pp. 289–310, Jan. 2014.

[117] G. Cazoulat, A. Simon, A. Dumenil, K. Gnep, R. de Crevoisier, O. Acosta, and P. Haigron, "Surface-constrained nonrigid registration for dose monitoring in prostate cancer radiotherapy," IEEE Trans Med Imaging, vol. 33, no. 7, pp. 1464–1474, Jul. 2014.

[118] M. Nassef, A. Simon, G. Cazoulat, A. Duménil, C. Blay, C. Lafond, O. Acosta, J. Balosso, P. Haigron, and R. de Crevoisier, "Quantification of dose uncertainties in cumulated dose estimation compared to planned dose in prostate IMRT," Radiother. Oncol., vol. 119, no. 1, pp. 129–136, Apr. 2016.

[119] R. A. Johnson and D. W. Wicherm, Applied Multivariate Statistical Analysis, 6th ed. Pearson, USA, 2008.

[120] G. J. Kutcher, C. Burman, L. Brewster, M. Goitein, and R. Mohan, "Histogram reduction method for calculating complication probabilities for three-dimensional treatment planning evaluations," Int. J. Radiat. Oncol. Biol. Phys., vol. 21, no. 1, pp. 137–146, May 1991.

[121] T. E. Schultheiss, C. G. Orton, and R. A. Peck, "Models in radiotherapy: volume effects," Med. Phys., vol. 10, no. 4, pp. 410–415, Aug. 1983.

[122] P. Källman, A. Agren, and A. Brahme, "Tumour and normal tissue responses to fractionated non-uniform dose delivery," Int. J. Radiat. Biol., vol. 62, no. 2, pp. 249–262, Aug. 1992.

[123] L. A. Dawson, M. Biersack, G. Lockwood, A. Eisbruch, T. S. Lawrence, and R. K. Ten Haken, "Use of principal component analysis to evaluate the partial

organ tolerance of normal tissues to radiation," Int. J. Radiat. Oncol. Biol. Phys., vol. 62, no. 3, pp. 829–837, Jul. 2005.

[124] F. Buettner, S. L. Gulliford, S. Webb, M. R. Sydes, D. P. Dearnaley, and M. Partridge, "Assessing correlations between the spatial distribution of the dose to the rectal wall and late rectal toxicity after prostate radiotherapy: an analysis of data from the MRC RT01 trial (ISRCTN 47772397)," Phys. Med. Biol., vol. 54, no. 21, pp. 6535–6548, Nov. 2009.

[125] O. Acosta, G. Drean, J. D. Ospina, A. Simon, P. Haigron, C. Lafond, and R. d. Crevoisier, "Voxel-based population analysis for correlating local dose and rectal toxicity in prostate cancer radiotherapy," Phys Med Biol, vol. 58, no. 8, p. 2581, Apr. 2013.

[126] J. D. Ospina, J. Zhu, C. Chira, A. Bossi, J. B. Delobel, V. Beckendorf, B. Dubray, J.-L. Lagrange, J. C. Correa, A. Simon, O. Acosta, and R. de Crevoisier, "Random forests to predict rectal toxicity following prostate cancer radiation therapy," Int. J. Radiat. Oncol. Biol. Phys., vol. 89, no. 5, pp. 1024–1031, Aug. 2014.

[127] R. L. Burden and J. D. Faires, Numerical Analysis, 9th ed. CENGAGE Learning, Boston, USA, 2010.